Max Planck Institut für Kolloid und Grenzflächenforschung

# Sustainable biomass-derived hydrothermal carbons for energy applications

**Dissertation**

zur Erlangung des akademischen Grades

"doctor rerum naturalium"

(Dr. rer. nat.)

in der Wissenschaftsdisziplin "Kolloidchemie"

eingereicht an der

Mathematisch-Naturwissenschaftlichen Fakultät

der Universität Potsdam

von

**Camillo Falco**

**Potsdam, im Januar 2012**

Published online at the
Institutional Repository of the University of Potsdam:
URL http://opus.kobv.de/ubp/volltexte/2012/5978/
URN urn:nbn:de:kobv:517-opus-59785
http://nbn-resolving.de/urn:nbn:de:kobv:517-opus-59785

## EIDESSTATTLICHE ERKLÄRUNG /STATUTORY DECLARATION

“Hiermit erkläre ich an Eides statt, dass ich die vorliegende Dissertation selbständig und ohne Hilfe verfasst, keine anderen als die angegebenen Quellen und Hilfsmittel benutzt und wörtlich oder inhaltlich entnommene Stellen als solche kenntlich gemacht habe.”
Potsdam, im Januar 2012

“I herewith formally declare that I myself have written the submitted dissertation independently. I did not use any outside support except for the quoted literature and all the other sources which I employed producing this academic work, either literally or in content.”
Potsdam, January 2012

Camillo Falco

***Ricett' o pappic' vicin' à noce....Ramm' o tiemp ca te sportos'!***

Ancient proverb from Neapolitan popular wisdom

*A tutti coloro che vorrei rendere felici*

## Acknowledgments

I would like first of all to thank all the people that have contributed either with professional help or with moral support to the realisation of this thesis.

I would like to start by thanking my official supervisor Prof. Markus Antonietti for allowing me to conduct my doctoral studies at the Max Planck Institute of Colloids and Interfaces, for granting me the necessary freedom to develop my own research ideas and for the suggestions provided throughout the development of this work.

Dr. Maria-Magdalena Titirici is greatly thanked for the supervision, professional help and advices provided during these two years, but also for the organisation of several extra-work activities, which have filled my permanence here at the MPI of wonderful memories.

I am very grateful also to Dr. Niki Baccile, for his precious help and supervision on Solid State NMR studies and for introducing me to the concept of art in science.

I would like to express my sincere gratitude to Dr. Robin White for being always present, whenever I have been in need of professional or moral support.

I would also like to thank Prof. Dolores Lozano-Castelló and David Salinas Torres for fruitful collaboration and for providing irreplaceable measurements and technical expertise.

Dr. Marta Sevilla is also thanked for all her patience despite my numerous questions and for the collaboration developed on the microalgae project.

Carmen Serra (Uni Vigo), Dr. Jane Howe (Oak Ridge National Laboratory), Dr. Vitaly Budarin (University of York), Regina Rothe and Sylvia Pirok are thanked for performing measurements necessary to the realisation of this work.

I would also like to thank the numerous office mates that I have had the pleasure to share the "Big Office" with during these two years, Clara, Jerome, Johannes, Steffy, Tim, Li, Sujeong, Linghui, Bettina, Antje, Debora, Marek, Yussuf, Fang Zheng, Sebastian, Kang-Go and Giani. I can certainly say that meeting all of you has contributed to make each day here in Golm special in its own way, and not a boring routine.

Great thanks are also for all the colleagues that I have met here at the MPI during these two years: Shiori, Fernando, Li, Zoe, Irene, Jelena, George, Marina, Alfonso, Ruben, Stefan, Nina, Daniel, Alex, David, Hiro, Filipe, Nico, Katja, Pablo, Miriam, John, Dimitri, Davide, Admir, Luca, Lorenzo (If someone has been left out, I

apologise). You have been a great source of surprises and constant amusement and have certainly taught me lots of lessons going beyond science.

Special thanks go to my “acquired” family here in Berlin: Chris, Ferdi, Mike, Cordi, Robin, Nora, Malte, Aida, Manu. You have always managed to make “home” a welcoming place where to go back.

I also would like to thank my family for their understanding and constant support. *Grazie di cuore per aver fatto si che la distanza tra noi sia sempre e solo stata fisica durante tutti questi anni.*

My last but greatest “thank you” goes to Lena Witte for all her support during these two years and for constantly reminding me *la legerezza del vivere.*

# Table of contents

# CHAPTER 1 – Introduction

## 1.1 From fossil fuels to the "Biorefinery Concept" and Green Chemistry

The dependence of humankind on fossil fuels is one of the major concerns of modern society. For centuries these commodities have provided the energy and the raw materials necessary to improve people's living standards and to produce needed goods in daily life (e.g. pharmaceuticals, plastics, paints, inks). The world hunger for these resources has steadily increased in time due to a continuous population growth and to a progressively more energy intensive lifestyle (e.g. constant use of electrically powered appliances, frequent long distance travelling), leading to their depletion and future consequential scarcity. According to recent estimates, the world oil demand will increase from the actual value of 84 millions barrels a day to 116 millions a day in 2030.[1] On the other hand, oil production will most likely achieve its maximum output peak within the next 15 years and subsequently start gradually decline.[2, 3] The development of novel oil extraction processes and the consequential unlocking of more remote reserves will probably delay the depletion of these resources. However the distance between demand and supply of this commodity will unavoidably increase, leading to rocketing prices. Furthermore the oligopolistic nature of the fossil fuels market will further contribute to increase the price volatility of this commodity, rendering its overall supply more unstable and unreliable. For these reasons, the need to move away from a fossil fuel based economy and to find an alternative and secure energy supply has lately become one of the main points on the governmental agenda of several countries.

A second, but equally strong driving force towards the reduction of fossil fuels consumption is represented by the increasing social awareness concerned with environmental protection. Several evidences have shown that the wild and unregulated exploitation of fossil fuels is having severe and negative effects on the planet's "health" (e.g. acid rain, smog in highly industrialised areas, ground-water pollution, alteration of the Carbon and Nitrogen cycles leading to global warming).[4] As a consequence, the desire of conducting a sustainable life-style, causing no harm to the planet, is spreading more and more among people, in particular in the so-called "developed Western countries".

The combination of these economical, political and environmental motivations is nowadays behind the enormous research activities encompassing numerous scientific fields and focusing mainly on the development of novel technologies, able to exploit the planet renewable energy resources (e.g. sun, tides, wind, biomass). However, although energy is the key topic of this new research wave, part of the research effort is also focused on finding alternatives to fossil fuels derived products/materials. In this regard, for the short term the most promising substitute is undoubtedly biomass, since it is the only renewable and sustainable alternative to fossil fuels as a source of carbon. In particular lignocellulosic and waste biomass has attracted several attentions in the recent past, since they do not compete with the food chain or, in most cases, for lands aimed at food production. Therefore, starting from biomass as a feedstock, the "Biorefinery concept" has been created and largely developed in the last years (Fig. 1.1). The International Energy Agency (IEA) has recently defined Biorefinering as *"the sustainable processing of biomass into a spectrum of marketable products and energy"*.[5] A Biorefinery thus implies integrated systems using all the available resources in an effective and efficient manner. The used technology may involve a mix of physical, thermal, chemical or biological processes, aimed at converting the biomass feedstock in carbon neutral/negative biofuels, energy or materials.

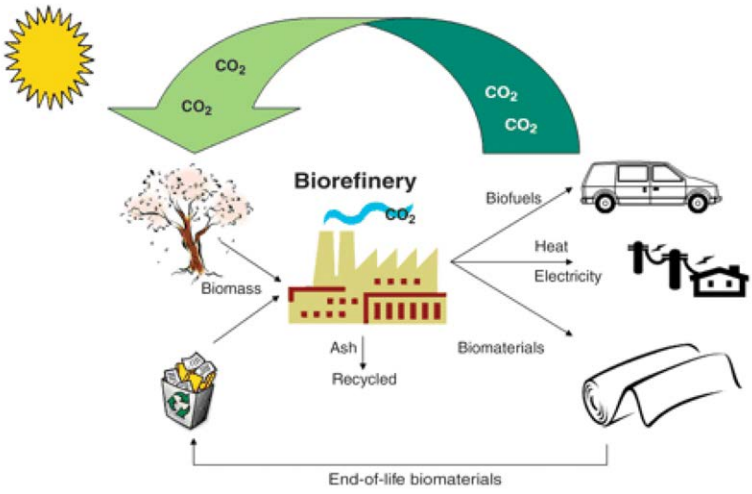


**Figure 1.1:** The "Biorefinery Concept". Reproduced from [6]

In order to enhance the sustainability of biorefineries, their development should be shaped according to the principles of *Green Chemistry,* which provide a tool kit for the design of "environmentally friendly" chemical processes. Crucial parameters to consider are atom and energy efficiency, catalysis, safety, real-time analysis and preventive design in order to avoid production of waste, hazardous chemicals or

unrecyclable products.[7, 8] Integrating the principles of *Green Chemistry* to the "Biorefinery concept" is thus considered to be the key to unlock biomass as a feedstock for the chemical industry in a fully sustainable manner.[9]

## 1.2 Sustainable carbon materials

Carbon materials are ubiquitous in mankind daily life. They are employed in numerous applications, such as catalysis, chromatography, gas storage, water remediation, soil amendment, energy production and storage.[10-13] Their successfulness in fulfilling such a great variety of tasks arises from their enormous versatility. According to the carbon source and processing conditions, these materials can be designed and synthesised in order to show several beneficial properties (e.g. high electrical conductivity and thermal stability, chemical inertness, high surface area and pore volume, high mechanical strength).

A second factor, largely contributing to their widespread use, is the high abundance and relatively cheapness of carbon material precursors leading to reduced costs of production. However the major fraction of such precursors is still based on fossil fuel resources (e.g. hydrocarbons, petroleum pitch, coal, tars) posing several doubts on the sustainability of carbon materials.[14] Furthermore, the most common synthetic pathways for the production of carbon materials involve pyrolysis (or carbonisation) or more energy intensive methods such as laser ablation, electro-arc discharge or chemical vapour deposition, which are all processes far away from the principles of *Green Chemistry*.[15, 16]

A more sustainable approach towards the synthesis of carbon materials would be the direct use of biomass as organic precursors. The large-scale production of long-lasting carbon materials from such renewable resources could be an effective carbon sink. In the long-run this solution would contribute to re-establish an equilibrium scenario in the planet carbon cycle. However the successful exploitation of biomass as carbon precursor poses some major challenges, mostly arising from its heterogeneous composition and complex structure requiring either pre-treatment, to separate it in its single component, or novel synthetic processes, able to cope with such features. Additionally these processes should also be designed in respect of the *Green Chemistry* sustainability requirements, adding a further challenge to the pathway towards the successful exploitation of biomass as carbon precursor.

Research efforts in this direction have considerably multiplied in the last years. Numerous examples of carbon materials derived from *"green"* processing of biomass or of its components (e.g. seaweed, tannins, lignocellulosic biomass derived monomers) can be found in the literature.[17-20] One of the most prominent examples are Starbons©. Clark *et al.* have managed to synthesise highly mesoporous carbon aerogels from several polysaccharide precursors (e.g. pectin, alginic acid and high-amylose corn starch) via the initial gelation of the parent biopolymers and subsequent retrogradation upon cooling. A heat treatment step was then adopted to yield the final carbonaceous product.[21, 22] These examples provide the evidences that substituting fossil fuels based precursors with biomass for the synthesis of carbon materials is indeed possible. As a consequence novel developments of this research field will most likely shape the future of carbon materials.

## 1.3 Hydrothermal Carbonisation: The "Chimie Douce" of carbon materials

In the context of the "biorefinery concept" and sustainable carbon materials, hydrothermal carbonisation (HTC) has received great attention from both the academic and industrial worlds in the last years. This thermochemical processing technique is an effective means of biomass conversion, especially carbohydrate rich biomass, in carbonaceous "coal-like" products mimicking the natural coalification process.[23] HTC is considered particularly advantageous, because it exploits mild processing conditions (160 – 260 $^{o}$C and self-generated pressure, 10 – 30 bar) and an environmentally benign solvent (i.e. water) as reaction medium.[24] As consequence it shows great potential to satisfy the *Green Chemistry* requirements.

Hydrothermal treatment of biomass has been an intensively investigated research topic since the beginning of the 20$^{th}$ century. One of the first studies dates back to 1913, when the chemist and Nobel laureate Friederich Bergius reported on the transformation of cellulose into coal-like material under hydrothermal conditions.[25] Several other studies followed, however mostly focused on the separation of lignocellulosic biomass into its components and the subsequent hydrolysis of the carbohydrate fraction into its building blocks (i.e. monosaccharides).[26, 27] However they never generated appreciable interests in industrial partners due to the uncompetitive process economics compared to fossil fuels derived products. As previously explained, in the last decades the urgent need to move away from a fossil fuel based economy has shifted the market spotlight towards the use of biomass. As a

consequence, biomass derived HTC products have become increasingly more interesting for a variety of applications. Electricity producer companies (e.g. Vattenfall) are currently testing lignocellulosic biomass derived HTC products as a fuel substituent for the numerous coal fired plants present in Germany.[28] HTC carbonaceous products are also being tested for soil amendment purposes, since their relatively more hydrophilic nature compared to biochars obtained from pyrolysis, makes them more suitable for soil nutrients retention.[13, 29, 30]

The HTC concept has recently also been extended to the synthesis of carbon materials.[31] In particular Antonietti and his coworkers have rediscovered this facile synthesis route to generate highly functional materials from biomass derivatives.[32, 33] Their research efforts have mostly focused on the use of monosaccharides as carbon precursors, whilst the utilisation of crude biomass has been rarer.[34] Glucose, in particular, has been largely employed, since it is the most-abundant biomass derived sugar. The developed HTC method exploits the dehydration of glucose to 5-hydroxymethylfurfural (5-HMF) via isomerisation to fructose under hydrothermal conditions. The furan based intermediate undergoes then a manifold of reactions (e.g. aldol or self-condensation, substitution), involving also other glucose degradation products (e.g. levulinic acid), leading to the formation of the carbonaceous product or HTC carbon (For a more detailed description of the glucose derived HTC carbon structure and the possible reactions leading to its formation, see Chapter 2).[35] The morphology of HTC carbon, derived from pure glucose, is characterised by micron-sized spherical particles, showing no appreciable porosity and therefore limiting its range of possible applications.[34] However using either soft or hard templating strategies or growth directing agents (e.g. ovalbumin) allows the synthesis of HTC carbons with more interesting morphologies (e.g. mesoporous aerogels, hollow spheres, nanowires) having several foreseeable applications (chromatography, catalyst support, energy storage and production).[36, 37] The ability of HTC to generate such a variety of morphologies from biomass derived precursors, highlights its high effectiveness as sustainable and "green" method for the synthesis of functional carbon materials. For this reason, HTC has been recently defined as the leading pathway towards the "*Chimie Douce"* (conceptual translation: *mild chemistry*) of carbon materials.[38]

The attempts to synthesise functional HTC carbon materials directly from crude biomass, in particular lignocellulosic biomass, have shown to be more challenging.

As previously explained, the main obstacle towards the successful exploitation of such raw materials is represented by their heterogeneous composition and complex structure. However, unlocking the direct use of such resources as carbon precursors would certainly be beneficial in terms of HTC sustainability enhancement. The combination of these challenges and motivations sets the frame for the work herein presented. In this study the direct use of carbohydrate-rich (i.e. lignocellulosic biomass) and protein-rich (i.e. algae) biomass for the synthesis of carbon materials is investigated.

In the first part of this thesis (Chapters 3 and 4) a comparison between the HTC of simple monosaccharides (i.e. glucose) and lignocellulosic biomass is developed based on a systematic study of the HTC process. Furthermore the pyrolysis of glucose derived HTC carbons is in detailed investigated, in such a way as to understand the effects of this post-functionalisation step on the material properties. A comparison between HTC and direct pyrolysis of biomass derivatives is also presented, in order to highlight the higher degree of chemical structure control allowed by HTC.

In the second part of this thesis (Chapter 5) the chemical activation of the lignocellulosic biomass derived HTC carbon is investigated. The suitability of HTC carbons as precursor for highly porous activated carbons is shown, and a dependence between the chemical structure of the HTC carbons and the subsequent porosity development of the activated carbons is established. Results obtained from preliminary testing of the HTC derived activated carbons for $CO_2$ capture and high pressure $CH_4$ storage are also presented. In the last chapter (Chapter 6) this synthetic route is further extended to protein-rich biomass (i.e. microalgae). The retention of the high N-content of the parent biomass in the derived HTC carbons and their subsequent chemical activation allows the production of highly porous N-doped activated carbons, with high potential for energy storage applications (e.g. supercapacitors).

# CHAPTER 2 – The use of $^{13}C$ solid-state NMR techniques to analyse the HTC carbons chemical structure.

## 2.1 Introduction

The chemical structure elucidation of carbonaceous and coal-like materials has been an intensively investigated topic in the last 50 years. Several characterisation techniques (e.g. FT-IR, XPS, Raman) have been employed to accomplish such a task. However the interpretation of the obtained results has always shown a certain degree of ambiguity, in the case of carbonaceous materials characterised by a high chemical heterogeneity and intricacy.[39]

In the last 25 years, several theoretical and technical developments (e.g. Magic angle spinning (MAS), cross polarisation (CP)), in the field of solid-state nuclear magnetic resonance (ssNMR), have highlighted the high potential of this characterisation method in regard to the chemical structure study of carbonaceous materials. SsNMR generally provides a higher spectral resolution than FT-IR or XPS, for this reason its adoption as characterisation method of choice has rapidly spread.[40-43] Nonetheless the interpretation of $^{13}C$ CPMAS spectrum can still be quite challenging for highly heterogeneous carbonaceous materials (Fig. 2.1)

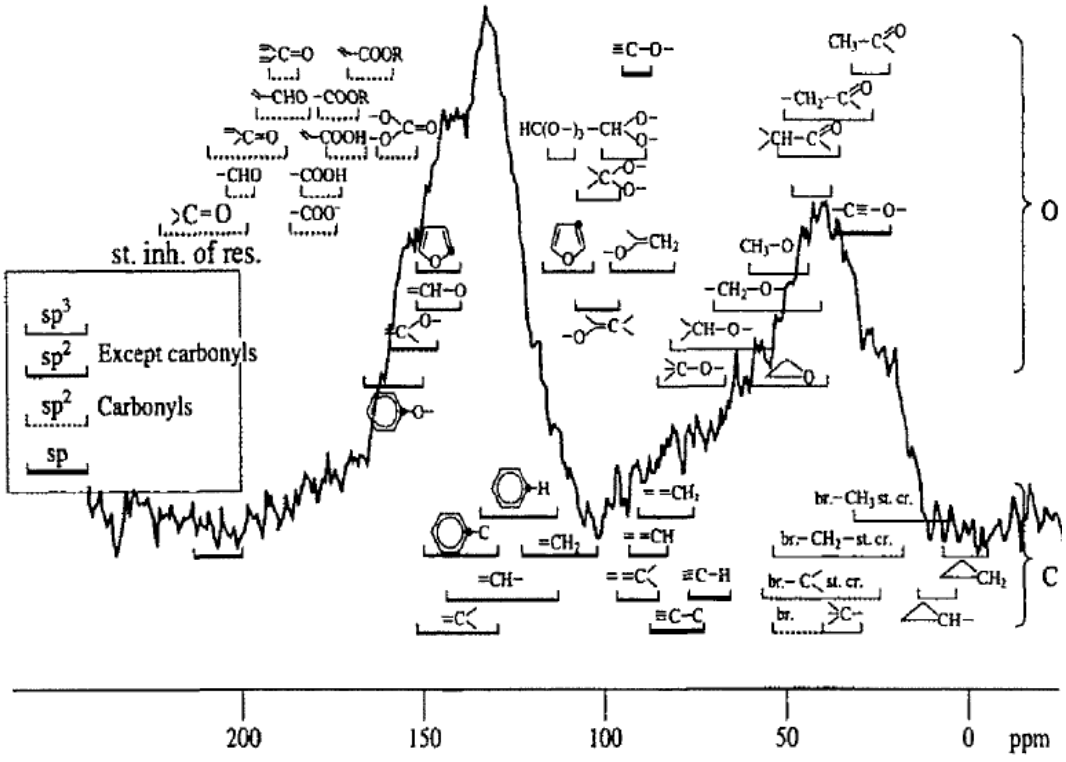


**Figure 2.1:** $^{13}C$ CPMAS spectrum of a whole coal with the NMR chemical shift correlation chart. Reproduced from reference [44]

In regard to the analysis of such complex carbonaceous materials, $^{13}C$ ssNMR provides a further advantage compared to other characterisation techniques: the possibility of using selective pulse sequences to indentify and separate chemical species without ambiguity.[45, 46] Such specifically tailored NMR techniques have been particularly effective and helpful to determine the chemical structure of glucose derived HTC carbon.[35] For this reason, they have also been used extensively throughout this work to characterise the raw biomass derived HTC products.

Due to the central role of ssNMR experiments throughout this work, the following chapter aims to provide a brief introduction to the basic concepts of NMR, its main challenges in solid-state and the routinely employed techniques. Furthermore a qualitative description of the specific pulse sequences used to analyse glucose derived HTC carbon and a summary of the studies developed by Titirici and her coworkers to elucidate its chemical structure are also presented, in such a way as to provide a reference model for the analysis developed in the following chapters.

## 2.2 $^{13}C$ solid state NMR [47-49]

### *2.2.1 NMR basic concepts*

The spin angular momentum (J) of a nucleus is given by:

$$J = \hbar\sqrt{I(I+1)} \tag{2.1}$$

where $\hbar$ is the Planck's constant(divided by $2\pi$) and $I$ corresponds to the nuclear spin. This latter quantity is an intrinsic property of the nucleus depending on its atomic and mass number (Table 2.1).

**Table 2.1:** Nuclear spin values for different elements.

| | |
|---|---|
| **Nucleus** (Nuclear spin) | $^{1}$**H** (1/2), $^{12}$**C** (0), $^{13}$**C** (1/2), $^{15}$**N**(1/2), $^{29}$**Si**(3/2) |

The magnetic moment of a nucleus is proportional to its spin angular momentum:

$$\hat{\mu} = \gamma \ \hat{J} \tag{2.2}$$

Where $\gamma$ is the gyromagnetic constant. The hats indicate that these parameters are quantum mechanical operators.

When a nucleus with nuclear spin (i.e. $I$) equal to 1/2 is placed in an external magnetic field (i.e. $B_0$), it will adopt either a parallel (α-alignment) or antiparallel (β-alignment) alignment (configurations with the highest probability) to the magnetic field in order to minimize the magnetic energy. During the alignment process the nucleus precesses at an angle θ to the magnetic field. The initial value of θ is equal to

the angle that the nucleus polarization axis forms with the magnetic field (i.e. $B_0$) at the moment when $\mathbf{B_0}$ is firstly applied. As time proceeds, θ gradually decreases due to spin-lattice relaxation, and it becomes eventually 0 when the nucleus polarization axis is perfectly aligned with the magnetic field (Fig. 2.2).

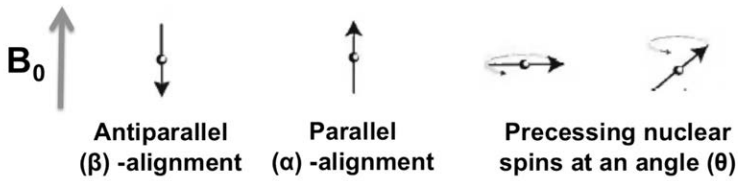


**Figure 2.2:** Precessing nuclear spins at angle θ to the external magnetic field. θ is 0 for nuclear spins in the antiparallel or parallel alignment.

The frequency of precession of the nucleus is called the Larmor frequency ($\omega_0$) and is given by:

$$\omega_0 = -\gamma B_0 \tag{2.3}$$

In standard NMR experiments, radiofrequency (RF) pulses are used to create short-lived secondary magnetic fields (i.e. $B_1$), aimed at disrupting the alignment of the nucleus polarization axis with the primary magnetic field (i.e. $B_0$). The NMR experiment in its simplest version involves a 90° (or π/2) RF pulse (single pulse (SP) experiment) shifting the nucleus polarization axis to the plane perpendicular to the magnetic field (*xy* plane) (Fig 2.3). Once $\mathbf{B_1}$ is extinguished, the nucleus returns back to its low energy position parallel (or antiparallel) to the primary magnetic field while precessing at its Larmor frequency.

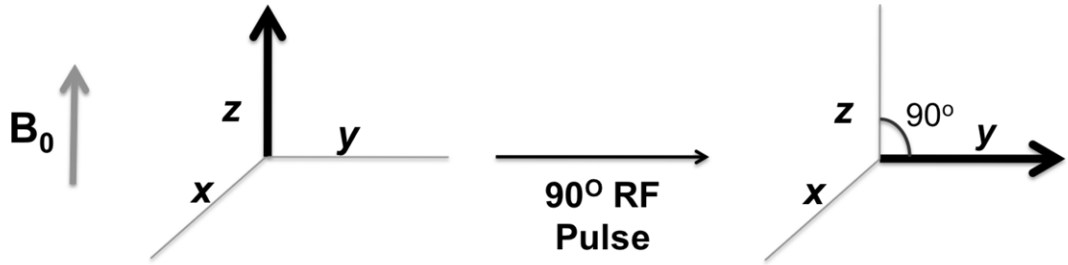


**Figure 2.3:** Nuclear spin polarization axis (black bold arrow) in a magnetic field before and after the application of a 90° RF pulse

NMR spectrometers are equipped with an electrical coil, aligned to the *xy* plane and able to measure the decreasing magnetic energy experienced by the nucleus along the *x* and *y* axes, as it preceedes back to its original position parallel to $\mathbf{B_0}$ (z axis).

This gives rise to a free induction decay (FID) curve, which is then transformed to the desired NMR spectrum by applying the Fourier Transform (FT).

The underlying principle allowing NMR spectroscopy to identify the chemical structure of molecules is that nuclei of the same isotope but belonging to different chemical environments (i.e. functional groups) precess at diverse Larmor frequencies. Such differences arise from the evidence that the effective magnetic field ($B_{ef}$), felt locally by each nucleus, is affected by several magnetic interactions determining its strength. The interaction that is mostly exploited in NMR spectroscopy arises from the uneven distribution of electron clouds within a molecule. Electrons under the influence of an external magnetic field generate an induced proportional and opposite magnetic field, which reduces the strength of $B_{ef}$ according to Lenz's law:

$$B_{ef} = B_0(1-\sigma) \tag{2.4}$$

where σ corresponds to the shielding factor. Highly shielded nuclei ($\sigma \rightarrow 1$) precess at lower frequencies, therefore they resonate at high field (negative or small frequency shifts). Highly deshielded nuclei ($\sigma \rightarrow 0$) precess at higher frequencies, therefore they resonate at low field (large positive frequency shifts). This kind of chemical shift in NMR spectra is referred to as *Isotropic Chemical Shift* or simply *Chemical Shift*.

Therefore, depending on the number of nuclear species present within the analyzed sample, the FID curve may be the result of either a single Larmor frequency (i.e. all nuclear spins belonging to the same chemical environment) or of several ones superimposed. Upon FT of the FID curve, each Larmor frequency is then related to a chemical shift in the spectrum. The known correspondence of specific chemical environments to precise chemical shifts allows determining the chemical structure of the analyzed sample.

### *2.2.2 NMR interactions in solid state*

As anticipated in the previous section, there exist several magnetic interactions affecting locally the magnitude of the magnetic field felt by the nuclei. The one determining the Chemical Shift is the strongest and it is necessary to obtain separation of the peaks relating to different chemical species in NMR spectra. On the other hand the other interactions generally need to be suppressed because they lead to peak broadening. Nonetheless this is not always the case, because under specific circumstances they may be used to investigate particular features of molecules (e.g. bond length, molecule folding).

These magnetic interactions are not a major concern in solution NMR, since the random tumbling of the molecules due to Brownian motion averages them out. On the other hand to obtain such an averaging effect in ssNMR spectroscopy, specific tailored techniques are needed. In this section a brief overview of the magnetic interactions affecting $I = ½$ nuclear spins (i.e. omitting quadropolar interactions), the reasons why they arise and the available techniques to cancel their effects out is presented.[50]

Chemical Shift Anisotropy (CSA)

Electrons distributions in atoms are rarely isotropic in relation to bonding axes. These asymmetries lead to inhomogeneous effects on the magnitude of the magnetic field felt by the nuclei in the surrounding environment, since the extent, the electrons affect the chemical shift at, strictly depends on the orientation of the electron cloud in the molecule and in relation to the external magnetic field. In solids these anisotropic effects are particularly strong (i.e. $10\text{-}10^4$ Hz), since the averaging effect due to Brownian motion characteristic of liquids is not present. Nonetheless a similar result can be achieved if the sample is moved in a liquid like manner. Theoretically a solution is rotating the sample with respect to all its three axes, in such a way that each nuclear spin spends equal amount of times in a position parallel to each of the three axes. However, practically, this is achieved by spinning the sample at high rotational speed (e.g. 5-14 kHz) and at a given angle to the external magnetic field. This technique is commonly known as Magic Angle Spinning (MAS) and it relies on the qualitative observation that if a molecule is spun at very high rotational speeds, due to its constant position change in time, its overall electron cloud is averaged to an ellipsoid. Furthermore if the longitudinal axis of such a spherical object is inclined at an angle of $54.74^o$ (the value of the magic angle), then the ellipsoid shows a perfect symmetry in relation to all three Cartesian axes. During the NMR experiment, this leads each of the nuclear spin to experience an average chemical shift due to all the possible orientations of the electron clouds with respect to the external magnetic field during one rotational period. This averages out the effect of electron clouds anisotropy on chemical shifts in solids.

Dipolar Coupling (DC) [51]

It involves the interaction between the magnetic moments of two like (Homonuclear Dipolar Coupling - HomoC) or unlike (Heteronuclear Dipolar Coupling - HeteroC)

nuclear spins. Each nucleus with a magnetic moment, exposed to an external magnetic field, generates a small secondary field. This will add to or subtract from the effective magnetic field magnitude perceived by the nuclei in its proximity. The strength of dipolar coupling (i.e. $10^4$-$10^5$ Hz) depends on three main parameters:

- The magnitudes of the gyromagnetic constants ($\gamma$) of the involved nuclei. Higher gyromagnetic constant values lead nuclei to develop larger magnetic moments generating stronger secondary magnetic fields.
- The internuclei distance. The strength of dipolar coupling is inversely proportional to the cube of the internuclei distance. Therefore this magnetic interaction decays relatively fast as the distance between nuclei increases.
- The angle ($\theta$) that the internuclei axis forms with the external magnetic field. The magnitude of dipolar coupling is proportional to $(3\cos^2\theta - 1)$, therefore if the orientation of the sample is chosen in such a way that this term equals 0, then the dipolar coupling interaction is suppressed.

Dipolar coupling can be reduced via MAS. The positioning of the sample at a $54.74^o$ angle to the external magnetic field partially suppresses this interaction, since the term $(3\cos^2\theta - 1)$ tends to 0, as previously explained. However MAS is mostly effective for nuclei with a low gyromagnetic constant (i.e. $^{13}C$, $^{15}N$). Whenever high gyromagnetic constant nuclear spins (i.e. $^1H$) are involved in the coupling interaction, MAS may not be sufficient and other decoupling techniques are then required. These are specific for the HeteroC and HomoC cases.

*Heteronuclear decoupling (HeteroD)* involves the use of RF pulses rotating the nuclear spins of the heteroatom, whose coupling magnetic interaction needs to be decoupled. The rotation is induced in such a way that the decoupled nuclei spend exactly the same amount of time in their parallel and antiparallel alignments with respect to the external magnetic field. This leads to the averaging out of the HeteroC effect on the nuclear spins, whose resonance frequency is being detected during the experiment.

*Homonuclear Dipolar Decoupling* (HomoD) is also based on the use of RF pulses. However in this case the cycle is more complex than for HeteroD, since the coupled nuclear spins resonate at the same frequency, as a consequence it is not possible to rotate only one of them at a time. The only possible solution is to rotate the coupled spins as a unique unit and in such a way that they spend equal amounts of time in

positions parallel to each of the three axes over one cycle. If the pulse sequence is carried out over a period of time that is much shorter than the spin-lattice relaxation time frame, then the HomoC is averaged out.

J-coupling (J-C)

J-C is also present in solution NMR, since it is not averaged out. It is also known as indirect dipolar coupling or electron-coupled spin interaction. The reason is that, while dipolar coupling is a through space interactions, J-c takes place across the bond meaning that the magnetization is transferred from a nuclear spin to another one through the electrons that are confined in the bond between them. As a consequence J-c takes place only between nuclei belonging to the same molecule. However it is much weaker (i.e. 10-150 Hz) than CSA or DC, as a result it is not a major source of peak broadening.

### *2.2.3 $^{13}C$ solid state NMR challenges and Cross Polarisation*

In ssNMR experiments it is common to obtain very broad peaks for $^{1}H$ NMR spectra due to the strong HomoC. Such spectra yield very few information regarding the chemical structure of the analyzed molecules, since the chemical shift peaks cannot be assigned due to lack of sharpness. For this reason it is preferable to analyze nuclei with a relatively small gyromagnetic constant, such as $^{13}C$, since the effects of HomoC are relatively negligible in this case. However $^{13}C$ ssNMR measurements also present some challenges due to some intrinsic properties of the $^{13}C$ nuclei:

- Low isotope – The carbon NMR active isotope (i.e. $^{13}C$) possesses a low natural abundance (1.108%) leading to weak signal intensity whenever a SP $^{13}C$ NMR spectrum is acquired from a non-enriched sample.
- Low gyromagnetic constant – The NMR signal intensity depends on the nuclear spins population difference between the two allowed energy states (for a $I = ½$ nuclear spin). Higher the excess of spins in the lower energy state, greater the probability of resonance, stronger the NMR signal. According to the Boltzmann's distribution law, the ratio of nuclei in the two energy states is determined by their energy difference, which is proportional to the gyromagnetic constant (i.e. $\gamma$). As a consequence for low gyromagnetic constant nuclei the nuclear spin population distribution between the two energy levels is more homogeneous, leading to a weaker NMR signal.[52]

- Long spin-lattice relaxation time –In regard to an NMR experiment this parameter refers to the time necessary for the system to achieve thermal equilibrium, corresponding to the development of a macroscopic magnetization throughout the sample (i.e. largest proportion of nuclei aligned along the external magnetic field). Since during an NMR experiment between the acquisition of two consecutive scans thermal equilibrium needs to be re-established, the value of this constant is a key factor determining the total experiment length. Generally spin lattice relaxation times are much higher in solids than in liquids. Furthermore in the case of $^{13}C$ nuclear spins the spin-lattice relaxation time is relatively high if compared to quick relaxing nuclear spins, such as $^{1}H$ (generally one order of magnitude faster).[53] This results in a considerable increase in the duration of each experiment.

These sensitivity issues are partially improved by specific tuning of the NMR experiment parameters, such as using greater sample amounts, lowering the acquisition temperature, increasing magnetic field strength or acquiring a higher number of scans. However these adjustments allow only marginal improvements of the spectra resolution. Another available solution to improve the relatively low abundance of the $^{13}C$ nuclei is isotopic enrichment of the sample. This procedure leads to a stronger signal intensity and therefore to a better spectra resolution. However it can be rather expensive, therefore isotopic enrichment may not be the solution of choice, when the NMR analysis of several samples is required for a systematic investigation.

A major breakthrough in the field of NMR analysis of nuclei, characterised by low isotopic abundance and small gyromagnetic constant, was achieved with the development of Cross Polarization (CP). This technique relies on the principle that magnetization can be exchanged between different nuclear spins via the dipolar magnetic interaction ( I is conventionally used to represent abundant nuclei, e.g. $^{1}H$, S scarce nuclei, e.g. $^{13}C$) . However such an energy exchange can only take place effectively if the Hartmann-Hahn principle is satisfied, which requires both spin systems to be precessing at approximately the same frequency. The energy gap between the different nuclear spins can be bridged by employing two different sets of RF pulses. Each of them generates a secondary magnetic field ($B_{1I}$ and $B_{1S}$), affecting respectively the precession frequency of only one of the two nuclear spins. The RF pulses are tuned according to the following equation:

$$\frac{B_{1I}}{B_{1S}} = \frac{\gamma_{1S}}{\gamma_{1I}} \tag{2.5}$$

If the condition expressed in eq 2.5 is satisfied, then the magnetization transfer can take place. In the case where I and S correspond respectively to $^{1}H$ and $^{13}C$ (i.e. $^{13}C$ CP), since the ratio of the gyromagnetic constants of these two nuclei is 4, theoretically the magnetization of $^{13}C$ nuclear spins experiences a magnitude increase of an equivalent factor leading to a stronger signal during detection. A second advantage provided by $^{13}C$ $\{^{1}H\}$ CP experiments is that the time gap between the acquisition of two successive scans depends on the $^{1}H$ spin-lattice relaxation time constant leading to a considerable reduction of the NMR experiment duration compared to $^{13}C$ SP experiments.

The pulse sequence used for $^{13}C$ $\{^{1}H\}$ CP NMR experiments initiates with a $\pi/2$ pulse aimed at rotating the $^{1}H$ nuclear spins into the *xy* plane (Fig. 2.4). Subsequently CP is applied to the $^{1}H$ and $^{13}C$ nuclei for a time $\mathbf{t_{cp}}$ (varying from milliseconds to μs). Lastly the protons are decoupled while the signal produced by the precessing $^{13}C$ nuclear spins is acquired.

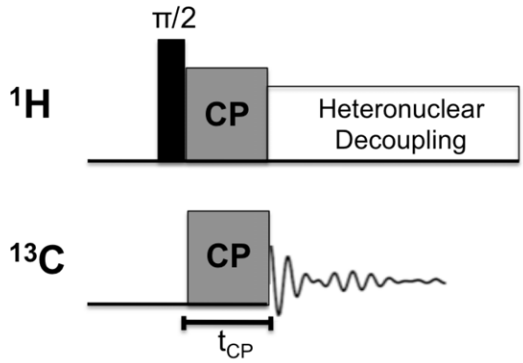


**Figure 2.4:** Pulse sequence for basic $^{13}C\{^{1}H\}$ CP NMR experiment

The rate of magnetization increase due to CP strongly depends also on the internuclei distance between the $^{13}C$ and $^{1}H$ nuclear spins. Protonated carbons experience a strong dipolar coupling, as a consequence the magnetisation transfer in such species is quicker and decays faster than in non-protonated carbons. For this reason, when designing CP NMR experiments, the $\mathbf{t_{cp}}$ value has to be chosen carefully in such a way that the obtained spectra are not utterly biased towards a certain group of species.

Due to the complexity of involved magnetic interactions and the strong dependence of the peak intensities on the $\mathbf{t_{cp}}$, the main drawback of CP is that it

cannot be used for a strict quantitative analysis. Nonetheless spectra, obtained at a carefully chosen value of $\mathbf{t_{cp}}$, are still a reliable approximation that can be used for pointing out the most abundant species within the analyzed sample.

### *2.2.4 Advanced $^{13}C$ NMR techniques*

In the previous sections routinely employed ssNMR tools have been introduced. In standard experiments, a combined use of these techniques generally yields well-resolved spectra allowing predominantly the identification of the functional groups present within the analyzed sample. Nonetheless this may not be sufficient when a more detailed analysis of the different chemical environments connectivity is required. For these studies specific NMR experiments are designed, exploiting pulse sequences that are tailored according to the investigated molecular feature. Because of this high specificity, advanced NMR techniques available in literature are numerous. Therefore it is unfeasible and beyond the scope of this chapter to provide a complete overview. For this reason this section will mostly focus on the techniques that have been employed to study the structure of hydrothermal carbons.

Inversion Recovery Cross Polarisation (IRCP)

It is usually employed to distinguish between protonated and non protonated carbons and it can be considered as a modified version of simple CP.[54] IRCP relies on the principle that magnetization transfer during CP is faster in protonated rather than non-protonated carbons due to stronger HeteroC.

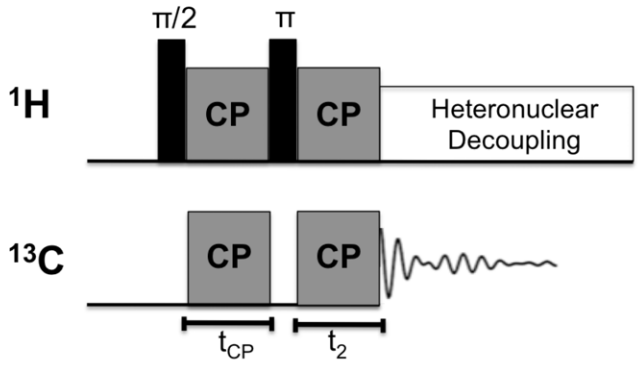


**Figure 2.5:** Pulse sequence for IRCP experiment

The pulse sequence is very similar to the CP one. The only modification involves an inversion of the proton magnetization direction from the *y* to the *–y* axis, before CP is ceased (Fig 2.5). During $\mathbf{t_2}$ the $^{13}C$ nuclear spins gradually tend to realign with the proton magnetization parallel to the *–y* axis. This leads to a decrease of the detected

$^{13}C$ *xy* plane magnetization, which may eventually become negative and consequently reverse the sign of the FID curve intensity. Upon FT of such FIDs the $^{13}C$ nuclear spins, whose net magnetization along the y axis has been reversed, are characterised by negative peaks in the NMR spectrum.

The probability of a nuclear spin showing a negative peak during an IRCP experiment, depends on the rate of magnetization transfer from the protons. Protonated carbons tend to realign with the reversed $^{1}H$ magnetization relatively fast due to the strong HeteroC. As a consequence, even at short $\mathbf{t_2}$ values, they show negative peaks in NMR spectra. On the other hand the non protonated carbons have a more sluggish response to the $^{1}H$ magnetization inversion. As a result even at long $\mathbf{t_2}$ values, the intensity of their NMR peaks is only reduced, but it never becomes negative. The relative rates of $^{13}C$ nuclei polarization follow the subsequent order:

$$CH_3 \text{ (Static)} > CH_2 > CH > CH_3 \text{ (rotating)}, C \text{ (non protonated)}$$

Very mobile methyl groups behave like non-protonated carbons due to the fact that they cross polarize slowly because of rapid molecular motions.

Insensitive nuclei enhanced by polarisation transfer (INEPT)

It exploits the J-coupling interaction between $^{1}H$ and $^{13}C$ nuclear spins. For this reason it is a very powerful technique to investigate the protonation of carbon atoms. INEPT relies on the principle that if polarisation inversion of only the $^{1}H$ nuclei, coupled to the α-aligned $^{13}C$ nuclear spins (i.e. parallel alignment to the external magnetic field) takes place, the induced population distribution inversion of the respective energy levels leads to a dramatic increase of the signal intensity acquired from the resonance of protonated $^{13}C$ nuclei.

Practically this effect is achieved by applying a sequence of pulses (Fig 2.6), which refocuses the $^{1}H$ magnetization along the z-axis in such a way that the protons that are coupled to the α-aligned $^{13}C$ nuclei have opposite polarization than the ones coupled to β-aligned $^{13}C$ nuclear spins. This polarization rearrangement of the $^{1}H$ nuclei affects the overall $^{13}C$ nuclear spins (only those experiencing J-coupling) magnetization in such a way that, when its rotation to the xy plane takes place due to the last $90^{o}$ pulse, the overall $^{13}C$ signal shows a fourfold intensity increase upon refocusing of all the magnetization *xy* components and decoupling of the $^{1}H$-$^{13}C$ interaction.

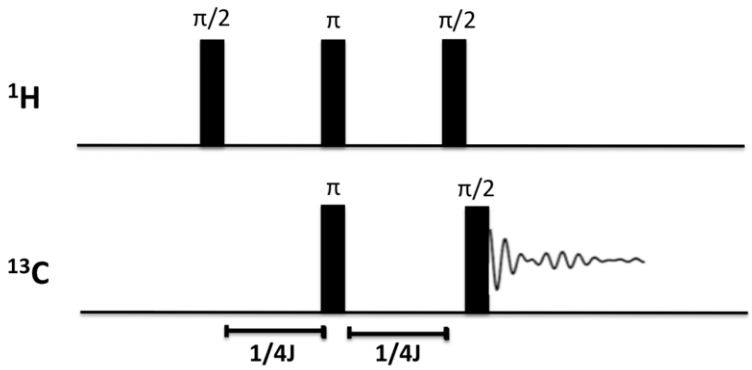


**Figure 2.6:** Pulse sequence for INEPT experiment (N.B. *J* is the $^{1}H - ^{13}C$ coupling constant).

The increase in signal intensity is observed for $^{13}C$ nuclear spins that experience direct J-C with the protons, as a consequence INEPT experiments only show protonated carbons.

2D NMR techniques

These NMR experiments allow studying the magnetic interactions between like (homonuclear) or unlike (heteronuclear) nuclear spins. Therefore they are particularly useful to visualize the connectivity between the chemical environments comprising the structure of the analyzed molecules. Practically this is achieved via the analysis of the cross peaks, characterising the 2D NMR spectra usually presented in the form of contours plots. In this section the standard format generally characterising all 2D NMR experiments is presented. Subsequently a more detailed description of the 2D NMR experiments used for the analysis of HTC carbons is provided (i.e. HETCOR $^{1}H$-$^{13}C$ and Homonuclear $^{13}C$ DQ-SQ experiments).

Each 2D experiment is generally comprises of 4 different phases (Fig.2.7):

- Preparation ($\tau_p$) – The nuclear spins are allowed to achieve thermal equilibrium. Then the magnetization is usually rotated in the *xy* plane ($\pi/2$ pulse) (in heteronuclear experiments, the $\pi/2$ pulse affects only one of the two nuclear spins). In some specific cases a more complex sequence of pulses may be used before the final $\pi/2$ pulse.
- Evolution ($t_1$) – The magnetization evolves freely according to the experiment settings (i.e. MAS, decoupling/recoupling pulse sequences)
- Mixing ($\tau_M$) – Pulse sequences are applied to the nuclear spins in such a way as to enhance specific heteronuclear or homonuclear magnetic interactions depending

on the nature of the experiment. Routine procedures comprehend CP, hetero/homo decoupling/recoupling.

- Detection ($t_2$) – The nuclear spins precession frequency is detected.

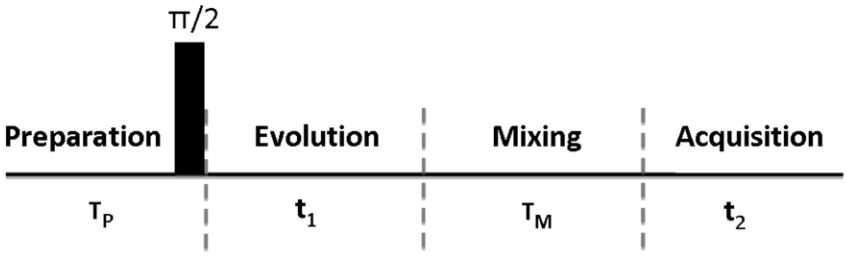


**Figure 2.7:** General format of a 2D NMR experiment

Such a sequence is repeated several times at different $\mathbf{t_1}$ intervals. A FT transform is finally applied to both the direct ($t_2$) and indirect ($t_1$) dimensions in order to generate the 2D NMR spectrum. The basic concept of 2D NMR experiments is that the detected signal during $\mathbf{t_2}$ depends on the magnetic "events" taking place during both the evolution (i.e. $t_1$) and mixing (i.e. $\tau_M$) periods. As a consequence the NMR spectra, recorded during $\mathbf{t_2}$, can be used to reconstruct the magnetic interactions history of the detected nuclear spins yielding detailed information regarding their bonding patterns.

$^{1}$H-$^{13}$C Heteronuclear Correlation experiment (HETCOR )

It is used to correlate the chemical shifts of $^{1}$H and $^{13}$C nuclear spins. Its pulse sequence follows the structure of standard 2D NMR experiments (Fig.2.8). The $^{1}$H-$^{13}$C dipolar coupling is suppressed in both the evolution and detection phases (i.e. $t_1$ and $t_2$) while CP is applied during the mixing one (i.e. $\tau_M$) to allow magnetization exchange between the protons and the $^{13}$C nuclei. Since the rate of magnetization transfer is different for protonated and non protonated carbons (as seen in the previous sections), tuning the $\tau_M$ allows to control the extent, the $^{1}$H-$^{13}$C interaction extends to. Using this NMR technique it is thus possible to obtain information on the bonding patterns between protons and carbons within the analyzed molecules.

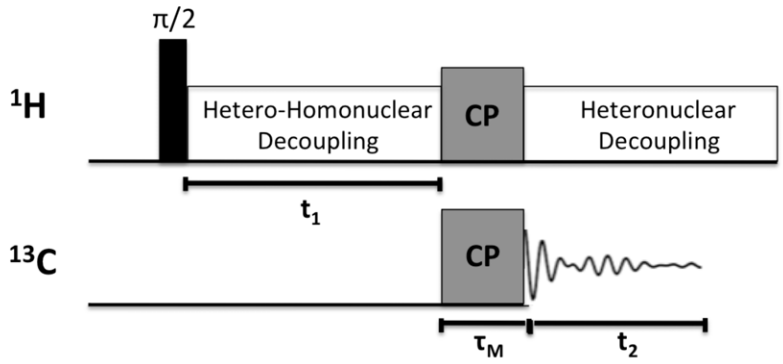


**Figure 2.8:** Pulse sequence for HETCOR experiment

$^{13}$C Homonuclear Double-Quantum-Single-Quantum (DQ-SQ) correlation experiment

It shows the interactions between $^{13}$C nuclear spins. CP is firstly applied to enhance the carbon magnetization (Fig 2.9). Subsequently heteronuclear decoupling is introduced and maintained throughout the whole experiment to remove $^{1}$H-$^{13}$C coupling. As previously explained, MAS averages HomoC out for low gyromagnetic constant nuclei (i.e. $^{13}$C), as a consequence after the evolution period (i.e. $t_1$) homonuclear recoupling is required to observe $^{13}$C-$^{13}$C interactions upon acquisition of the signal in the detection phase. The recoupling pulse sequence plays a crucial role in homonuclear correlation experiments, since it allows reintroducing selectively only the required type of interactions. In this case a DQ filter is applied within the recoupling sequence allowing to detect only those resonances arising from dipole-coupled pairs of $^{13}$C spins and to suppress those from isolated, unpaired spins. [55]

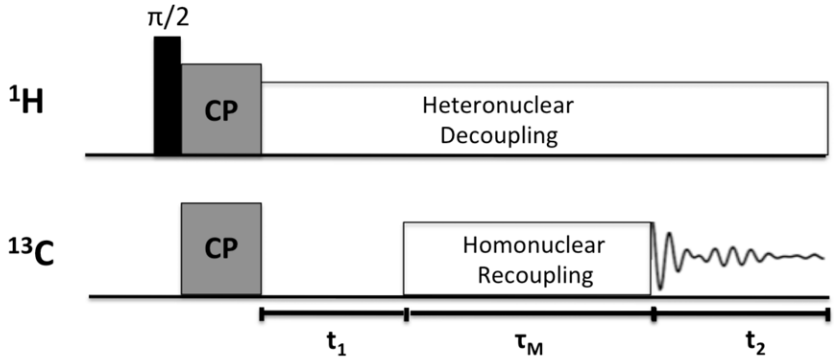


**Figure 2.9:** Pulse sequence for 2D $^{13}$C-$^{13}$C homonuclear correlation experiment.

Due to the steep decay of dipolar coupling as a function of internuclear distance, $^{13}$C DQ-SQ experiments show only the resonances, arising from $^{13}$C nuclei that are in each other proximities.[56] Furthermore in the case of uniformly $^{13}$C-labeled samples the distance range of the detected interactions does not extend beyond one bond

length, because, due to the presence of strong local couplings, weak interactions between relatively distant nuclear spins cannot be recoupled effectively. This effect is known as dipolar truncation.[57]

## 2.3 Advanced $^{13}C$ solid state NMR studies of glucose derived HTC carbon chemical structure.[34, 35]

The chemical structure of monosaccharides derived HTC carbons has been extensively studied by Titirici and her co-workers. Several characterisation techniques have been employed to determine the main building blocks of such carbonaceous materials (e.g. FT-IR, XPS, Raman). However the $^{13}C$ ssNMR studies are the real core of their characterisation analysis, since they do not only allow identifying the functional groups, present in HTC carbons, but also their inter-connectivity.

A preliminary $^{13}C$ ssNMR study on HTC carbons derived from different mono and polysaccharides (i.e. fructose, glucose, starch, xylose) highlighted that the main factor affecting the chemical nature of the HTC product is the structure of the parent sugar. Pentose (e.g. xylose) derived HTC carbons possess a more marked aromatic character than hexose (e.g. glucose) ones. Such a difference is demonstrated by a more intense peak at $\delta$ = 125-129 ppm for the former material, characteristic of aromatic carbons belonging to graphitic or long range conjugated double bonds structures. Different HTC reaction intermediates may be the explanation for such a finding. Pentose sugars are expected to be dehydrated to furfural, when hydrothermally treated. On the other hand 5-HMF is the main dehydration product derived from hexoses. As reported in literature, the reactivity of these two intermediates is indeed different, as a consequence it also reflects in the chemical structure of the respective HTC carbons.[58]

Further Gas-chromatography mass spectrometry (GCMS) and solution $^{13}C$ NMR on the glucose system confirmed that the major intermediate in the reaction mixture is 5-HMF. This finding, coupled to the evidence that the $^{13}C$ ssNMR spectrum of glucose derived HTC carbon is characterised by the presence of intense furan moieties resonances, led to the conclusion that polymerisation/condensation reactions involving 5-HMF monomers are the route of formation of HTC carbon. However, although the literature available on furan chemistry is extensive, a straightforward and detailed mechanism could not be proposed, since 5-HMF is known to undergo a plethora of reactions under hydrothermal conditions (e.g. self-condensation,

substitution on the furan ring). Furthermore other degradation products (e.g. levulinic acid) are present within the reaction mixture and may at the same time react with 5-HMF units (e.g. aldol condensation). For these reasons the overall HTC mechanism most likely comprises of several parallel reactions involving 5-HMF as reacting unit and taking place at different extents depending on the processing conditions.

Despite of the HTC mechanism complexity, the $^{13}C$ ssNMR studies highlighted the presence of a major building unit. Glucose derived HTC carbon, synthesised at 180$^{o}$C, is majorly composed of highly cross-linked furan moieties. In the next two sections, a summary of the experiments, employed by the Titirici group to demonstrate the presence of such subunit, is given.

### *2.3.1 HTC carbon functional groups*

Fig. 2.10 shows the $^{13}C$ spectra of glucose derived HTC carbon at 180$^{o}$C obtained by employing different pulse sequences. The peak deconvolution and assignment is based on the DQ-SQ map projection, since this spectrum allows better resolution and identification of the individual peaks. Several interesting highlights can be observed:

- For HTC carbons the $^{13}C$ spectrum obtained at a contact time equal to 3 ms is a fairly good approximation of a quantitative SP experiment. This is an important piece of information, since throughout this work CP experiments will be extensively employed, because of the shorter acquisition times required.
- All four NMR signatures can be divided in 3 separate regions. Region I (or aliphatic region, 0-80 ppm) is related to $sp^3$ hybridised carbons. Region II (or aromatic region, 100-160 ppm) is characteristic of $sp^2$ hybridised aromatic carbons, with the high end of the range corresponding to oxygen containing aromatic rings. Region III (175-225 ppm) is typical of resonances that are attributed to oxygen containing functionalities, such as carboxylic acids, ketones, aldehydes, esters.
- As anticipated, the aromatic region (II) of all four spectra is predominantly characterised by furan moieties peaks. **J** and **I** arise from the α-carbons (δ =140-151 ppm), while **G** and **F** are due to the β-carbons (δ =110-118 ppm). Such a finding is indicative of the central role of furan building blocks within the HTC structure.

Specifically tailored $^{13}C$ NMR experiments have also been very helpful in determining bonding features, peculiar of functional groups corresponding to specific

resonances. The first crucial piece of information about the cross-linked nature of the furan units is given by the INEPT experiment (Fig 2.10c). The peaks corresponding to furan α-carbons (i.e. δ = 146 – 151 ppm) cannot be seen with this pulse sequence. As previously explained, INEPT is specific for carbons bonded to hydrogen atoms, as a consequence the non-protonated nature of the 2,5 furan carbons can be deduced. Furthermore the disappearance of the δ ≈ 208 ppm peak in the INEPT spectrum also shows the absence of aldehydes indicating these functional groups as major reactive sites in the formation of HTC carbon from 5-HMF. Such a speculation is also confirmed from HETCOR experiments (not shown), where no crosspeak corresponding to aldehydes can be observed.

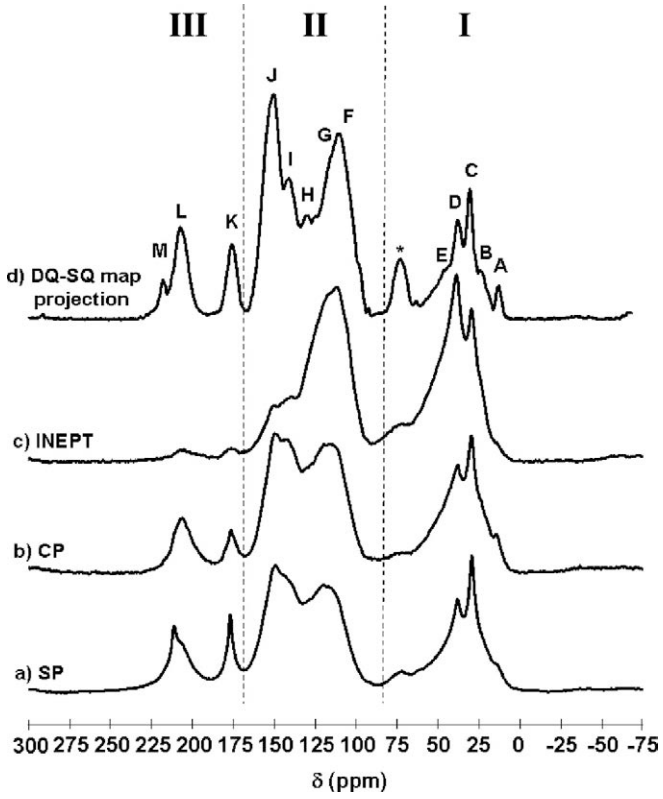


**Figure 2.10:** $^{13}$C MAS NMR spectra of glucose derived HTC carbon at 180°C recorded with different pulse sequences: (a) SP, (b) CP, and (c) INEPT. (d) Skyline projection of the 2D 13C−13C DQ−SQ experiment. Reproduced from reference [35]

The non-protonated nature of the α-carbons and of the **L** peak is also confirmed by $^{13}$C CP experiments carried out at different contact times (Fig 2.11b). The typical behaviour of quaternary carbons can be observed, the intensity increase of these peaks is very sluggish as contact time increases meaning that their magnetisation enhancement, due to CP, is taking place at a reduced rate. Interestingly the same kind of trend can be observed for the **G** peak, whilst **F** shows instead a typical behaviour of

protonated carbons. This last finding, coupled to the observation that **G** and **F** have approximately the same intensity in the $^{13}C$ SP spectrum (Fig. 2.10a), leads to the rough estimate that in each furan unit one of the two β-carbons is non-protonated (Fig 2.11a).

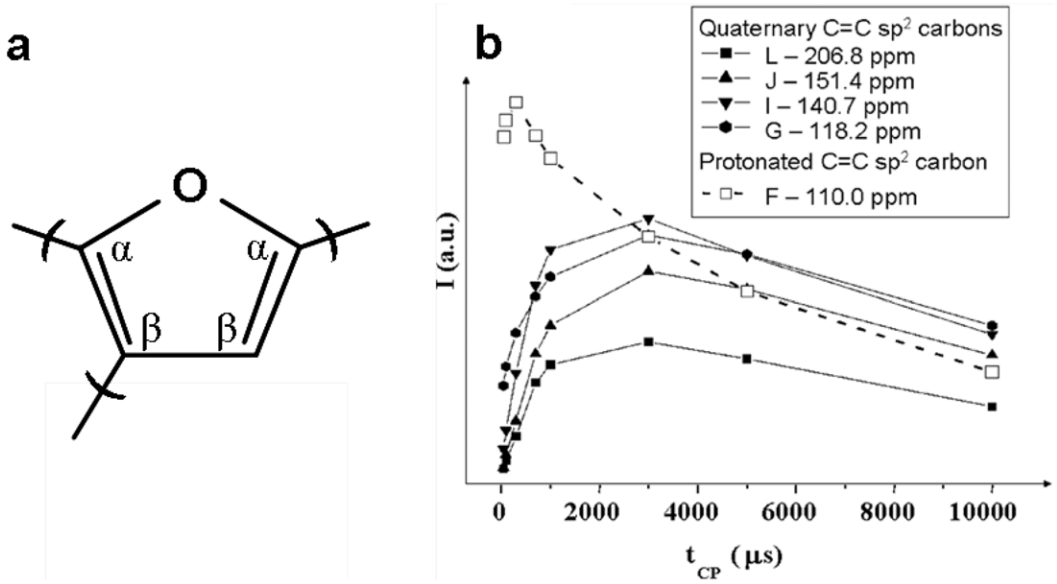


**Figure 2.11:** a) Furan unit bonding patterns as deduced from $^{13}C$ NMR experiments. b) Dependence of the peak intensities in the aromatic region on CP contact time ($t_{CP}$). 2.14b is reproduced from reference [35] .

As previously shown, IRCP experiments are a powerful tool to determine if a carbon has a primary, secondary or tertiary bonding structure. In the case of HTC carbons (not shown), this kind of analysis shows that peaks **B** and **D** have negative intensity upon polarization inversion, as a consequence they can be assigned to methylene groups. On the other hand peak **A** maintains a positive intensity, as a result it is most likely due to mobile methyl groups. Peak **C** instead does not show such a straightforward behaviour as the others, this might be indicative of a multicomponent nature of the peak.

### *2.3.2 HTC carbon bonding patterns*

As previously explained, 2D $^{13}C$ homonuclear DQ-SQ experiments are a powerful tool to deduce the main structural units and the major bonding patterns of a carbonaceous framework structure. *On* diagonal peaks indicate $^{13}C$ spin pairs, belonging to equal chemical environments, while *off* diagonal cross-peaks show the linkage between carbons that are present in different functional groups.

This $^{13}C$ NMR technique was used to study the chemical structure of HTC carbon synthesised at 180 $^{o}C$ (Fig. 2.12). The aromatic region (II—II) of the 2D spectrum is characterised by very intense *on* diagonal (red full dots) and *off* diagonal (red solid lines) crosspeaks. Their origins (F-F, G-G, I-I, I-J, J-F, J-G) are consistent with the previous experiments highlighting that the major building unit of HTC carbons is the furan ring. However because of the nature and intensity of some of these cross correlations, it is possible to speculate that they may also arise because of bonds between different furan units. The intense **J-F** crosspeak can be attributed to two furan rings connected via a carbon double bond (Fig 2.13a ). Such structure may arise from the self-condensation of two furan units.[59] Furthermore the on diagonal **I-I** and the off-diagonal **I-G** and **J-G** peaks can also be indicative of structures formed by two furans linked directly trough a covalent α-α or α-β bond (Fig 2.13b). These moieties may be the product of substitution reactions, taking place on the furan aromatic ring.[58]

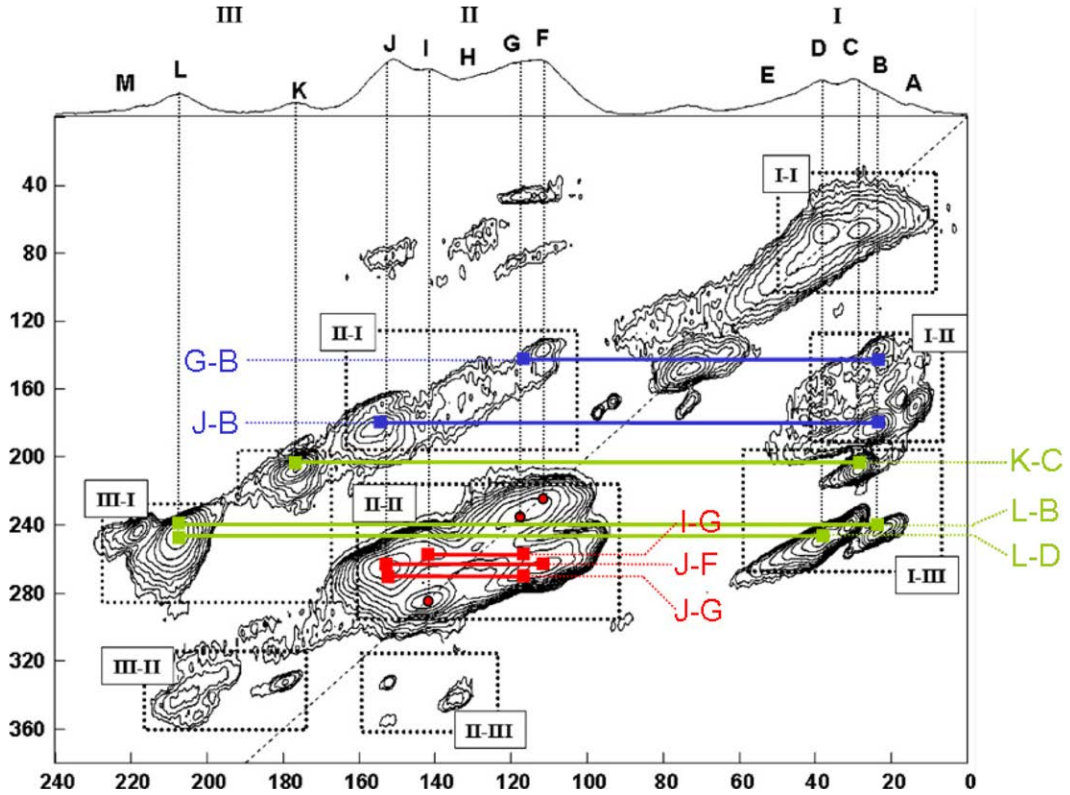


**Figure 2.12:** 2D $^{13}C$ DQ-SQ MAS NMR correlation spectrum recorded for glucose derived HTC carbon synthesised at 180 $^{o}C$. Adapted from [35]

Intense off diagonal crosspeaks are present between the aromatic and the aliphatic region (blue solid lines). **J-B** and **G-B** cross-correlations underline the close connection between the carbons of the furanic rings and the ones of methylene

groups. The **J-B** crosspeak, in particular, due to its high intensity suggests that most likely furan units may be inter-connected at positions 2 and 5 by a methylene group (Fig. 2.13c ). Such bonding patterns are known to form *via* etherification reaction and subsequent formaldehyde elimination.[59]

Interestingly no intense cross peaks are observed in the II-III region. This evidence highlights that the carbons of the furanic rings are not directly connected to oxygen containing functional groups, such as ketone or carboxylic acids. On the other hand these latter species are strictly related to the aliphatic region by several very intense crosspeaks ( K-C, L-B, L-D, green solid lines). Such bonding patterns may either arise because of levulinic acid molecules embedded within the carbon matrix, or because of aldol condensation reactions of such species with the furan units (Fig 2.13d ).[60, 61]

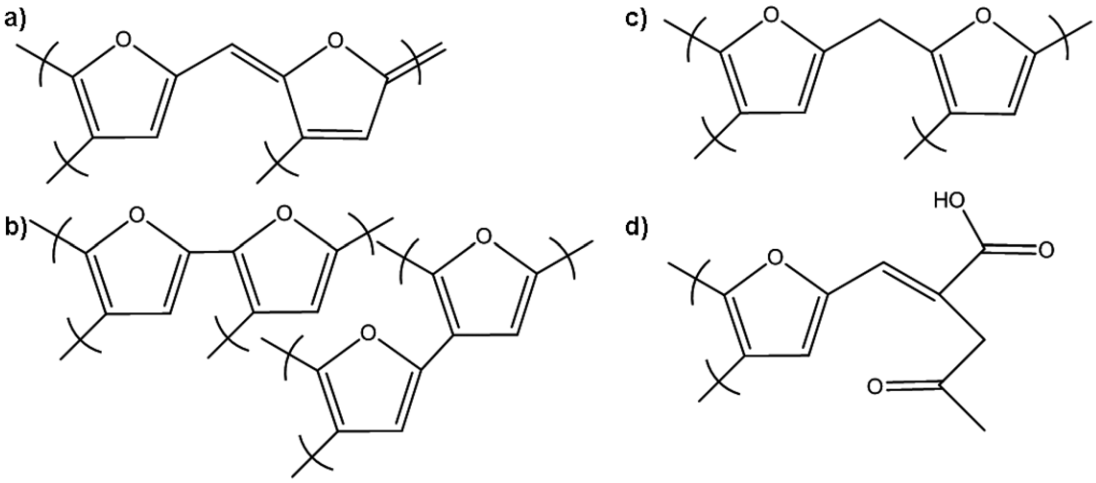


**Figure 2.13:** Major building units of glucose derived HTC carbon synthesised at 180°C

Overall the detailed $^{13}C$ ssNMR study of the HTC carbon, developed by Titirici and her coworkers, highlights the high abundance of cross-linked furan units within the carbon framework structure. However, as confirmed by the complexity of the 2D $^{13}C$ homonuclear spectrum, it also shows a high heterogeneity of bonding patterns arising from the several reactions (e.g. self-condensation, substitution aldol condensation, etherification) that 5-HMF may undergo under hydrothermal conditions.

# CHAPTER 3 – Morphological and structural differences between glucose, cellulose and lignocellulosic biomass derived HTC carbons.

## 3.1 Introduction

HTC has so far proven to be an effective means of conversion of biomass-derived precursors (e.g. monosaccharides) into functionally rich carbonaceous materials. To further highlight the potential of HTC processing with regards to the evolving concept of the "Bio-Refinery", it is advantageous to extend the range of suitable carbon precursors to lignocellulosic biomass, which would guarantee a readily accessible, inexpensive and carbon negative feedstock supply.[62] The use of such biomass, as a raw material for HTC, may in principle seem straightforward, since the main component is cellulose, a β(1→4)glucose polymer (see section 3.2). However the higher chemical heterogeneity and structural complexity of lignocellulosic substrates represents one of the major challenges in terms of biomass utilisation, not only with regard to HTC, but in the wider concept of the aforementioned "Bio-Refinery".[63, 64]

The need for a detailed study focusing on the conversion of lignocellulosic biomass into HTC carbon is thus evident. For the purpose of this investigation, rye straw was used as a model lignocellulosic substrate. This biomass is a by-product of the cereal industry and consists of the dry plants stalks remaining once the grains have been collected. As it is typical for all lignocellulosic biomass, the three main predominant components are cellulose, hemicellulose and lignin (Table 3.1).

**Table 3.1:** Rye straw composition.

| Cellulose | Hemicellulose | Lignin | Others |
|---|---|---|---|
| 41.2 | 21.2 | 19.5 | 18.1 |

Rye straw was chosen among all the other available lignocellulosic biomass due to three main reasons. It is available at reduced costs (*ca.* 0.2-0.4$/Kg),[65] whilst Germany is the third largest producer of rye in the world,[66] therefore its supply (specifically on a national level) is not a major concern. Furthermore it possesses a medium lignin content, as a result it is a suitable model lignocellulosic substrate to investigate the role of this polyaromatic component during the HTC conversion.

In this chapter, an investigation highlighting the effects of temperature and reaction time on the morphology and chemical structure of HTC carbons, produced from rye straw and its representative individual components (i.e. cellulose, lignin), is presented.

The chemical structure of glucose-derived HTC carbon is used herein as a reference model to the more complex lignocellulosic biomass system. A short description of the carbon precursors will also be provided to highlight how structural differences, on a molecular level between the used substrates, affect their HTC conversion mechanism.

## 3.2 The carbon precursors' structure[67]

*Glucose*

Glucose is an aldol hexose sugar and may exist in the form of five different isomers. Whilst one of the isomers represents an open chain structure, the other four are cyclic and referred to as α-, β-glucopyranose and α-, β- glucofuranose. The α or β classification depends on the orientation of the hydroxyl group on the anomeric carbon (position 1). In the β-isomers this hydroxyl group is in the equatorial position, whilst in the α-isomers adopts an axial conformation (Fig 3.1).

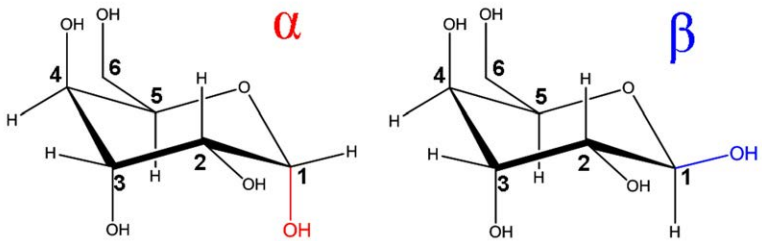


**Figure 3.1:** α- and β-glucopyranose isomers structures.

*Amylose*

After amylopectin, amylose is the second most abundant glucopolymer to be found in starch-based biomass. It is an unbranched polymer of the glucopyranose isomer. The successive hexose monomers are connected via α(1→4) glycosidic bond enabling a degree of flexibility or rotation.[68] As a result, favoured by intra-strand H-bonding, the amylose polymer chain typically adopts an helix polymer arrangement by itself or a double helix structure with a second amylose chain (Fig 3.2). Such a molecular conformation does not allow close packing of the amylose strands (as in cellulose), leading to its solubility in water at mild processing conditions (60-70°C).[69]

*Cellulose*

Cellulose is the main component of plants and the most abundant biopolymer on earth.[6, 70] As with amylose, it is an unbranched polymer of the glucopyranose isomer. However in cellulose the glucose monomers are linked via a β(1→4) glycosidic bond,

resulting in linear self-associating polymer arrangements. The resulting molecular structure generates extensive intra- and intermolecular H-bonding and consequential close packing, leading in some cases to highly crystalline polymeric systems (Fig. 3.2).[71] This structure results in limited water solubility and the need of much higher temperatures than those required for the solubilisation of amylose.

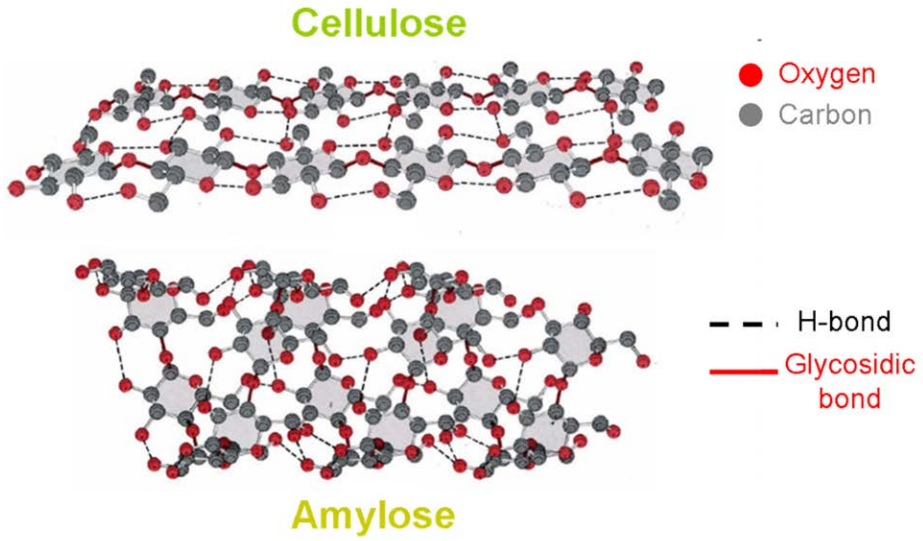


**Figure 3.2:** Cellulose and amylose structures. Adapted from Ref. [72]

*Lignin*

Even though extensive research efforts have been made to elucidate the finer structural details of the highly complex polyaromatic lignin, a definitive model does not yet exist (One of the available models is illustrated in the Appendix section Fig. A.Ch3.1 ). This task is further complicated by the wide natural variation in lignin structure, with the main difficulties arising during characterisation due to the high level of chemical and structural heterogeneity of its bonding patterns. Nonetheless, lignin polyphenolic nature has been ascertained, and the most abundant constituent monomers characterised as *p*-coumaryl, coniferyl and synapyl alcohol (Figure 3.3).[73]

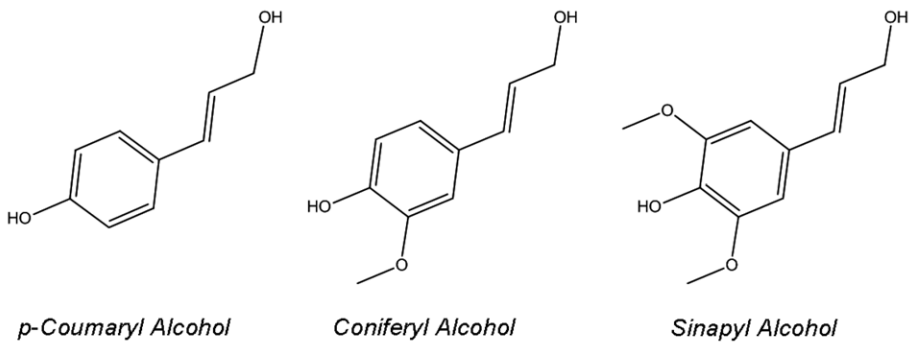


**Figure 3.3:** Major lignin building blocks

## 3.3 The effects of HTC temperature and reaction time

The morphology and chemical structure of the HTC carbons, synthesised at different temperatures and reaction times from the previously introduced precursors, have been characterised using SEM, EA and $^{13}C$ ssNMR. This latter characterisation technique in particular has been tremendously useful in highlighting the main bonding patterns differences between the HTC carbons derived from the different precursors.

### *3.3.1 Morphology analysis*

Glucose derived HTC carbons, synthesised at two different HTC temperatures (160 and 260 $^{o}$C), were analysed by SEM (Fig. 3.4). This analysis reveals the dependence of the mean particle diameter and size distribution on the processing temperature. It is evident that higher processing temperatures (i.e. 260 °C) lead to larger particles and to a more homogeneous average size, as confirmed by DLS measurements. In the case of the material prepared at 160 $^{o}$C, an average particle hydrodynamic diameter of 0.95 μm (± 75 nm) is recorded, while for the 260 $^{o}$C samples the mean value is 1.37 μm (± 60 nm). For the sample synthesised at higher temperature (i.e. 260 $^{o}$C), the mean particle size value measured by DLS and the one observed by SEM are much closer than for the HTC carbon prepared at 160 $^{o}$C. One possible explanation for this latter difference might be the wider size distribution of the 160 $^{o}$C sample and the consequential presence of very large particles, which could affect the diameter value, measured by light scattering, increasing the average error. Another factor that can possibly contribute to the value mismatch might be the presence of particles aggregates in the 160 $^{o}$C sample.

Although DLS measurements do not allow a precise estimate of the particle size for the sample processed at lower temperature (i.e. 160 $^{o}$C), they quantitatively confirm the increase in the average particle diameter at higher HTC processing temperatures, as indicated by SEM measurements. A possible explanation for the observed influence of HTC temperature on particle size might be that water properties are known to change substantially upon increasing the temperature under self-generated pressures;[74] therefore its solvating ability and reactivity / pH are highly affected over a narrow temperature range. This can play a significant role in affecting the particles' surrounding environment, which determines their colloidal stability and the coupled size features.[75, 76]

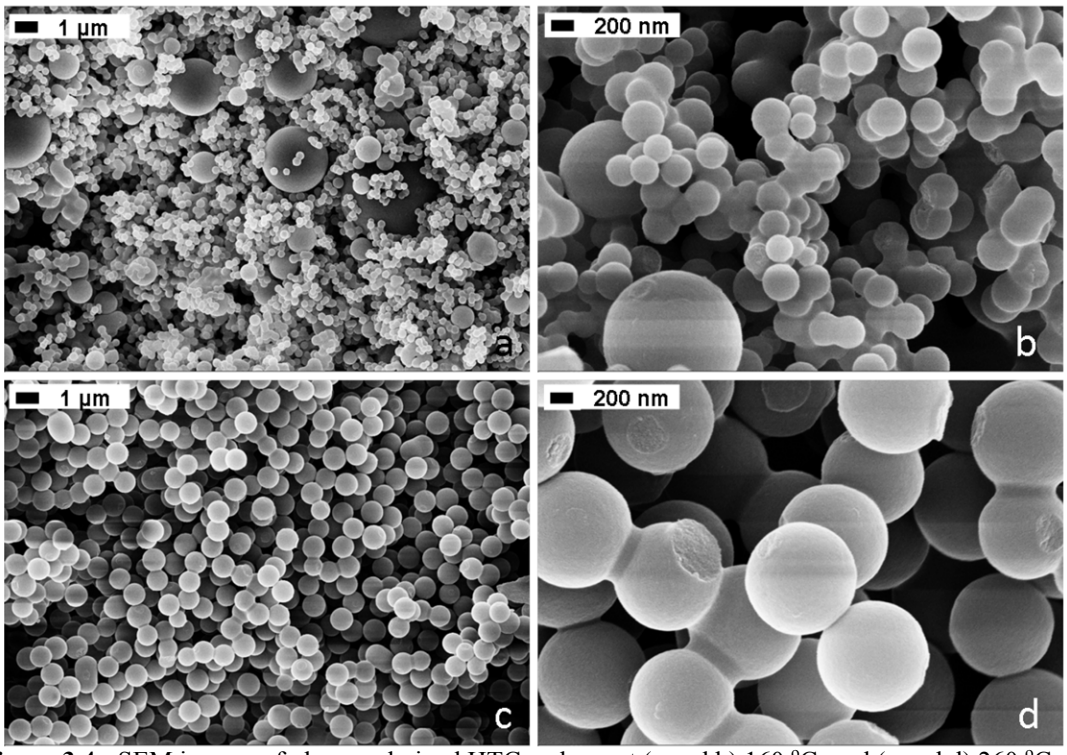


**Figure 3.4:** SEM images of glucose-derived HTC carbons at (a and b) 160 $^{o}$C; and (c and d) 260 $^{o}$C.

SEM images of the cellulose-derived HTC carbon show that at low processing temperatures, the cellulosic substrate is resistant to hydrothermal treatment (Fig 3.5 a-b). The parent fibre structure is still intact and arranged in characteristic bundles.[67] Increasing the HTC processing temperature to 220 $^{o}$C leads to the formation of spherical particles, in a similar manner to HTC materials obtained from glucose (Fig 3.5 c-d). However, the overall morphology of cellulose-derived HTC carbons is not as homogeneous as for the glucose system, as indicated by the presence of shapeless particle agglomerates presumably formed from the disruption of the cellulosic substrate.

These observations, coupled with SEM images of glucose- and cellulose-derived HTC carbon synthesised at short residence times (i.e. 6 h), highlight a remarkable difference in the mechanism of particle formation between these two carbon precursors (Fig. 3.6). In the glucose case starting from a homogeneous system, particles form via an initial nucleation step arising from formation and reaction of 5-HMF (see Chapter 2).[77] In the early stage of the reaction, they are characterised by a smaller diameter (100 - 200 nm range; Fig. 3.6a). As reaction time is increased, particle growth continues until achieving their final size, which depends upon the HTC processing temperature as previously observed. For cellulose HTC, increasing processing temperature results in an overall disruption of the fibrous network, leading

to the formation of nano \ micro-sized cellulose fragments (Fig 3.5, 3.6b). Such cellulose-derived fragments presumably still have limited solubility in water at this processing temperature,[78] and as a consequence they adopt the spherical shape to minimize their contacting interface with the surrounding.

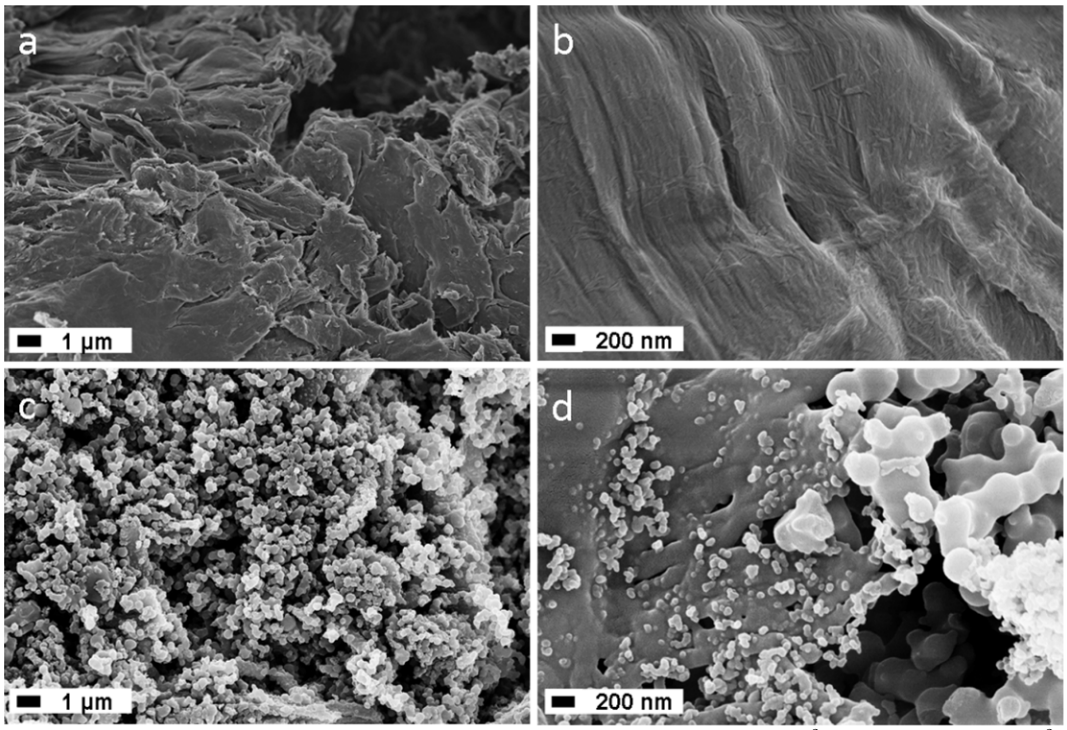


**Figure 3.5:** SEM images of cellulose-derived HTC carbons at (a and b) 160 °C; and (c and d) 220 °C.

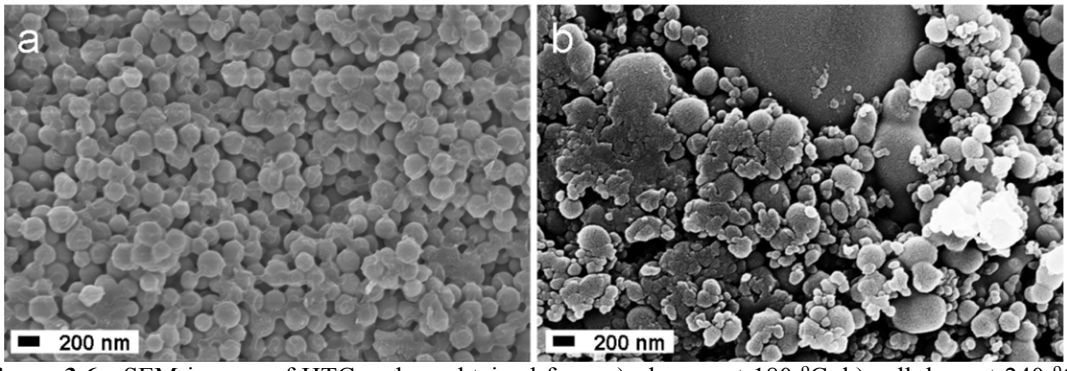


**Figure 3.6:** SEM images of HTC carbon obtained from a) glucose at 180 °C, b) cellulose at 240 °C; Reaction time = 6 h.

The morphological transformation of rye straw upon HTC treatment shows great similarities to that observed for cellulose (Fig. 3.7). Lignocellulosic biomass does not undergo any structural disruption at low (i.e. T = 180 °C) temperatures, and the rye straw fibrous structure is maintained (Fig. 3.7a-b). When this complex biomass precursor is hydrothermally treated at higher temperatures (i.e. T= 240 °C), the fibre network is disrupted, and spherical particles start forming similarly to cellulose. However, part of the natural biomass macrostructure persists even after the spherical

particles are formed on the surface of the rye straw fibres (Fig 3.7c), confirming the findings of a preliminary study employing oak leaves as carbon precursor developed by Titirici *et al.*[24]

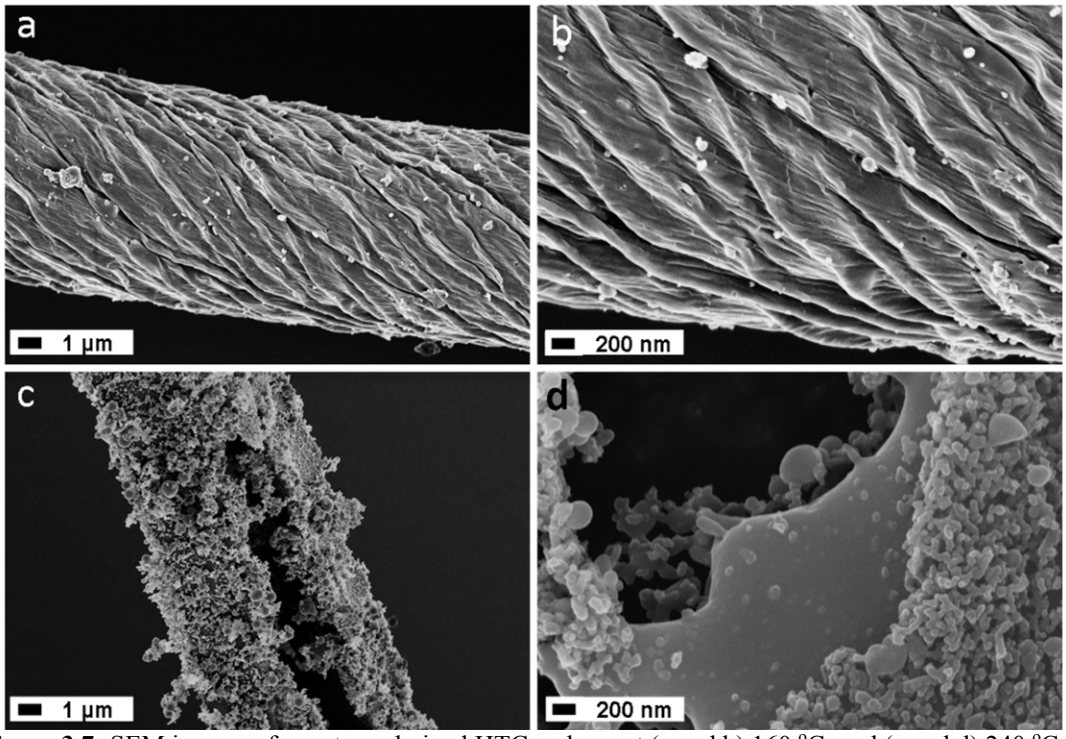


**Figure 3.7:** SEM images of rye straw derived HTC carbons at (a and b) 160 $^{o}$C; and (c and d) 240 $^{o}$C.

*3.3.2 Yield and elemental composition analysis.*

The HTC recovery yields (Fig 3.8a) of the different carbon precursors indicate the amount of solid product recovered after hydrothermal treatment as a percentage of the initial biomass weight employed in each experiment (For the equation defining the HTC recovery yield, see Appendix section, Chapter 3, Experimental procedure).

The HTC recovery yield from the model precursor glucose is not meaningful (i.e. 0%) below a lower temperature threshold (i.e. 150 – 160 $^{o}$C), as no appreciable amount of solid is formed within the studied timeframe (i.e. 24 h). On the other hand, for the other lignocellulosic raw materials (i.e. cellulose, lignin and rye straw), the HTC recovery yield gradually decreases from an initial value of 100 %, due to the increasing extents of liquefaction and gasification of the biomass at higher temperatures values, which are parallel reactions to the process of HTC carbon formation.[79, 80]

From the yield analysis of the glucose-derived HTC carbons, it is evident that the HTC process can be tuned to optimise the HTC carbon yield. The highest yield is

achieved at a processing temperature of 200 °C. Higher processing temperatures lead to lower HTC recovery yields due to larger extent of gasification reactions. As a consequence, part of the HTC carbon is lost in the form of volatile compounds.[29] However, the theoretical HTC recovery yield for glucose-derived HTC carbon is 60 wt% (grey dotted line, Fig. 3.8a). This value can be derived from the mechanism of 5-HMF formation. For each glucose molecule, converted to 5-HMF and leading to HTC carbon formation, four water molecules (i.e. 40 wt% of the starting mass) are eliminated,[58, 81] representing an unavoidable yield loss throughout the hydrothermal treatment. Furthermore the HTC recovery yields depend on the HTC processing design, higher values can be achieved in continuous operating mode or by recycling the liquid phase between two consecutive batch experiments. Such processing set-ups lead to a recovery enhancement of the unreacted liquid intermediates, which are otherwise lost in the aqueous product stream.

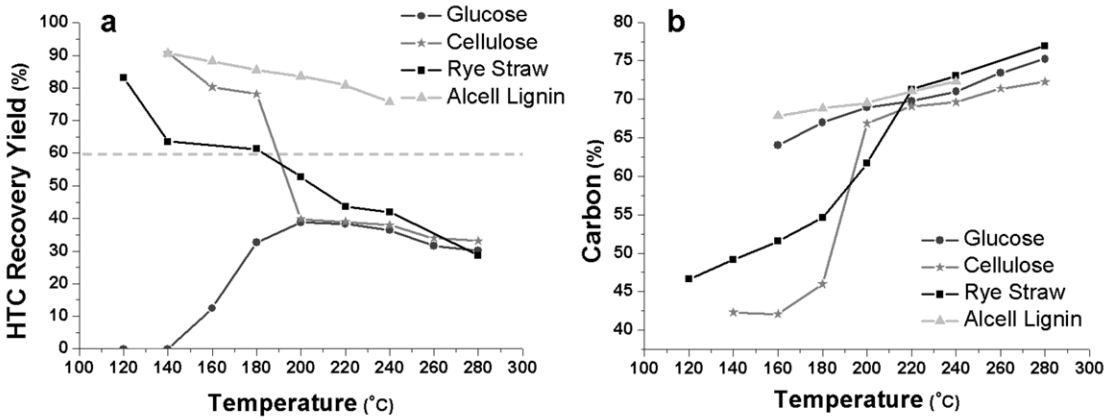


**Figure 3.8:** a) Calculated HTC carbon recovery yields and b) carbon content of HTC materials obtained from glucose, cellulose, alcell lignin and rye straw at different processing temperatures. The carbon wt% for the raw materials are respectively: Glucose = 40 %, Cellulose = 41.75 %, Alcell Lignin = 66.10 % and Rye Straw = 45.86 %.

EA demonstrates that the carbon content of glucose-derived HTC carbon undergoes a constant and gradual increase as the reaction temperature is set at higher values, suggesting a progressively larger extent of carbonisation (Fig. 3.8b). The only sharp change, corresponding to a difference of *ca.* 20 %, is observed between the carbon content of raw glucose and HTC carbon, produced at the lowest reaction temperature (i.e. 160 °C), and is caused by the dehydration of glucose to 5-HMF during the early stages of hydrothermal carbonisation.

Combining the calculated yields at different temperatures with the EA results, it is possible to investigate the mass loss upon temperature increase as a function of

chemical composition (Fig. 3.9). In the temperature range 200 - 250 $^{o}$C, the decrease of the HTC recovery yield is predominantly due to the loss of oxygen. On the other hand the carbon content (or carbon efficiency) undergoes an initial decrease presumably due to the conversion of glucose into other water-soluble degradation products (e.g. levulinic acid, dihydroxyacetone, formic acid),[80] but subsequently remains relatively constant within the range 200 – 250 $^{o}$C. Above this temperature a second steeper decrease in carbon efficiency is observed, presumably related to gasification processes leading to the loss of the thermally unstable species as volatiles.

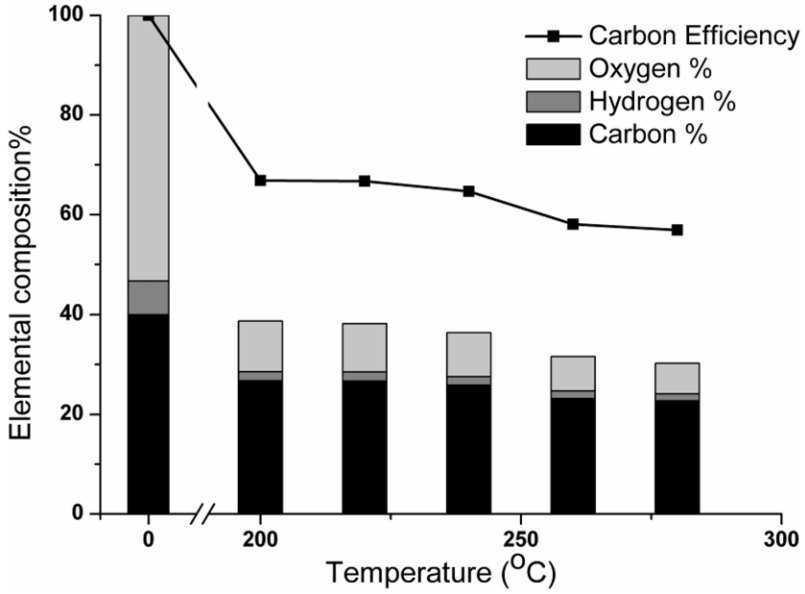


**Figure 3.9**: HTC recovery yield normalised elemental composition of HTC carbon obtained from glucose at different processing temperatures (temperature 0 corresponds to raw glucose whose HTC recovery yield is taken as 100 %) and carbon efficiency $\left(\frac{amount\_of\_carbon\_in\_the\_product}{initial\_amount\_of\_carbon}\right)$

Glucose-derived HTC carbon was also characterised using FT-IR spectroscopy in order to investigate surface functional groups evolution as a function of processing temperature (Fig. 3.10). In agreement with EA, FT-IR reveals the presence of oxygenated moieties, whose relative content drastically decreases over the processing temperature range 200 – 250 $^{o}$C. In particular the progressive disappearance of the absorption bands at 3110-3670 cm$^{-1}$ and the spectral band at 1030 cm$^{-1}$, suggest respectively the loss of hydroxyl (–OH) and ether (C-O) related functional groups as a function of increasing processing temperature. Furthermore the sharp increase and subsequent disappearance of the band at *ca.* 1700 cm$^{-1}$ indicate respectively the presence of a large fraction of carbonyl moieties in glucose-derived HTC carbon at relatively low processing temperature (i.e. 180 – 220 $^{o}$C) and their subsequent

depletion at increasingly more severe processing conditions (i.e. higher temperature), as a result of a higher extent of carbonisation and surface dehydration. The enhanced degree of aromatisation of the HTC carbons, synthesised at higher processing temperatures, is also highlighted by the increasing relative intensity of the adsorption band at 1600 $cm^{-1}$ (C=C stretching vibration) and the appearance of more defined features in the 690-820 $cm^{-1}$ region, arising from C-H out of plane bending vibrations for aromatic structures.

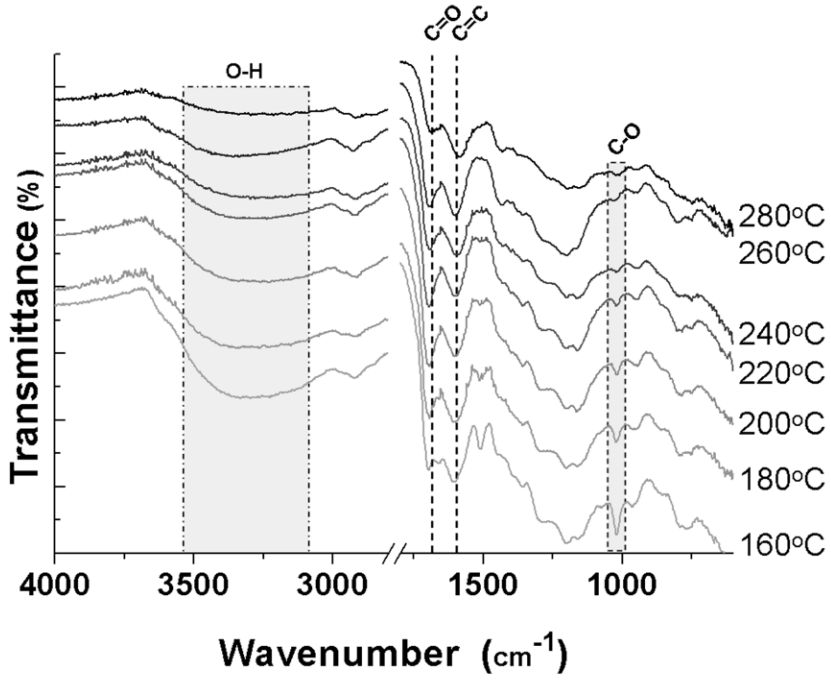


**Figure 3.10:** FTIR spectra of glucose derived HTC carbons at different temperatures.

For cellulose-derived HTC carbon, yield and elemental analysis show some differences as compared to the behaviour of glucose-derived materials (Fig. 3.8 a-b). Both the yield and carbon content can be observed to undergo negligible changes within the low processing temperature range (i.e. 140 – 180 $^{o}$C) indicating minor effects of the HTC process on the cellulosic substrate. On the other hand, within the processing temperature interval 180 - 200 $^{o}$C, a sharp transition is observed whereby yield and carbon content become respectively ca. 37% and 65%. After reaching this critical point, the slope of both curves become less steep. The presence of this sharp transition supports the idea of the existence of a well-defined temperature threshold, above which cellulose structure is disrupted as previously seen during SEM analysis. This finding is additionally supported by XRD measurements of raw and hydrothermally treated cellulose at different temperatures (Fig 3.11). Between 180 and 200 $^{o}$C, the diffraction peaks corresponding to crystalline cellulose, disappear.[82]

Above this temperature threshold, the structure of the material corresponds to amorphous carbon with no noticeable long range ordering. The presence of other crystalline peaks in the diffraction pattern was found to correspond to zinc silicate impurities ( < 1 wt% as confirmed by TGA).

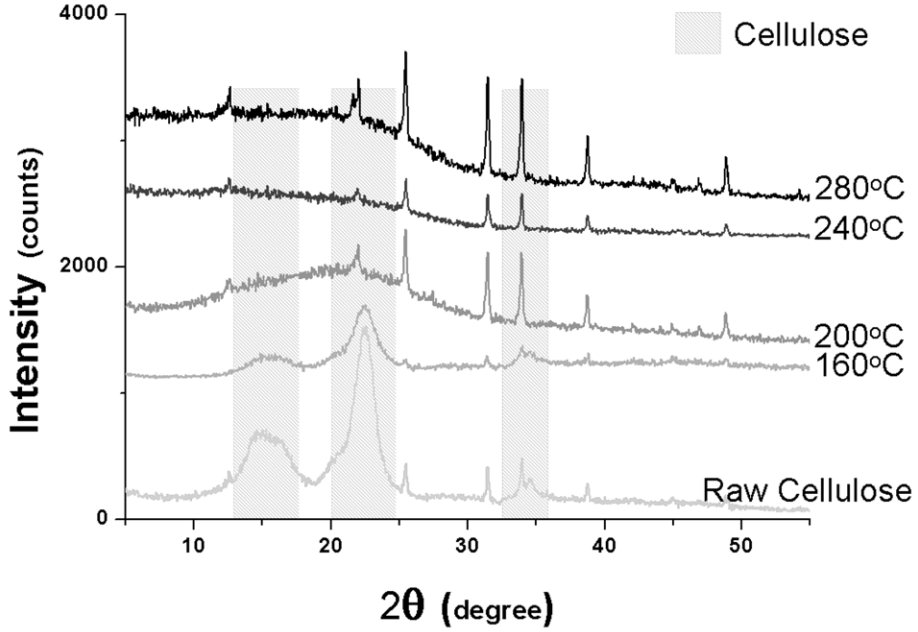


**Figure 3.11:** Powder XRD pattern of cellulose and cellulose-derived HTC carbons prepared at increasing processing temperature.

Similarly to cellulose, a sharp transition is observed for both the HTC recovery yield and the carbon content of rye straw-derived HTC carbons (Fig 3.8 a-b). However there are two main differences that need to be underlined:

**1.** Rye straw is more sensitive to hydrothermal treatment at low HTC processing temperature (e.g. 120 – 180 $^{o}$C), as indicated by the steeper changes in HTC recovery yield and carbon content. This observation is related to the presence of hemicellulose and xylose-based polysaccharides within the rye straw, which are more susceptible to hydrothermal treatment. As a consequence they are decomposed at lower temperatures, with a resultant yield loss due to formation of liquid and volatile degradation products.[83]

**2.** For rye straw, the changes in HTC recovery yield and carbon content are less steep than for cellulose in the region immediately > 180 $^{o}$C and appear to be marginally shifted to higher temperature values. Lignin, present within the lignocellulosic biomass, is presumably the cause of such differences. Due to its polyaromatic nature and high hydrophobic character, this biomass component is

affected to a very limited extent by hydrothermal treatment as indicated by its relatively constant yield and carbon content after hydrothermal treatment (Fig 3.8a-b). As a consequence, its presence may cause the HTC recovery yield of rye straw to decrease less abruptly as temperature increases. Furthermore, since lignin acts as support within the plant wall,[84] it may stabilise cellulose and prevent the disruption of its crystalline structure in the lower temperature range.

Overall yield and EA analysis highlights an interesting feature, common to all carbon precursors in the context of HTC, they all follow similar trends in terms of HTC recovery yield and carbon content for processing temperature values > 220 $^{o}$C. This finding is the first indication that above this temperature threshold, the HTC of all carbon precursors follows similar reaction patterns.

### *3.3.3 $^{13}$C solid state NMR analysis*

In order to obtain more insights on the bulk chemical structure of HTC carbons as a function of processing temperature and reaction time, the synthesised samples were also further characterised by $^{13}$C ssNMR. First glucose-derived HTC carbons at different temperatures were compared (Fig. 3.12). As previously reported in Chapter 2, the HTC carbon, synthesised at 180 $^{o}$C, is found to be majorly composed of highly cross-linked furanic-type units and characterised by a high density of oxygen containing functionalities (i.e. ketones and carbonyl groups). Increasing the HTC temperature leads to a HTC carbon with a higher degree of aromatisation, as indicated by a major decrease in the relative intensity of the peaks at $\delta$ = 150 ppm and $\delta$ = 110 - 118 ppm, respectively corresponding to carbons 2,5 and 3,4 of the furanic ring, and the simultaneous increase in relative intensity of the peak at $\delta$ = 125 - 129 ppm, ascribable to $sp^2$ aromatic carbons relating to more condensed aromatic arene-like structures. The behaviour of the resonance at $\delta$ = 208 ppm also shows the high dependence of the oxygenated functionalities content (i.e. ketones) on the processing conditions. Increasing the HTC temperature leads to the loss of such moieties and a consequential oxygen content decrease, as suggested by the progressive disappearance of the $\delta$ = 208 ppm peak. In addition, the relative intensity of resonances associated with aliphatic-type groups is fairly constant for samples prepared at T = 180, 200 and 240 $^{o}$C whilst, at higher HTC temperatures (i.e. 280 $^{o}$C), it significantly decreases indicating the loss of these less thermally stable species, which are either converted to volatile products through gasification reactions or to

increasingly more condensed $sp^2$ aromatic species. This observation is in agreement with the carbon efficiency decrease observed in the previous section during HTC of glucose at temperatures higher than 250 °C.

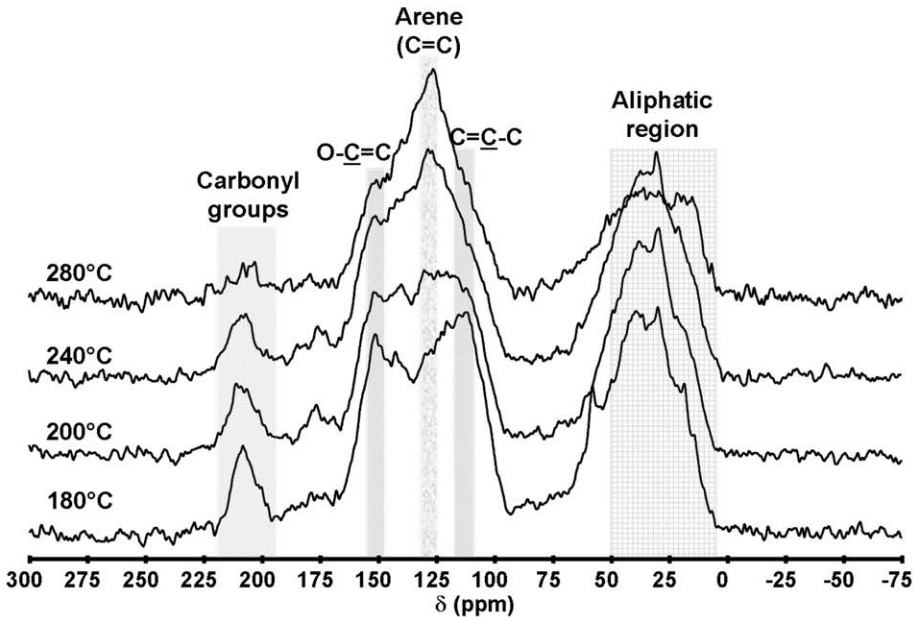


**Figure 3.12:** $^{13}C$ CP MAS NMR spectra of glucose-derived HTC carbons prepared at increasing processing temperatures.

In a second set of experiments, glucose-derived HTC carbons (T = 240 $^{o}$C) were synthesised at different reaction times and characterised by $^{13}C$ ssNMR (Fig. 3.13a). An analysis of the aromatic region (i.e. δ = 105 - 155 ppm) reveals that the central resonance at δ = 125 - 129 ppm is not visible in the early stages of the reaction (i.e. 2 h). The entire region of the spectrum is characterised predominantly by the presence of two resonances corresponding to furanic rings (i.e. δ = 150 and 110 - 118 ppm). As the HTC reaction time is increased, the relative intensity of these latter peaks diminishes, while the central resonance at δ = 125 - 129 ppm becomes increasingly more prominent. From these observations, it is evident that under more severe HTC processing conditions (i.e. HTC T > 200$^{o}$C, long reaction time) the cross-linked furanic structures, comprising the HTC carbon obtained at 180 $^{o}$C, react further via intramolecular condensation, dehydration and decarbonylation reactions to create more condensed aromatic arene-like carbon environments. This mechanistic speculation is also supported by further evidences obtained after repeating the same time experiments at lower HTC processing temperature (i.e. 180 $^{o}$C) (Fig. 3.13 b). In this case, all spectra maintain an NMR profile predominantly characterised by carbon resonances related to furanic ring structures (δ = 150 and 110 - 118ppm). This

finding, coupled to the evident lack of a predominant resonance at δ = 125 - 129 ppm, suggests that when the HTC is performed at relatively low processing temperatures (e.g. T ≤ 180°C), the initial furan rich carbon structure is maintained regardless of the reaction time.

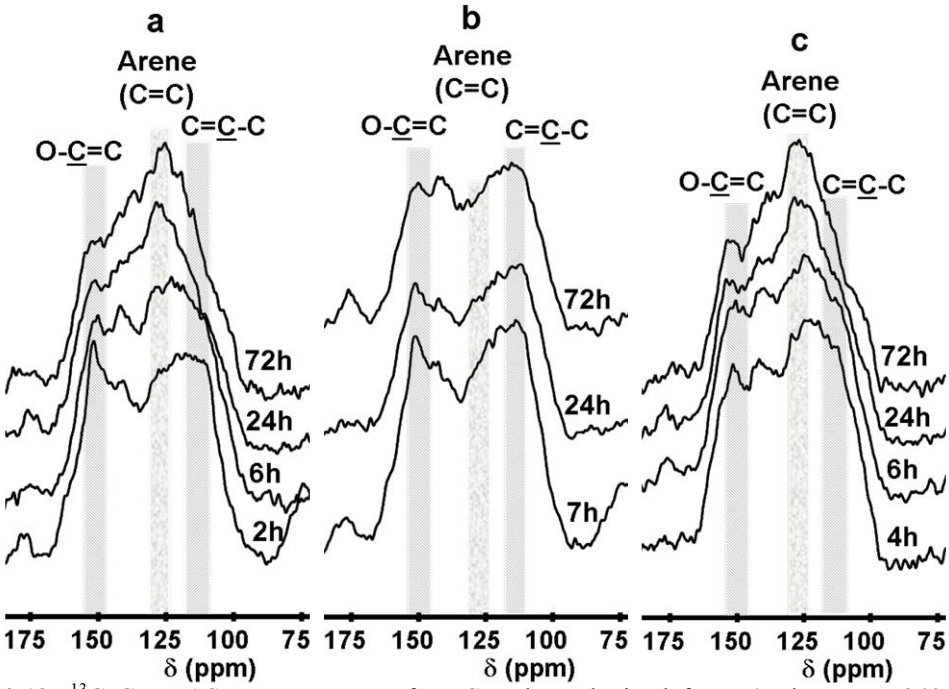


**Figure 3.13:** $^{13}C$ CP MAS NMR spectra of HTC carbon obtained from a) glucose at 240 °C, b) glucose at 180 °C and c) cellulose at 240 °C prepared at increasing reaction / HTC treatment times.

In order to highlight potential differences with glucose HTC, the same temperature dependent experiments were also repeated, using cellulose as the HTC precursor (Fig. 3.14). In accordance with the findings of the previous sections, the obtained $^{13}C$ NMR spectra demonstrate that when T = 180 °C, cellulose is still unaffected by hydrothermal treatment. The characteristic resonances (i.e. δ = 65, 72, 75, 84, 89 and 105 ppm)[85] are still present and well resolved in the NMR spectrum, while no resonances are observed in the aromatic region indicating no major HTC carbon formation. As the processing temperature is raised to 200 °C, dramatic differences are observed in the NMR spectrum. All characteristic cellulose resonances disappear, whilst a new broad resonance centred at δ = 125-129 ppm emerges. Furthermore, as observed for glucose, cellulose-derived HTC carbon shows a similar reduction in the relative intensities of resonances associated with oxygenated functional groups and an increase in the aromatic character at progressively higher temperatures, as respectively indicated by the disappearance of the peak at δ = 208 ppm and the relative increase of resonances in the region δ = 125 - 129 ppm. These

findings highlight that glucose- and cellulose-derived HTC carbons show identical peak evolution patterns for temperature values higher than 200°C, indicating the similar nature of the chemical transformations characterising the HTC of both substrates above this temperature threshold.

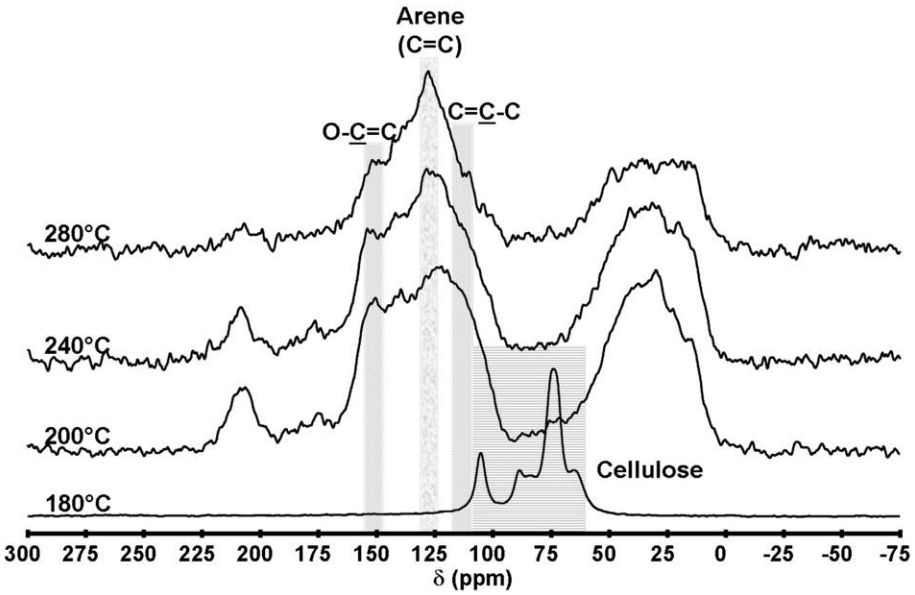


**Figure 3.14:** $^{13}C$ CP MAS NMR spectra of cellulose-derived HTC carbons prepared at increasing processing temperature.

However the $^{13}C$ NMR spectra of cellulose derived HTC carbon, synthesised at different reaction times, highlight a remarkable difference between the HTC mechanism of glucose and cellulose (Fig. 3.13c). All carbon samples obtained from cellulose are characterised by the presence of the central resonance at $\delta$ = 125 - 129 ppm. This feature is present since the early stages of the reaction contrarily to what was observed for the treatment of glucose as a function of time (Fig. 3.13 a) at the same temperature. This finding suggests that the hydrothermal carbonisation of cellulose does not proceed solely through a furanic composed intermediate (i.e. HMF), as observed in the case of the model monosaccharide (i.e. glucose). The major conversion mechanism is instead thought to be the direct transformation of the cellulosic substrate into a final carbonaceous material composed of polyaromatic arene-like networks, presumably involving reactions that are normally characteristic of the pyrolysis process. During cellulose pyrolysis, the char formation is attributed to a manifold of reactions leading to cellulose intramolecular rearrangement and formation of a cellulose-derived polymeric compound, referred to as *intermediate cellulose*. This reaction intermediate then converts to aromatic network structures at

extended reaction times.[42, 43, 86, 87] This mechanistic speculation is well supported by the similar $^{13}C$ NMR profiles of cellulose-derived HTC carbon and char obtained from lignocellulosic biomass pyrolysis.[88, 89]

In the case of rye straw-derived HTC carbons, it is evident that the spectra evolution, as a function of temperature, follows a similar pattern for cellulose except for two major differences (Fig. 3.15). First of all, resonances related to cellulose are still present in the sample synthesised at T = 200 °C. This observation is in good agreement with SEM and yield analysis, with the higher temperature-resistance of rye straw to HTC processing, attributed to the presence of lignin stabilising the cellulose fraction of the biomass. Secondly, the rye straw derived HTC carbons spectra are characterised by two additional resonances (δ = 56 and 145-148ppm) corresponding to the methoxy functional groups (-$OCH_3$) and to aromatic carbons bounded to such moieties in lignin, as indicated by $^{13}C$ CP NMR investigations of an alcell lignin sample. The near complete disappearance of such resonances in HTC carbon synthesised at T = 280 $^{o}$C, marks the loss of these functional groups at such processing conditions presumably via demethanation reactions.

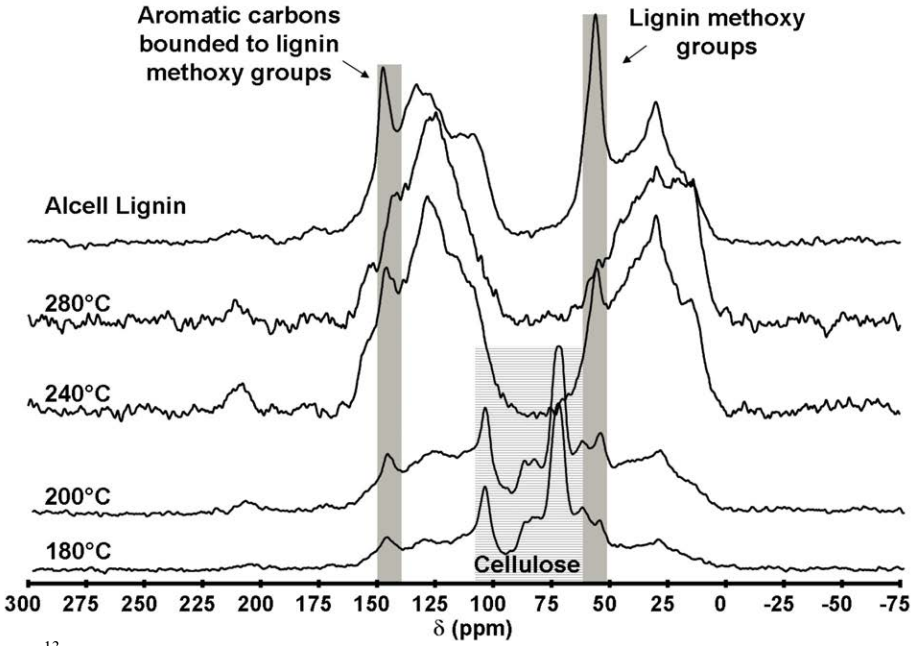


**Figure 3.15:** $^{13}C$ CP MAS NMR spectra of rye straw derived HTC carbons at different processing temperatures and a comparative spectra of alcell lignin

## 3.4 Mechanistic insights on cellulose HTC conversion.

Overall the results of the previous analysis suggest a different conversion pathway for cellulose, when HTC processing is performed under mild conditions. At T ≥ 180 $^{o}$C,

rather than the hydrolysis of the polysaccharide into glucose and its subsequent conversion into a furan rich HTC carbon, cellulose undergoes a disruption of its fibrous network leading to the formation of nano/micro sized cellulose fragments, as initially observed via SEM image analysis. These fragments adopt a spherical shape in order to minimise the contacting interface with the surrounding water and hence reduce the chances of hydrolysis of the glycosidic bond. At this point, the cellulose present in the bulk is likely to be exposed to a comparatively homogeneous thermal environment resembling the one of pyrolytic processes. Under these conditions, the cellulosic substrate undergoes intramolecular condensation, dehydration and decarbonylation reactions leading to the production of a hydrothermal carbon structurally composed of a more condensed polyaromatic arene-like carbon domains.[90] A very limited degree of hydrolysis and consequential glucose formation most likely takes simultaneously place at the envelopes interface, where cellulose is in contact with water. However this reaction route accounts only for a minor extent of cellulose conversion (Scheme 3.1).

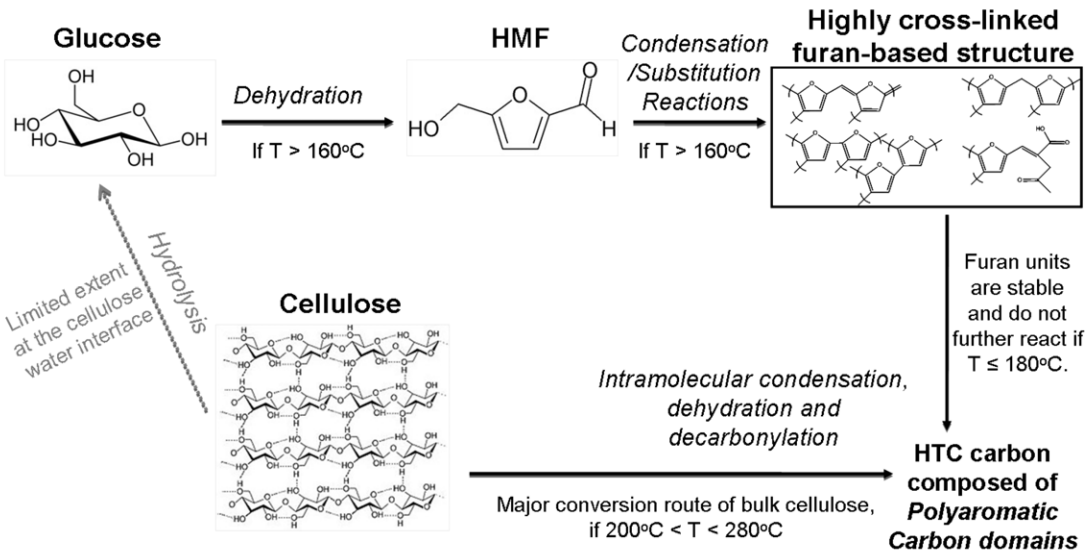


**Scheme 3.1:** Proposed model for cellulose conversion during hydrothermal treatment under mild processing conditions (180 $^{o}$C < T < 280 $^{o}$C). [*NB: Dotted lines represent minor reaction routes*].

This mechanistic scheme is well supported by the evidence that other non-reducing carbohydrates, such as starch, contrarily to cellulose, do yield furan-rich HTC carbon. In particular hydrothermal carbonisation of amylose rich starch (Hylon VII, 70% amylose) is a pertinent example, since its chemical composition is identical to cellulose. However this biopolymer is soluble in water when heated at relatively mild temperatures (60-70$^{o}$C), as previously explained (see section 3.2).

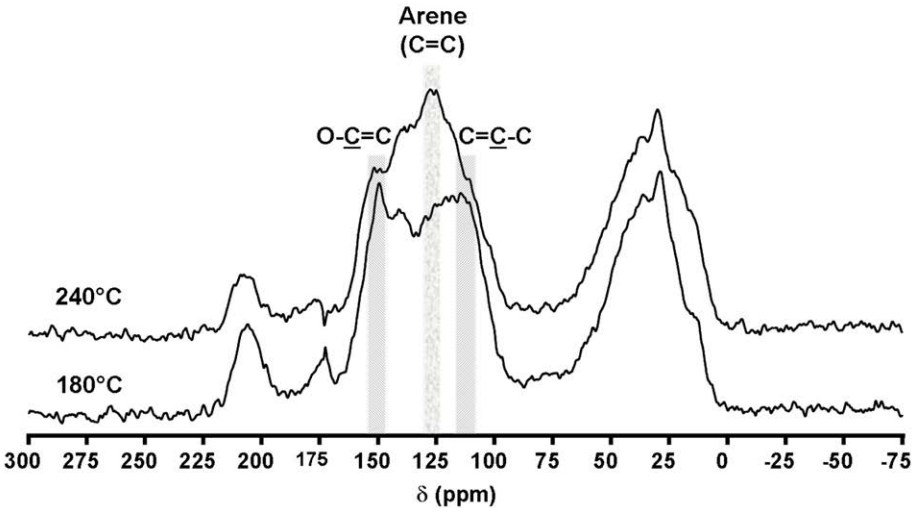


**Figure 3.16:** $^{13}C$ CP MAS NMR spectra of amylose (Hylon VII) derived HTC carbons at different processing temperatures.

Therefore amylose is more likely than cellulose to hydrolyse under mild hydrothermal treatment. This hypothesis is confirmed by $^{13}C$ NMR experimental evidences (Fig. 3.16). Resonances corresponding to furan moieties (δ = 110 - 118 ppm and δ = 151 ppm) characterise the amylose-derived HTC carbon produced at 180 $^{o}C$. On the other hand increasing the processing temperature leads to the development of resonances in the region δ = 125-129 ppm, as observed in glucose-derived HTC carbon. These findings are indicative of amylose hydrolysis into glucose and consequential HTC formation, contrarily to what observed for cellulose.

In order to enhance the extent of cellulose hydrolysis to glucose at milder temperature values (i.e. 180 $^{o}C$), HTC experiments in the presence of strong mineral acids (i.e. $H_2SO_4$) were performed (Fig. 3.17). The obtained $^{13}C$ NMR spectra show that at relatively low pH (i.e. 1) cellulose fully reacts at 180 $^{o}C$ . Nonetheless resonances corresponding to furanic moieties are not the dominant features of the NMR spectra, as it would be expected at this processing temperature value. The NMR spectrum for cellulose at *pH* = 1, shows a well-developed polyaromatic arene-like carbon resonance with a major shoulder at δ = 151 ppm, indicative of oxygenated $sp^2$ hybridised carbon environments. These features also characterise the NMR spectra of glucose-derived HTC carbon prepared at different pH. As a consequence, these results demonstrate the dependence of the chemical structure of HTC carbon upon the initial reaction mixture pH. Strong acidic solutions lead preferentially to the development of polyaromatic carbon species probably due to a higher extent of formation of furan degradation

products (e.g. levulinic acid),[91] reacting via aldol condensation and increasing the degree of conjugation of the carbon framework.[58]

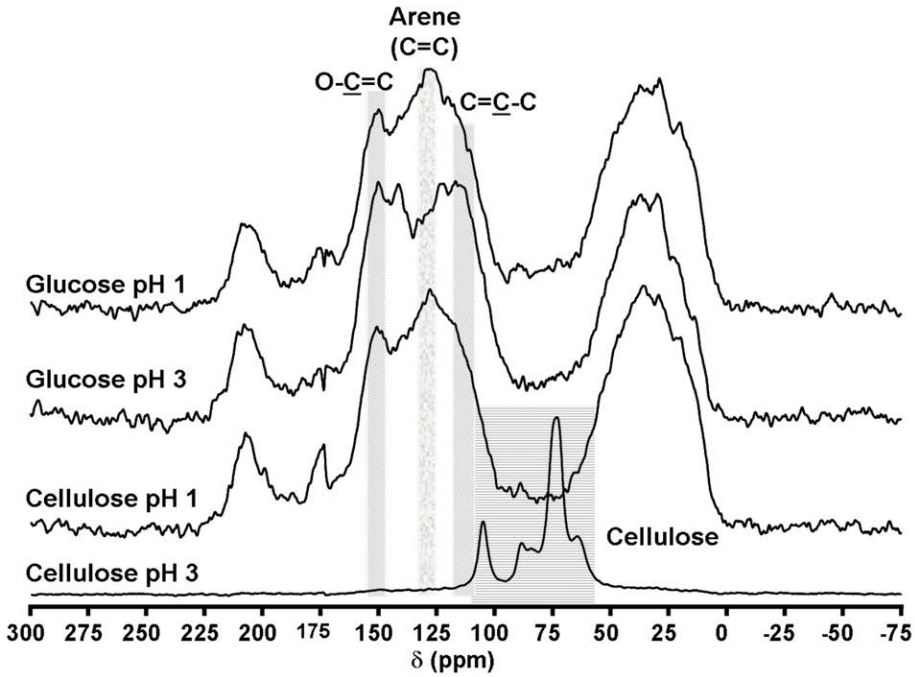


**Figure 3.17:** $^{13}C$ CP MAS NMR spectra of hydrothermal carbon obtained from glucose and cellulose at different initial *p*Hs.

The developed model also applies to lignocellulosic biomass. As previously observed, the hydrothermal carbonisation of rye straw is majorly governed by the reactivity of its cellulosic fraction, which is shifted to higher temperatures (i.e. T = 240 $^{o}$C) compared to pure cellulose (i.e. T = 200 $^{o}$C). Despite this increase, it is interesting to notice how under hydrothermal conditions the cellulose present in lignocellulosic biomass fully reacts over a lower temperature range than during pyrolysis.[89] A possible explanation for such a difference is the partial hydration of cellulose chains under HTC processing conditions, which can destabilise the hierarchical cellulosic structure and cause its disruption in this lower temperature range. The enhanced reactivity of crude biomass during HTC is further supported by the loss of lignin methoxy groups, which under hydrothermal conditions takes place between 240 – 280 $^{o}$C, while during pyrolysis it is not observed before 350 $^{o}$C.[92]

## 3.5 Summary

In this chapter a detailed investigation on the HTC conversion mechanism of lignocellulosic biomass (i.e. rye straw) and its single components has been presented (i.e. cellulose). The main differences between HTC carbons derived from cellulose and glucose have been analysed, based on the effects of HTC temperature and reaction time on the morphology and chemical structure of the synthesised samples. In the latter case, it was observed that HTC temperature is a powerful tool that allows tuning the chemical structure of the synthesised material. At relatively low temperatures (i.e. 180 $^{o}$C) glucose-derived HTC carbon was majorly composed of highly cross-linked furan units, as seen in the previous chapter. However increasing the HTC temperature led to the formation of condensed polyaromatic carbon domains possessing an increasingly hydrophobic character. In the case of cellulose-derived HTC carbon, the furan rich structure could not be isolated at any of the investigated processing conditions. The chemical structure of the synthesised samples was always characterised by a prevalent polyaromatic nature, as suggested by $^{13}$C ssNMR experiments. These evidences were indicative of a different HTC conversion mechanism for cellulose, involving reactions that are commonly observed during pyrolytic processes. The low water solubility of cellulose was identified as the cause of such difference, since it hindered the hydrolysis of the glycosidic bond and resultant formation of glucose. This mechanistic speculation was supported by the evidence that amylose, a glucose polymer soluble in water at relatively low temperature (i.e. 60-70 $^{o}$C), did produce furan rich HTC carbon.

These reactivity patterns observed for cellulose were also reflected in the rye straw-derived HTC carbon, indicating the main role of the cellulose fraction during the HTC processing of lignocellulosic biomass. Furthermore, in the case of rye straw, the cellulose conversion to HTC carbon was observed to shift to a higher temperature range (i.e. 220 - 240 $^{o}$C) presumably due to the presence of lignin hindering its disruption. However, its full conversion into a final carbonaceous material still took place in a lower temperature range than during pyrolysis (ca. 350$^{o}$C) providing potential advantages from an energetic point of view.

# CHAPTER 4 – Chemical structure differences between HTC and pyrolysed carbons

## 4.1 Introduction

In the field of functional carbon material synthesis, pyrolysis is a frequently adopted post-treatment step since it allows tuning several features of the synthesised materials including carbon content and surface functionality, as well as mechanical, electronic and structural properties.[22] Understanding the effects of pyrolysis on the HTC carbon structure would certainly be advantageous, since this further processing step would facilitate a higher degree of control over material properties, which could then be specifically tailored according to the end-application. A relevant example is the chromatographic separation of analytes, where the effectiveness of a stationary phase is majorly dependent upon its surface polarity. This property could be easily tuned by adopting different carbonisation temperatures during the pyrolysis of HTC carbons, as shown for other materials.[93]

Furthermore, investigating the thermal decomposition behaviour of HTC carbons and comparing HTC carbons before and after pyrolysis would also provide further useful insights regarding chemical structure and mechanistic discussion. In addition the comparison with biomass derived chars, obtained from direct pyrolysis, would help placing HTC within the context of thermo-chemical processing techniques. The following chapter presents a detailed investigation on the pyrolysis of glucose derived HTC carbons. Carbon materials obtained from direct pyrolysis and HTC are also compared based on a semi-quantitative NMR analysis, aimed at estimating the relative ratio of furan to arene-like species as a function of processing conditions.

## 4.2 Pyrolysis of carbon material precursors.

Pyrolysis (or carbonisation) of organic or carbonaceous precursors is the most common synthetic route for the production of carbon materials. During this process the substrates undergo physicochemical changes, which may eventually lead to the formation of hexagonal graphite, the most thermodynamically stable carbon allotrope.[94] The conversion of the starting precursors into a product with progressively higher carbon content has several intermediate stages, determined by the carbon precursor choice and the applied treatment temperature.[95] As a general premise, the substrate initially undergoes thermal decomposition, leading to the

elimination of heteroatoms in the form of volatile species (e.g. $CO_2$, CO, $CH_4$, $H_2O$). Simultaneously the forming carbon network rearranges *via* successive condensation/dehydration reactions, resulting in an increased degree of aromatisation (i.e. formation of polyaromatic arene-like species). It is emphasised in the literature how at this stage, the carbon material is not composed of a continuous solid phase. On the other hand, a relatively high amount of microporosity is usually encountered in pyrolytic carbons, generally attributed to voids present between the pre-graphenic aromatic structures comprising the carbon material at this stage.

At higher processing temperatures (> 800 $^{o}$C), microporosity disappears due to the increased ordering of the carbon structure and the formation of crosslinks between the aromatic intermediates (i.e. charring step). Depending on the relative extent of these two processes, carbon precursors have been divided into graphitisable and non-graphitisable by Franklin *et al* in 1950 (Fig 4.1).[96] The latter carbon type is characterised by a high degree of crosslinking and long range isotropy. In the former case, the aromatic sub-units have a higher tendency to align parallel to each other and therefore give rise to a pre-graphitic structure.[97] This alignment process takes place through a fluid intermediate, which is referred to as a liquid nematic phase.[98, 99]

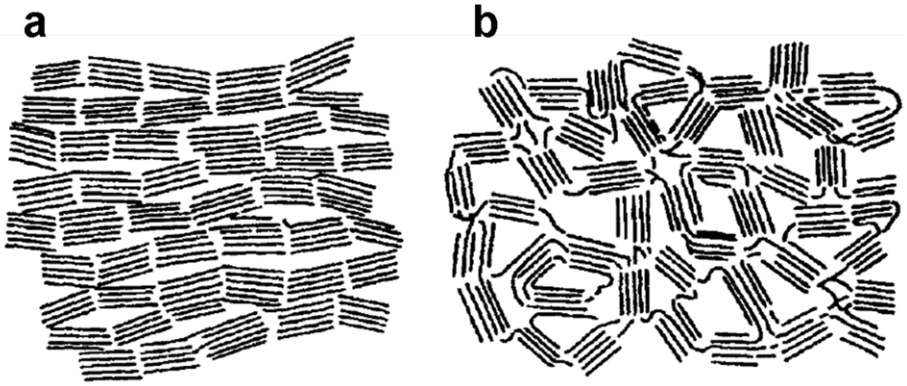


**Figure 4.1:** a) Graphitisable and b) Non-graphitisable carbon structure as described for the first time by Franklin *et al*. Reproduced from [96].

The tendency of non-graphitisable carbons to give rise to isotropic and entangled carbon structures is attributed to the relatively large fraction of highly curved pre-graphenic layers, arising from the presence of non-six carbon member rings within the carbon framework.[100] Their formation is largely dependent upon the nature of the carbon precursor.[101]

## 4.3 The effects of pyrolysis on glucose derived HTC carbons

As described in the previous section, the carbonisation of carbonaceous precursors is composed of several stages (i.e. thermal decomposition, charring, graphitisation). The following section predominantly focuses on the pyrolysis in the lower temperature range (< 800 $^{o}$C) of glucose-derived HTC carbons. First, the effects on the chemical structure of HTC carbon are investigated by combining both bulk (i.e. EA and $^{13}$C ssNMR) and surface (i.e. XPS) characterisation techniques. The thermal decomposition behaviour and the development of material porosity during pyrolysis of HTC carbons are also studied by means of TG-IR, $N_2$ sorption and HR-TEM.

### *4.3.1 Effects on the bulk and surface chemical structure*

EA of the hydrothermal carbons pyrolysed at different temperatures (Table 4.1) reveals major compositional changes in the temperature interval 350 -550 $^{o}$C, where the C content increases to approximately 85% while the H and O contents are markedly reduced. Increasing pyrolysis temperature to 750 $^{o}$C has a similar effect on the HTC carbon elemental composition, although this time the rate of change of the carbon content with temperature is less steep. These findings suggest that 350 - 550 $^{o}$C interval is the critical temperature region for HTC carbon thermal decomposition. Presumably at temperatures > 550 $^{o}$C, the occurring carbonisation can be described as a charring process.

**Table 4.1:** Elemental analysis of HTC carbons obtained from glucose at 180$^{o}$C and then pyrolysed (Δ) at 350 $^{o}$C, 550 $^{o}$C and 750 $^{o}$C respectively.

| Sample | C% | H% | O% |
|---|---|---|---|
| **HTC** | 64.47 | 4.69 | 30.84 |
| **HTC-Δ350** | 66.95 | 4.03 | 29.02 |
| **HTC-Δ550** | 84.66 | 2.83 | 12.51 |
| **HTC-Δ750** | 94.04 | 1.67 | 4.29 |

Although EA does not show major differences between HTC and HTC-Δ350$^{o}$C, the aromatic regions (δ = 105-155 ppm) of these carbons do differ significantly from each other, as observed via $^{13}$C ssNMR analysis (Fig. 4.2). HTC-Δ350$^{o}$C presents an enhanced level of aromatisation, demonstrated by an increased intensity of the central resonance at δ =125-129 ppm and partial loss of the furanic shoulder at δ = 110 - 118 ppm, as compared to the parent HTC material. Likewise, and in agreement with EA results, increasing the pyrolysis temperature from 350 to 550 $^{o}$C results in the disappearance of furanic associated resonances, as polyaromatic arene-like species

become the most dominant structural motif. Increasing the temperature further to 750 $^{o}$C leads to enhanced aromatisation of the HTC carbon, as indicated by the drifting of the central aromatic resonance to a lower chemical shift (δ = 125 ppm) and by the broadening of its profile. Both features are indicative of an extended delocalized π-system and of a reduced mobility of the carbon species.[102] As may be anticipated, increasing the pyrolysis temperature over this range (i.e. 350 – 750 $^{o}$C) also leads to the loss of the thermally unstable aliphatic groups, as observed from the progressive disappearance of resonances in the δ = 10-60 ppm region (Fig. 4.2).

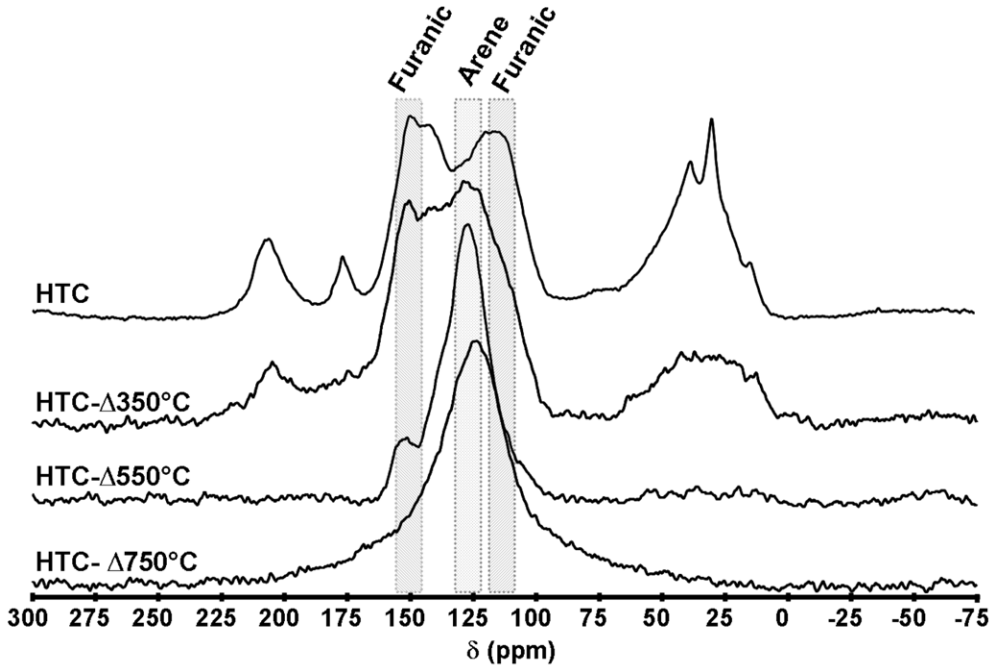


**Figure 4.2:** $^{13}$C single pulse MAS NMR spectra of HTC carbons obtained from glucose at 180$^{o}$C and then pyrolysed (Δ) at 350 $^{o}$C, 550 $^{o}$C and 750 $^{o}$C.

This $^{13}$C NMR analysis of pyrolysed HTC samples emphasises how examination of the aromatic resonances provides a very useful analytical handle on the development of the carbon structure as a function of pyrolysis temperature. To provide more details on such structures, 2D DQ-SQ $^{13}$C NMR experiments were designed to investigate these structural changes. As shown in Chapter 2, this ssNMR technique provides a greater degree of information regarding molecular connectivity of the different species within the carbon chemical structure.

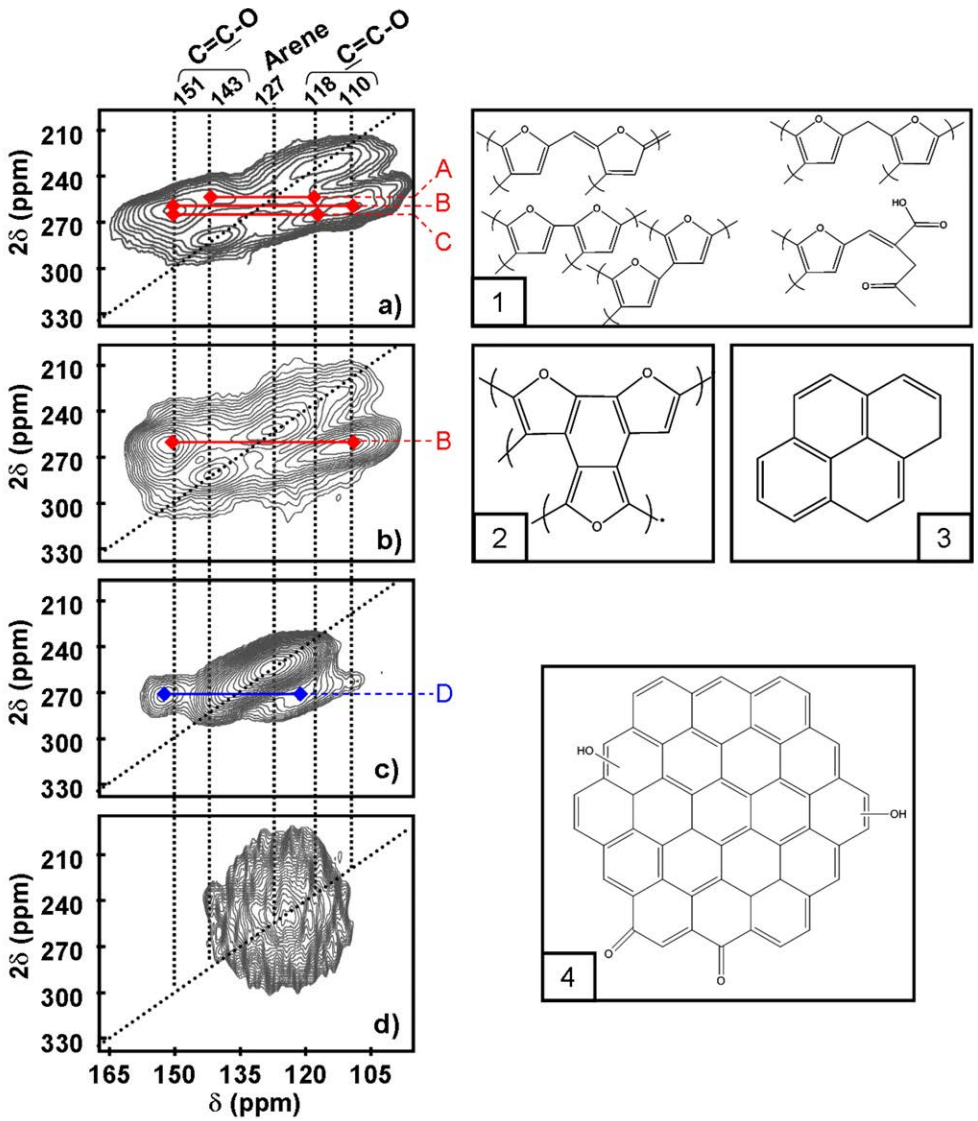


**Figure 4.3:** Aromatic region (δ = 100 – 160 ppm) of the $^{13}C$ spectra obtained with $^{13}C$-$^{13}C$ DQ-SQ experiments (CP filtered) performed on HTC carbons obtained from a) glucose at 180 °C and then pyrolysed (Δ) at b) 350 °C, c) 550 °C and d) 750 °C. [NB: 1, 2, 3 and 4 are representative chemical structures].

As initial point of examination, a 2D spectrum of the aromatic region of glucose-derived HTC carbon (prepared at 180 °C) was obtained (Fig 4.3 a). As explained in chapter 2, the *on* (δ =110, 118 and 143 ppm) and *off* (A, B and C) diagonal cross peaks are characteristic of a carbon framework mostly composed of highly cross-linked furan moieties (Fig. 4.3.1). Upon first inspection, pyrolysis of the HTC carbon at 350 °C does not result in major modifications of the 2D aromatic spectrum (Fig 4.3 b). However the persistence of crosspeak **B** is noteworthy and strongly supports the evidence that furan units are still present within the carbon framework at this pyrolysis temperature. At the same time the near complete disappearance of the *on*

and *off* diagonal crosspeaks (A and C), related to the resonance at δ = 118 ppm, suggests that the bonding patterns involving the cross-linked 3 and 4 furan carbons have changed. The coupled increased intensity of the *on* diagonal δ = 127 ppm crosspeak implies that such carbons are now part of a more extended, conjugated aromatic structure, resulting in the observed peak shifts. Such structures (a reference example model is given in Fig 4.3.2) may arise due to condensation reactions, leading to the formation of a more cross-linked and thermally stable aromatic network. Similar trends have been observed during the pyrolysis of polyfurfuryl alcohol (PFA) derived furan-rich resins.[103, 104]

The strong relative intensity of the δ = 127 ppm *on*-diagonal crosspeak cannot be solely justified by the presence of such structural motifs (Fig. 4.3.2.) Further peak deconvolution / refinement and assignment of the aromatic region highlights the multi-component nature of the resonance at δ = 127 ppm, which is found to be the sum of two distinct contributions at δ = 131 and δ = 125 ppm (Fig. 4.4a). Additional CP experiments at variable contact times (i.e. $t_{CP}$) indicate the protonated nature of the δ = 125 ppm component, since its intensity rapidly increases upon CP (Fig. 4.4b). All these results are indicative of the presence of both protonated and non-protonated $sp^2$ aromatic carbons within the material structure. Therefore, based on these evidences, it is not possible to exclude the presence of small arene-like aromatic structures in the HTC carbon scaffold prepared at 350 °C (Fig 4.2.3).

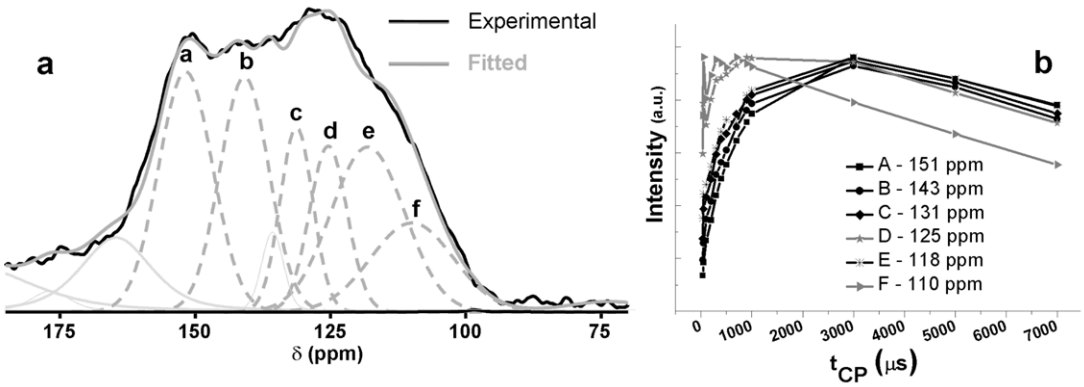


**Figure 4.4:** a) Peak deconvolution and assignment of the aromatic region for the HTC sample pyrolysed at 350°C. b) Contact time ($t_{CP}$) dependence of the peak intensity according to the deconvolution shown in a.

The complete loss of the furanic-based network only occurs after pyrolysis at 550 °C, as confirmed by the loss of the crosspeak **B** (Fig. 4.3c). Conversely, the aromatic region of the 2D spectrum is now characterised by a stronger cross peak at δ = 127

ppm, representative of a very well developed polyaromatic arene-like scaffold. The additional crosspeak **D** is instead attributed to phenolic carbons close to quaternary and protonated $sp^2$ carbons. These experimental results are verified by comparison with literature studies on the pyrolysis / thermal treatment of PFA-derived furan-rich resins. Furan ring opening is expected between 300 and 500 $^oC$, resulting in oxygen elimination,[105-107] whilst polyaromatic arene-like domains are spontaneously formed from the furan units fragments.[108] Therefore the total disappearance of the furanic-related cross peaks in the pyrolysis temperature range 350 - 550 $^oC$ and the dramatic intensity increase of the $\delta$ = 127 ppm on diagonal cross peak are presumably the result of such thermal decomposition processes.

The disappearance of the crosspeak **D,** together with the drifting of the $\delta$ = 127 ppm crosspeak to a lower chemical shift value ($\delta$ = 125 ppm), suggests that a further increase of the pyrolysis temperature to 750 $^oC$ leads to additional aromatisation of the carbon framework and loss of the hydroxyl groups belonging to the phenolic moieties. As a result , the material is at this stage composed of extended aromatic domains (Fig 4.3.4). However EA of HTC-Δ750 suggests that the presence of residual oxygenated functionality, presumably at the polyaromatic domain edges, cannot be totally discarded (Table 4.1; Fig 4.3.4). These moieties are not detectable and therefore not visible in the 2D spectra, because of their low relative abundance.

In order to investigate the effects of pyrolysis on the surface chemical structure of HTC carbons, three different glucose derived samples (as synthesised at 180$^oC$ and post-pyrolised at 550 and 900 $^oC$) were analysed by XPS (Fig 4.5). The high resolution C1(s) envelope of glucose derived HTC carbon is characterised by three main contributions, at 285.0 eV (C-C and C-$H_x$), 286.3 eV (C-O-H (hydroxyl), C-O-C (ether)) and 287.9 eV (C=O (carbonyl) ) with a minor shoulder at 289.3 eV (O=C-O (acid or ester)) (Fig 4.5a).[109] The relatively high intensity of the peaks at 286.3 and 287.9 eV indicates the presence of a considerable amount of oxygenated functionalities, mostly related to the furan and carbonyl moieties present in the HTC carbon structure. Pyrolysis at 550 $^oC$ causes a major reduction of the oxygen related contributions, indicating the loss of such functionalities and a resultant increase of surface hydrophobicity (Fig 4.5b). The residual intensity of the peak at 286.4 eV can be attributed to the presence of phenols group forming during the pyrolysis process, as confirmed by $^{13}C$ ssNMR. Increasing the temperature to 900 $^oC$ leads to a further loss of oxygenated functional groups, present at this stage only in minor quantities, as

indicated by the XPS survey scan (ca. 2.9%, see appendix section Fig. A.Ch4.1). In addition the simultaneous increase of the peak at 291.1 eV, corresponding to $\pi \rightarrow \pi^*$ shake up satellites, suggests the presence of extended pre-graphenic polyaromatic domains as the major building unit of the carbon scaffold.

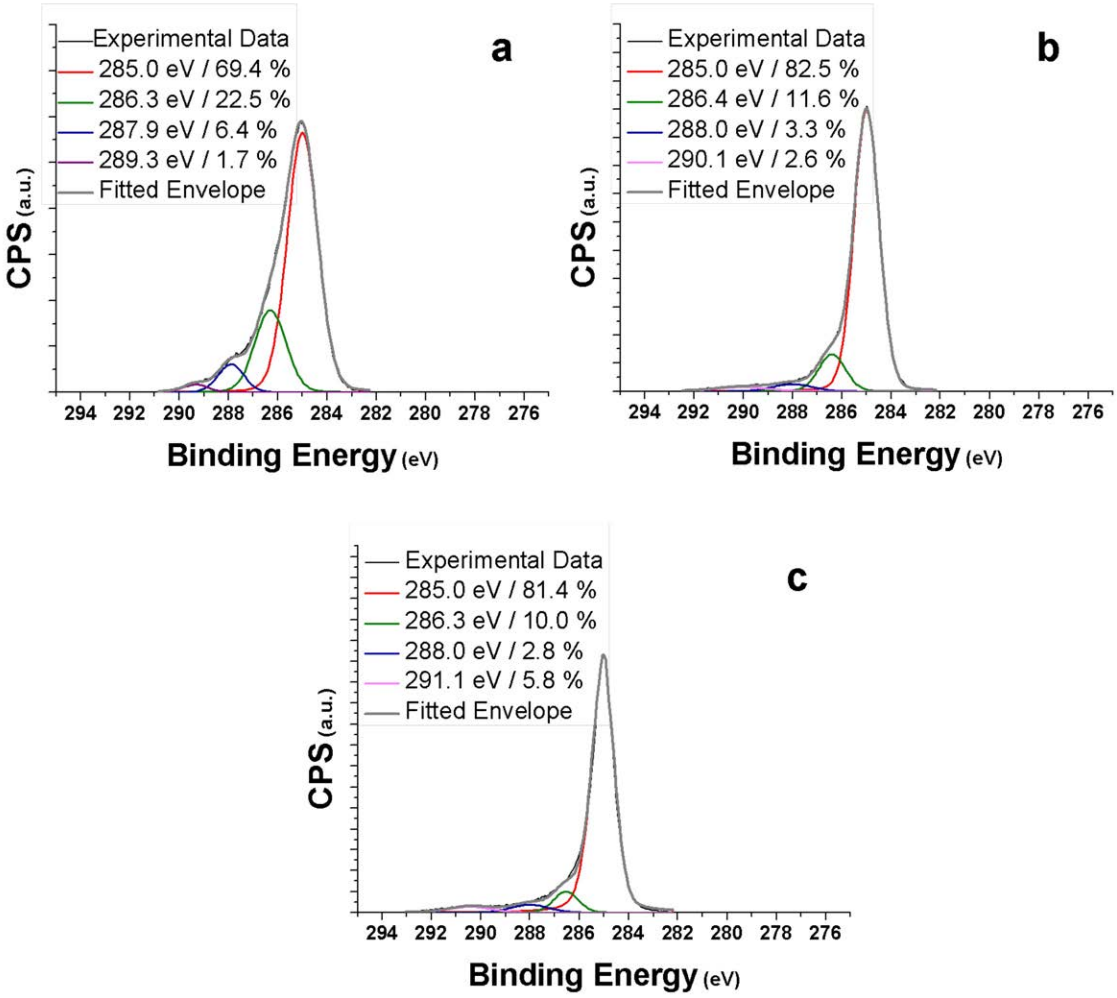


**Figure 4.5:** C1(s) photoelectron envelope of a) glucose derived HTC carbon at 180 °C and post-pyrolised at b) 550 °C and c) 900 °C

### *4.3.2 Thermal decomposition behaviour and porosity evolution.*

During glucose HTC, degradation products (e.g. levulinic acid) are formed and generally adsorbed onto the surface of the synthesised carbons. Simple washing with water and ethanol may not be sufficient for the complete removal of such products. The subsequent and potential release of these compounds may lead to undesired structural changes (e.g. porosity development) or negative performance for specific applications (e.g. analyte contamination when using HTC carbon as a stationary phase in chromatography). In order to ascertain the possible presence of entrapped

molecules within the structure of HTC carbon synthesised at 180 °C, a comparative analysis between a post-synthesis washed sample and a Soxhlet extracted one (with ethanol, hexane and THF), is presented in the following section.

TGA-IR was used to analyse the thermal decomposition behaviour of both samples (Fig. 4.6 and 4.8). The thermal decomposition of the non-extracted HTC carbon is composed of two relative broad decomposition events (160 – 270 °C and 350 – 600 °C; Fig 4.6a), whilst in the case of the extracted sample, only one main event between 350 and 600 °C is observable (Fig 4.6b). [*NB: The first peak between 100 - 180 °C for the extracted sample is ignored, as it is attributed to removal of residual extraction solvent and physisorbed water*].

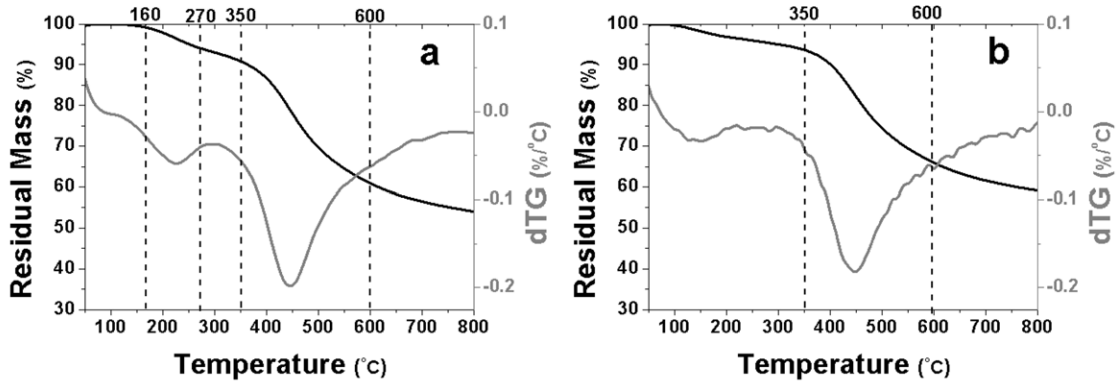


**Figure 4.6:** Thermogravimetric analysis of glucose derived HTC carbon at 180°C a) before extraction and b) after three consecutive extractions with ethanol, hexane and THF.

The first event (160-270°C) of the non-extracted sample is attributed to the thermal evolution of levulinic acid, embedded within the highly cross-linked HTC structure. Several evidences support this observation. First of all the decomposition peak appears across the levulinic acid boiling point range (i.e. 245-246°C).[110] At the same time GC-MS analysis of the extracted ethanol fraction demonstrates the presence of levulinic acid confirming its removal upon Soxhlet extraction (Fig. 4.7a-b). This finding explains the absence of the 160 - 270 °C dTG peak in the TGA curve of the extracted sample.

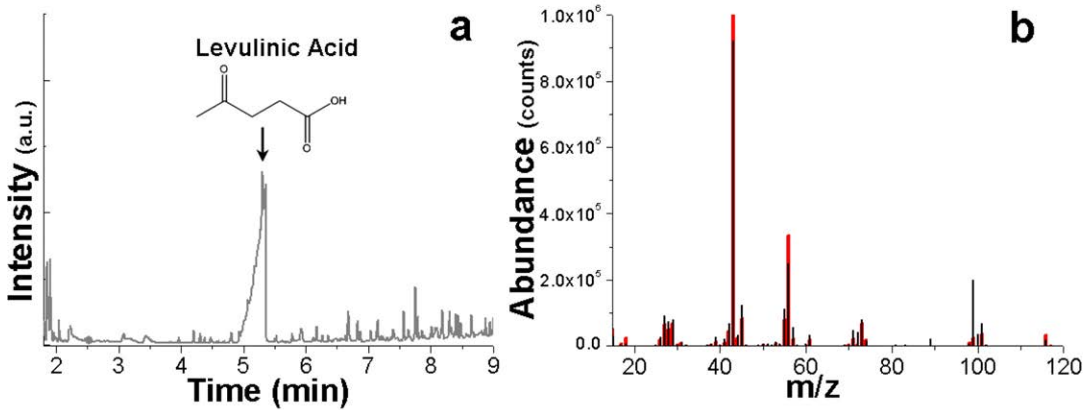


**Figure 4.7:** a) Gas chromatograph of the extract obtained after Soxhlet extraction with ethanol of glucose derived HTC carbon at 180°C. b) Mass Spectrum of the peak indicated in (a) (red – literature data,[111] black – experimental data).

Furthermore gas phase IR analysis of the evolved species, during the thermal degradation of HTC carbon, indicates that over the temperature range 160 - 270 °C the detected peaks are all ascribable to levulinic acid (Fig 4.8a). (For a comparison of full IR spectrum of the volatiles with gaseous levulinic acid, see appendix section Fig. A.Ch4.2). In particular, extract gas phase IR traces at 1770 and 1740 $cm^{-1}$ correspond to the carbonyl stretching of ketones and carboxylic acids. Such traces are not detected during the thermal decomposition of the extracted sample.

The decomposition event over the range 350 – 600 °C is observed for both samples. This evidence indicates a restructuring of the carbon motifs with simultaneous loss of volatile species, as supported by the corresponding IR analysis of the evolved gases (Fig. 4.8). Starting at 400 °C, the traces with the strongest intensities correspond to $CO_2$ and CO. Subsequently at ~ 450 °C, methane evolution is detected and the intensity of its corresponding peak increases until 550 °C. Above this temperature threshold all the detected signals fade away at different rates.

The observed cascade of instability upon pyrolysis of HTC carbon is in good agreement with the $^{13}C$ NMR experiments, as well as with literature studies on the pyrolysis of PFA-derived resins.[112] Furan ring opening is expected to take place within the temperature range where the second event of the TGA curves is observed. The evolution of CO and $CO_2$ can be attributed to the successive oxygen elimination from the furan fragments, whilst the methane trace is most likely related to the removal of methylene bridges acting as cross-linkers within the HTC carbon framework.[113] This analysis is indicative of the progressive conversion of furan moieties into polyaromatic arene-like domains.

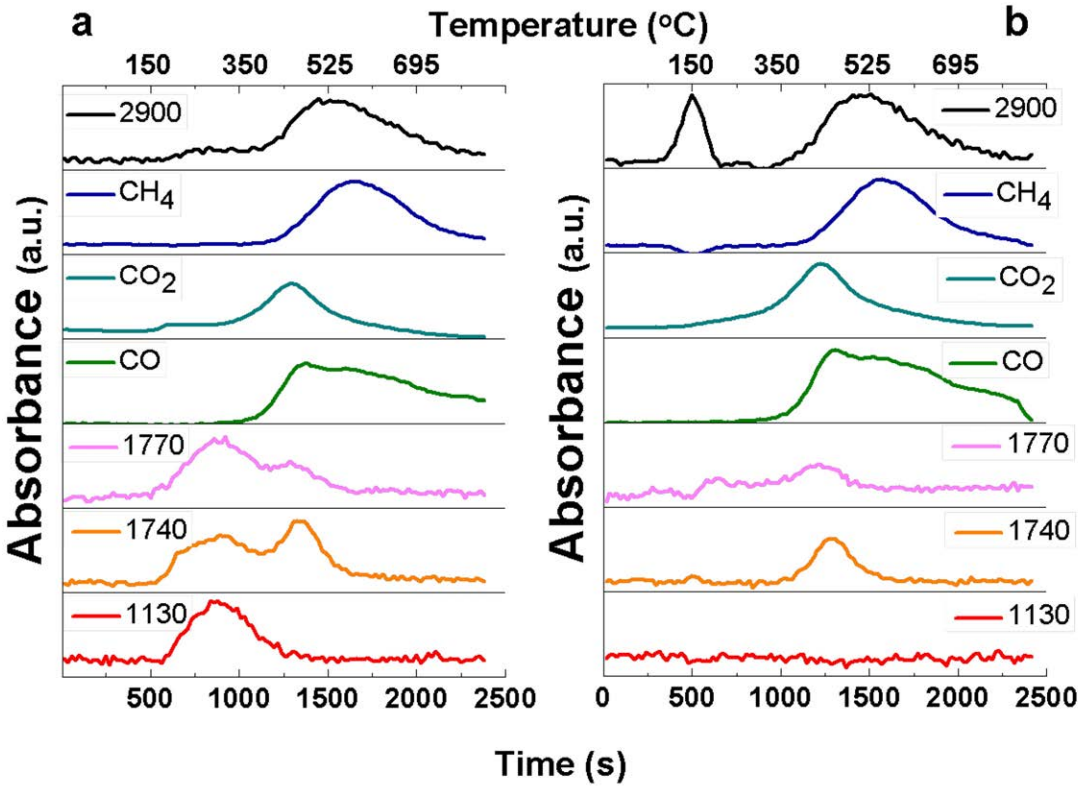


**Figure 4.8:** Extracted traces from TG-IR analysis at selected wavenumbers ($cm^{-1}$) for a) HTC synthesised at 180°C and b) HTC synthesised at 180°C after extraction with EtOH, hexane and THF. The legend shows either the name of the evolved gas, the trace can be attributed to, or the wavenumber ($cm^{-1}$), the trace is detected at.

To investigate the development of porosity in glucose-derived HTC carbons, after either Soxhlet extraction or further pyrolysis at 600 °C, $N_2$ sorption was employed (Fig. 4.9). The pyrolysed HTC carbon was processed at 600 °C, since at this temperature the main decomposition events have already occurred, as previously seen with TGA analysis. $N_2$ sorption isotherms of the HTC carbon (synthesised at 180°C) and extracted HTC carbon show negligible gas uptake indicating the absence of any developed internal porosity (Fig. 4.9a). This is rather surprising for the latter sample, since the removal of the levulinic acid upon extraction could be expected to create voids within the HTC carbon structure. A possible explanation might be that the HTC carbon, synthesised at 180 °C, possesses still a relatively "soft" or polymeric structure. It is well known from material science templating strategies that porosity (microporosity in particular) can be introduced within an organic polymeric structure only if the overall scaffold has a high enough degree of rigidity to counterbalance the polymer chains tendency to pack closely together, once the template is removed.[114] This structural rigidity does not characterise HTC carbons, as a consequence upon

levulinic acid removal the polymeric carbon scaffold presumably collapses closing the pores down.

A type I isotherm characterises the $N_2$ uptake of the HTC carbon pyrolysed at 600 $^oC$ (Fig. 4.9a). The high adsorption capacity at low relative pressures ($P/P_0 < 0.05$) and the relatively sharp knee of the isotherm curve are indicative of a predominantly microporous material and a narrow pore size distribution (PSD). Using the QSDFT model, a more detailed estimate of the PSD was obtained (Fig. 4.9b). It is evident that the material porosity is predominantly due to pores with an average diameter of *ca*. ~ 1 nm, with a relatively narrow PSD.

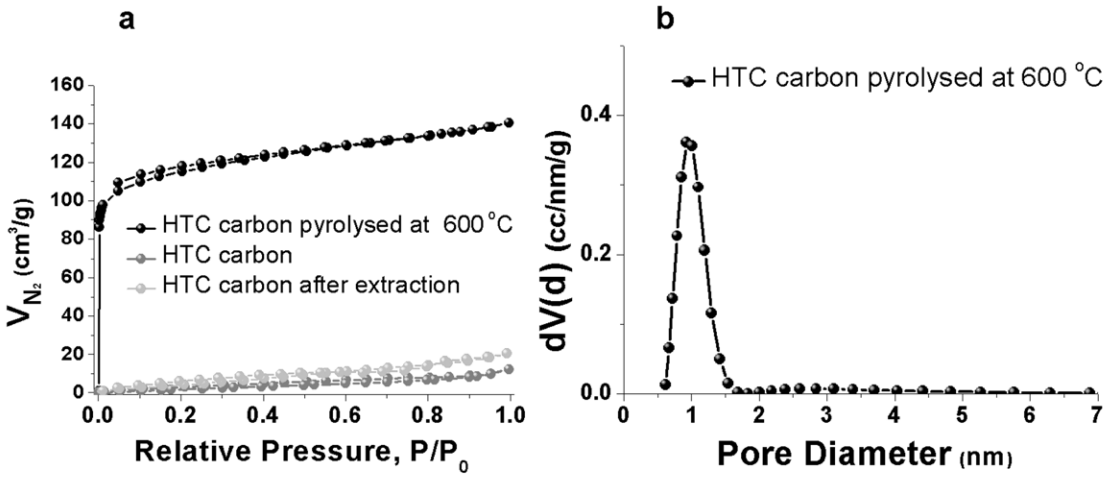


**Figure 4.9: (**a) $N_2$ sorption isotherms of glucose-derived HTC carbon at 180 $^oC$ and then pyrolysed at 600 $^oC$; and (b) QSDFT PSD for glucose-derived HTC carbon at 180 $^oC$ pyrolysed at 600 $^oC$.

Although the QSDFT data analysis indicates a well-defined PSD, its accuracy is questionable, since $N_2$ sorption analysis suffers from several limitations when employed to characterise microporous materials (see section 5.2.2). Therefore, $CO_2$ sorption measurements were also performed to provide a more thorough characterisation of the micropore domains (Fig. 4.10). This further analysis reveals the presence of a relatively high fraction of narrow micropores (0.3 – 0.7 nm, Fig 4.10b) that are normally not effectively detected by $N_2$ sorption. Overall, the combined results of the $N_2$ and $CO_2$ adsorption characterisation indicate that upon pyrolysis HTC carbon develops a relatively high microporosity ( Pore volume ≈ 0.2 $cm^3/g$) mostly characterised by narrow micropores (< 1 nm).

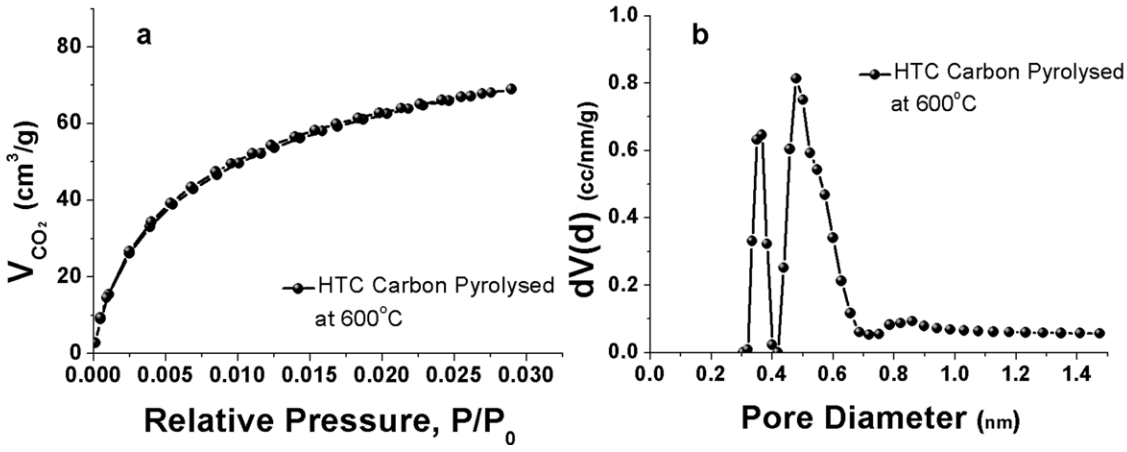


**Figure 4.10:** (a) CO2 sorption isotherms and (b) NLDFT PSD of glucose-derived HTC pyrolysed at 600 °C.

The formation of microporosity, during the thermal degradation of HTC carbon, is due to the combined effects of volatile species elimination (e.g. CO, $CO_2$ and $CH_4$) and formation of condensed aromatic intermediates. Both these processes lead to the development of voids (i.e. pores) between the isotropic pre-graphenic structures, present at this stage. As explained in the previous section, similar trends are generally observed during the thermal degradation of carbon material precursors.[115]

The effects of pyrolysis on the structural texture of HTC carbons were also investigated using HR-TEM (Fig. 4.11). The surface of the sample pyrolysed at 550°C shows an enhanced degree of roughness in comparison to the one of as-synthesised HTC carbon. This evidence can be associated with the formation of short and highly curved aromatic pre-graphenic domains, leading to micropore formation within the carbon structure. An additional increase in the pyrolysis temperature (900 °C) leads to cross-linking between the intermediate aromatic structures and to their resultant growth (Fig. 4.11c), resulting into partial closure of the structural voids developed during the thermal degradation of the HTC carbon. However at this stage, the pre-graphenic intermediate structures are still characterised by a highly curved profile and isotropic orientation due to the presence of non-six member rings within the carbon scaffold.

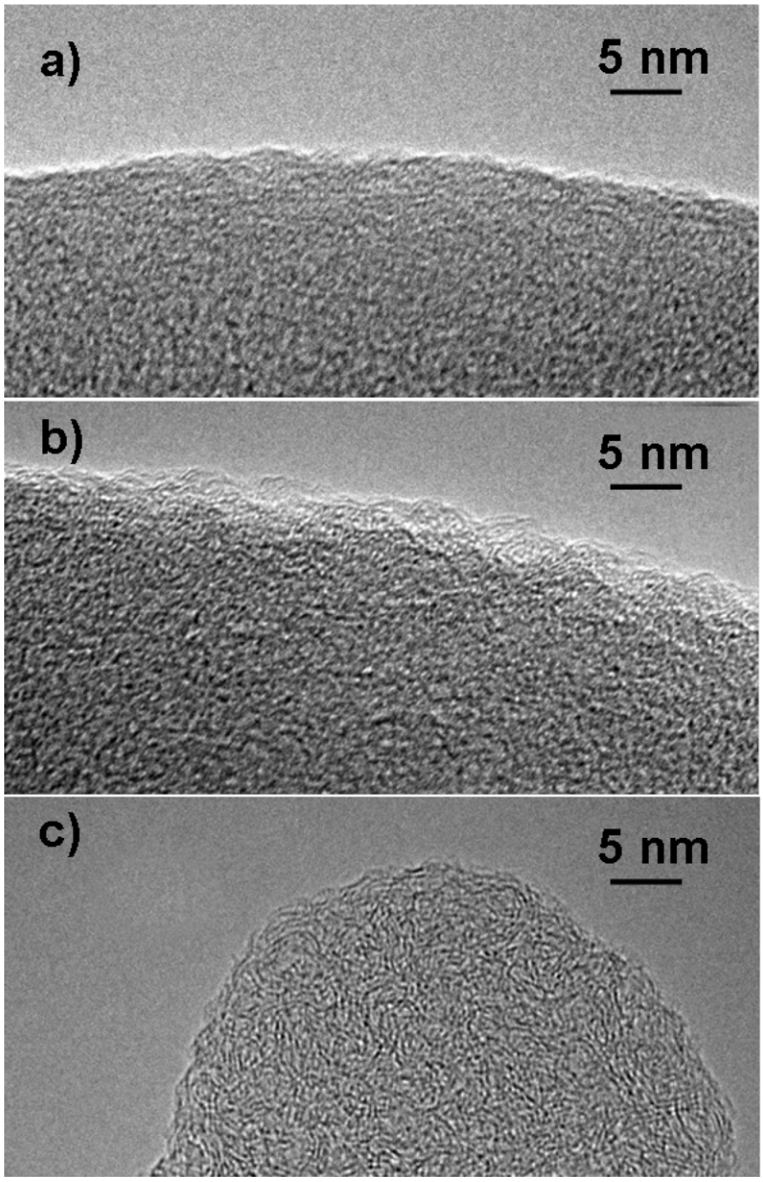


**Figure 4.11:** High resolution TEM of glucose derived HTC synthesised at 180°C a) before and after pyrolysis at b) 550 °C and c) 900 °C.

## 4.4 HTC vs. Pyrolysis: tuning the chemical structure of the HTC carbon.

In the previous section, it was shown how furanic moieties, present in the HTC carbon synthesised at 180 °C, are progressively converted into extended polyaromatic domains under pyrolysis and how the extent of conversion depends on the pyrolysis temperature. This claim was strongly supported by the evidence that the HTC carbon, pyrolysed at low temperatures (i.e. 350 °C), showed a carbon network characterised by the coexistence of both furan building blocks and aromatic arene-like species (Fig. 4.3.2-3). To observe if such an intermediate structure is also generated during the direct pyrolysis of the raw carbon precursors, glucose and starch were thermally

treated under mild conditions (i.e. 350 $^{o}$C under $N_2$) for short times (glucose 3 h (Glu-Δ350$^{o}$C), starch 6 h (Starch-Δ350$^{o}$C)). The synthesised samples were then analysed by $^{13}$C ssNMR and compared to the HTC carbon pyrolysed at 350 $^{o}$C (Fig. 4.12).

The $^{13}$C ssNMR spectrum of Glu-Δ350 $^{o}$C shows the presence of resonances related to un-reacted glucose (peak marked with a star; Fig. 4.12) confirming the mildness of the adopted processing conditions. For the two directly pyrolysed samples, the aromatic region (i.e. δ=105-160 ppm) of their NMR signatures has a different profile than the one of pyrolysed HTC carbon. A detailed analysis suggests that this difference arises mainly from the lack of the δ=118-110 ppm shoulder in the case of the directly pyrolysed samples, indicating the absence of furans. It can however be objected that if this was really the case, then both spectra should not show the resonance at δ =148- 151 ppm, which is instead still present. But such a peak can also be attributed to aromatic carbon of phenol-type moieties, forming during the pyrolysis process, as demonstrated in the previous section and observed in previous literature reports.[116]

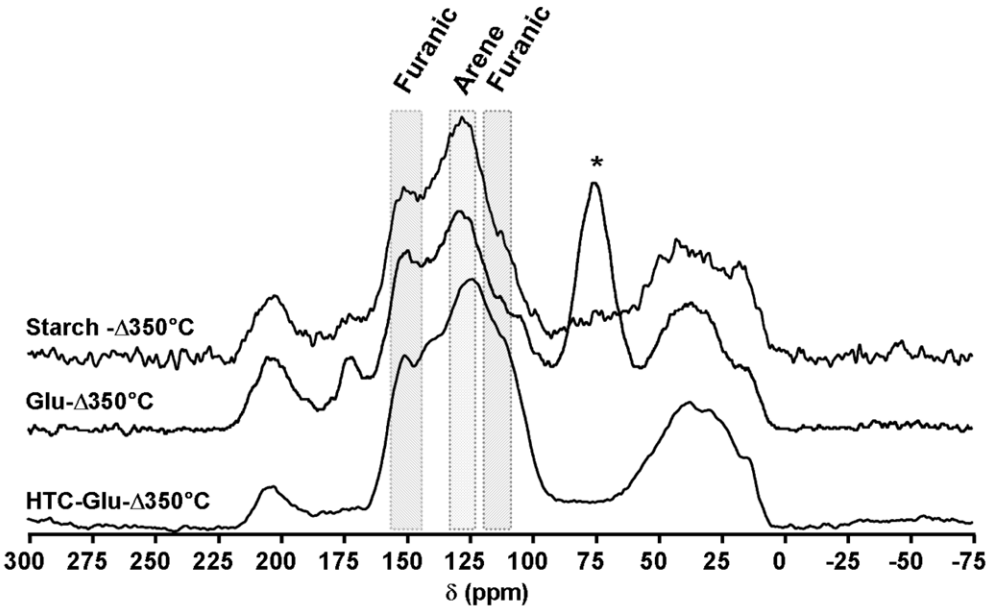


**Figure 4.12:** $^{13}$C CP MAS NMR spectra of a) HTC carbon obtained from glucose at 180$^{o}$C and then pyrolysed (Δ) at 350 $^{o}$C, pyrolysis chars obtained from b) glucose after 3 h and c) starch after 6 h at 350 $^{o}$C. The asterisk refers to resonances corresponding to unreacted glucose.

The results of the comparison between the pyrolysis and HTC of glucose strongly highlight that the hydrothermal treatment of carbohydrates offers an additional intermediate stage between the parent sugar and the polyaromatic char structure, obtained from pyrolysis. Therefore HTC provides a higher degree of control over the

synthesised carbon chemical structure. In order to assess such tunability, a semi-quantitative NMR analysis was used to provide an approximate estimate of the furan to aromatic arene-like species ratio in HTC carbons, obtained at different processing conditions.

Single-pulse (SP) experiments are normally the solution of choice, when ssNMR is employed to obtain a quantitative estimate of the different species present in the analysed sample. However, when the nuclear spin being detected is $^{13}C$, not all samples are best-suited for SP experiments due to the long spin-lattice relaxation times and the low natural abundance of the $^{13}C$ isotope (see Chapter 2). For this reason in this analysis, CP experiments were optimised and used to obtain the estimate of the furan to aromatic arene-like species ratio. Although this kind of measurement is generally known not to provide quantitative information, under the appropriate experimental conditions, it can be employed for semi-quantitative purposes. In particular, if the amount of protons is uniform throughout the analysed samples and the different chemical groups exhibit similar relaxation behaviour under spin-lock, then, for one or more optimum contact times, the CP spectrum can be comparable with the SP experiment and then considered as quantitative. Both criteria are satisfied for the set of experiments taken into consideration during this analysis. The hydrogen content is similar for all the analysed samples (Table 4.2), and the different chemical groups in the aromatic region have a relatively homogenous behaviour at contact times > 1000 μs, as CP experiments at different $\mathbf{t_{cp}}$ values have shown (Fig 4.4b and Fig. 2.11b)

**Table 4.2:** Elemental H content (wt%) of the samples used for the semi-quantitative analysis.

| | | **H (wt%)** |
|---|---|---|
| **HTC-Glu(24 h, 180 °C)** | | 4.69 |
| **HTC-Glu(24 h, 180 °C)-Δ350 °C** | | 4.03 |
| **Set 1 HTC-Glu(24 h) at different temperatures** | 180°C | 4.69 |
| | 200 °C | 4.68 |
| | 240 °C | 4.60 |
| | 280 °C | 4.50 |
| **Set 2 HTC-Glu(240 °C) at different reaction times** | 2hr | 4.63 |
| | 6hr | 4.58 |
| | 24hr | 4.60 |
| | 72hr | 4.51 |

To study the variation of furan to arene species distribution in glucose-derived HTC samples, synthesised under different processing conditions, the following formula is employed:

$$Furan\ to\ arene\ estimate\ (r) = \frac{I(f)}{I(c) + I(d)} \tag{4.1}$$

Where *I(x)* stands for the intensity of peak *x*, which is calculated by integration of the peak area. The Peak List is given in Table 4.3 based on the assignment in Fig 4.4a.

**Table 4.3:** Peak assignment as show in Fig. 4.4 (a).

| Peak | Chemical Shift, δ (ppm) |
|---|---|
| A | 151 |
| B | 143 |
| C | 131 |
| D | 125 |
| E | 118 |
| F | 110 |

The intensity of peak **F** is chosen as an estimate of the furan fraction (Table 4.3). This choice is based on the evidence that its assignment is uniquely related to furan units, since in the 2D $^{13}C$ NMR analysis, no off-diagonal crosspeaks are observed for this chemical shift, except for a resonance at δ = 151 ppm. The same cannot be said of the other furan resonances, since their chemical shifts might overlap with the ones of other species. For example, as seen in the previous section, peak **A** can also be due to aromatic carbons of phenolic species, therefore its intensity cannot be considered to be uniquely related to the furan fraction within the analysed sample. Such ambiguity would introduce further sources of uncertainty in the performed analysis. The arene fraction estimate is instead based on the sum of the intensities of peaks **C** and **D**, since they arise principally from $sp^2$ aromatic arene-like carbons.

The reliability of CP experiments as a tool for quantitative analysis is verified by comparing the *r* values, obtained from $^{13}C$ enriched samples analysed with both SP and CP experiments (Fig 4.13a). Although CP measurements tend to yield an overestimated result (ca. + 0.2), the difference from the SP experiments value is nearly equal for both samples, which are at the extremes of the two analysed samples series from an elemental composition point of view (Table 4.2). As a consequence the comparison between the other samples can be considered fairly reliable.

For the first set of experiments it is evident that the proportion of furan to arene decreases with increasing the HTC processing temperature (Fig. 4.13b). Interestingly

lower *r* values are observed for the HTC samples synthesised at 240 – 280 °C than for the sample post-pyrolysed at 350 °C, indicating that the effects of HTC in such a temperature range on the final carbon chemical structure are actually comparable to pyrolysis at temperatures > 350 °C in terms of carbon aromatisation.

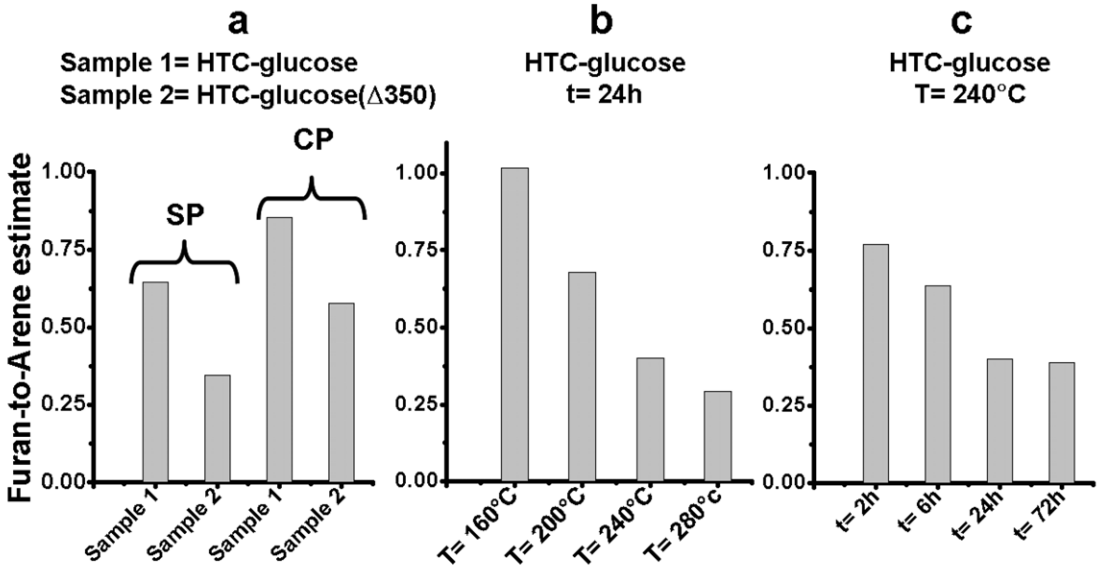


**Figure 4.13:** Furan to arene estimate (r) semi-quantitative analysis of a) comparison of single-pulse (SP) and cross polarization (CP) experiments on two different samples (as-synthesised glucose derived HTC carbon and post pyrolysed at 350 °C) , b) comparison of glucose derived HTC carbon produced at different temperatures after 24 h and c) comparison of glucose-derived HTC carbon at 240 °C after different reaction times.

The results obtained for HTC samples, treated for different reaction times, reflect the observations discussed in the previous chapter (Fig. 4.13c). The furan proportion decreases as reaction time increases, since these species are progressively converted to aromatic arene-like structures. Once a certain degree of conversion is achieved, regardless of increasing reaction time, no further change in the furan / arene distribution is then observed. This demonstrates that presumably the most thermodynamically stable chemical structure at the chosen processing temperature has been formed. At this point, an additional *r* value decrease can only be achieved by further raising the processing temperature.

## 4.5 Summary

In this chapter a detailed study of the HTC carbon pyrolysis has been developed. First, the evolution of the chemical structure at different pyrolysis temperatures has been studied by means of both bulk and surface characterisation techniques. In

particular 2D $^{13}C$ ssNMR experiments have been used to study the evolution of the $^{13}C$ spectrum aromatic region ( $\delta$ = 100 – 155 ppm). Furan based moieties were produced by HTC treatment of hexose sugars at mild processing conditions (Scheme 4.1a). In the case of hexose based polysaccharides the same structures were observed provided that the biopolymers chains were hydrolysable at the used reaction conditions (e.g. amylose, starch) (see chapter 3). Pyrolysis of these HTC carbons at relatively low temperatures (e.g. 350 $^{o}C$) led to an enhanced degree of conjugation / condensation of the carbon structure and to the formation of the initial aromatic arene-like centres (Scheme 4.1b). A further increase in the pyrolysis temperature (i.e. 550-750$^{o}C$) caused the complete loss of the furan species and the formation of extended polyaromatic carbon structures decorated with oxygenated functional groups, which are then removed at progressively higher treatment temperature (Scheme. 4.1c). These latter reaction patterns are common to pyrolysis processes of carbonaceous materials. These structural changes were observed to affect also the surface chemistry, which became increasingly hydrophobic due to the loss of oxygenated groups as indicated by XPS analysis.

Furthermore, comparing the thermal decomposition of HTC carbon before and after Soxhlet extraction, it was possible to observe that the initial stages of HTC carbon pyrolysis are characterised by two main events. The first one corresponds to the evolution of entrapped levulinic acid, whilst the second can be attributed to the carbon scaffold restructuration arising majorly from the furan ring opening and resultant volatile species evolution (i.e. CO, $CO_2$, $H_2O$). As a result of this latter decomposition event, the formation of micropores within the HTC carbon structure was detected and attributed to the presence of voids between the highly curved polyaromatic domains, composing the carbon scaffold at this stage. These findings have demonstrated that pyrolysis of HTC carbons is a powerful post-synthesis functionalisation step. According to the adopted processing temperature, it is possible to precisely tune the chemical structure of the synthesised material tailoring its properties to the end-application (e.g. Adsorption, chromatography, electrochemistry). However the effects on the material texture should not be underestimated, since upon pyrolysis the HTC carbon inevitably develops a microporous character.

The NMR semi-quantitative analysis, developed in the second section of this chapter, has been used to compare HTC carbons to the chars obtained from direct pyrolysis. Its findings have highlighted that hydrothermal treatment of carbohydrates offers an additional intermediate stage between the parent sugar and the polyaromatic char structure, obtained from pyrolysis, allowing a higher degree of control over the chemical structure. Increasing the process temperature of the HTC treatment leads to a higher extent of aromatisation of the synthesised carbons comparable to the one obtained from pyrolysis. Therefore with the aid of a high temperature and pressure equipment, it would be possible to synthesise and tune the chemical structure of HTC carbons, as shown with pyrolysis, with a single pot synthetic process. This would certainly be advantageous from a process engineering point of view.

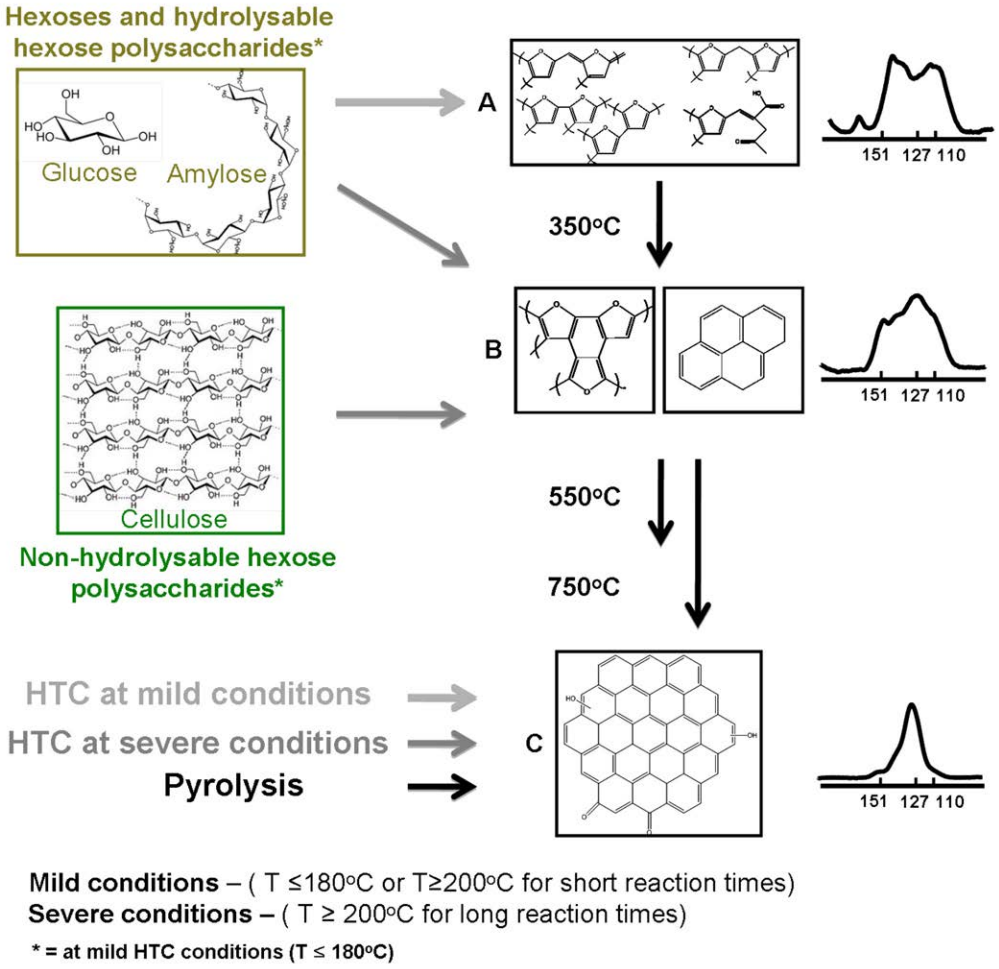


**Scheme 4.1:** Summarising scheme highlighting major structural units of HTC carbons depending on processing conditions and carbon precursor.

# CHAPTER 5 – Chemical activation of biomass derived HTC carbon

## 5.1 Introduction

One of the main limiting factors, hindering the effective exploitation of HTC carbons for several end-applications (e.g. catalysis, separation science, energy production and storage), is their low surface area and porosity. In the case of monosaccharide derived HTC carbons, this problem has been elegantly overcome by using hard\soft-templating strategies or by addition of structural directing agents.[117-119] Such synthetic routes are effective because of the homogeneous nature of the pre-HTC aqueous reaction mixture. On the other hand, in the case of cellulose and more generally of lignocellulosic biomass, the same synthetic approaches are not feasible because of the insolubility of the cellulosic substrate in water. As a consequence, in order to introduce porosity in the lignocellulosic biomass derived HTC carbons, post-synthesis methods are required.

Physical or chemical activation processes are well-known strategies to produce highly porous carbons from coal-derived precursors. Their application to lignocellulosic biomass is widely used, but it is not as effective because of poor yields and low porosity development, arising from the excessive degradation of the organic substrate.[120, 121] In this regard the HTC treated biomass is characterised by a more "coal-like" chemical structure, as a consequence it may represent a more suitable precursor for the production of highly porous activated carbons (ACs).

In this chapter the KOH chemical activation of HTC carbons is investigated as a function of their chemical structure. Some preliminary results on the gas storage performance (i.e. $CO_2$ capture and high pressure $CH_4$ storage) of the synthesised ACs are also presented.

## 5.2 Activated Carbons

### *5.2.1 State of the Art*[122]

ACs are highly porous (surface area > 1000 $m^2/g$) carbon materials, which are synthesised via a carbonisation "activation" process of either an organic or coal precursor. Normally their utilisation for several applications, such as energy storage, gas adsorption and catalysis, is simply justified by the extremely high surface area they are able to provide. However there are some other key properties, which need to

be tailored according to the end use of the ACs. These are the pore volume, pore size distribution (PSD) and surface chemistry, since they have an enormous impact on the overall properties of these materials.[123, 124]

The activation methods are usually divided into 2 different categories: physical and chemical. In the former case, a two-step process is usually employed. The AC precursor is first carbonised and then selectively gasified with an oxidant gas, most frequently $CO_2$ or $H_2O$. During chemical activation, instead, the AC precursor is firstly impregnated with an activating agent (e.g. $ZnCl_2$, $H_3PO_4$, KOH, NaOH), then heat-treated and finally washed to remove all the inorganic side products. Among all the different activation methods, chemical activation using hydroxides (i.e. KOH and NaOH) is the most recent developed methodology. Its adoption has rapidly spread in the past 15 years, since it offers several advantages, in particular when KOH is the activating agent. Above all, higher yields and porosity developments are usually obtained and varying the processing parameters allows precise tuning of the ACs PSD.[125] These are crucial aspects affecting the performance of the synthesised materials and their potential scale-up.

Concerning the mechanism of hydroxide chemical activation, it has been proposed by Linares-Solano and his coworkers that KOH (or NaOH) acts as an oxidant.[126] Redox reactions take place ($6KOH + 2C \rightarrow 2K + 3H_2 + 2K_2CO_3$) etching the carbon and leading to pore formation. However, it has also been demonstrated that the high porosity of the ACs, synthesised via this method, does not solely arise because of the removal of carbon atoms, as for physical activation.[127] The intercalation of $K^+$ or $Na^+$ ions within the structure of the AC precursors seem to play a major role in expanding the AC structure, which is then rearranged into a highly microporous network. The expansion may be due either to the presence of the ions during the thermal decomposition or to the formation of carbonates ( i.e. $K_2CO_3$, $NaCO_3$), characterised by larger molecular volumes.[128] Several parameters of the hydroxides chemical activation process affect the main features of the produced ACs at different extents. A systematic study, developed by Lozano-Castelló and her coworkers, have underlined that the reactivity of the carbon precursor, the carbon to hydroxide ratio, the heat treatment temperature and the $N_2$ flow rate are the crucial variables determining the porous character of the ACs. [126, 129, 130] In some cases their careful control has allowed the production of highly porous ACs ( $S_{BET}$ > 2500-3000 $m^2/g$) with narrow micropore size distributions.

### *5.2.2 Porosity characterisation*[131]

The extremely high porosity of ACs is the key feature which stands behind their successful utilisation in a large variety of applications. Therefore a precise estimate of this structural property is a crucial step for the complete characterisation of these carbon materials.

Although ACs have been intensively investigated in the last 40-50 years, a specific and straightforward protocol to characterise their porous structure does not exist yet. Surprisingly, instead, a very intense debate on the reliability of the different available characterisation methods and models is still ongoing. Gas sorption is undoubtedly the most common characterisation technique. In most of the cases the employed adsorbate is $N_2$, since its utilisation offers several advantages. First of all, there exists an extensive literature on its application for gas sorption measurements, therefore the obtained results can be easily verified and contextualised by comparing with relevant previous studies. Furthermore its low saturation pressure at 77K allows exploring a wide range of relative pressures (from $10^{-8}$ to 1), corresponding to adsorption in all pores sizes (from micropores to macropores).[132]

Nonetheless the reliability of $N_2$ gas sorption in context with microporous carbons characterisation, has been often questioned due to its inability to effectively detect ultramicropores (pore width < 0.7 nm).[133] The main reason behind this limitation is that at 77K the $N_2$ molecules entry into such small pores is kinetically hindered due to their low kinetic energy.[134] As a consequence, the time needed to achieve equilibrium is dramatically prolonged, resulting into unfeasible measuring times for $N_2$ sorption routine experiments. Furthermore due to the large quadrupole moment of $N_2$ molecules, the adsorption in ultramicropores takes place at very low relative pressures ($10^{-8}$- $10^{-5}$). At these values the measurement uncertainty, which can be considered negligible at higher relative pressures ($P/P_0$), may extensively affect the measured $P/P_0$ values yielding unrepresentative isotherms.[125]

The most common model used to fit experimental $N_2$ isotherms is the BET (Brunauer, Emmet, Teller) one. It is generally used to estimate the surface area ($S_{BET}$) of the measured sample. However, in the past, several doubts have been raised concerning the validity and the real meaning of the BET surface area in relation to microporous carbons. The main concerns regard its principal model assumption of multilayer formation, which is appropriate for mesopores, but it does not hold in the case of micropores and in particular of ultramicropores, whose mechanism of gas

adsorption is considered to be micropore filling. Therefore in some cases condensation in micropores may overlap with multilayer formation, yielding BET values unrepresentative of real surface area.[135] For this reason some authors refer to it as apparent BET surface area.[136] Nonetheless, it has been shown recently that reasonable BET surface area values for microporous materials are obtainable if the chosen pressure range for calculations satisfies specific requirements.[137]

Because of these evident limitations of $N_2$ sorption related to the characterisation of microporous carbons, the utilisation of $CO_2$ as an alternative adsorbate for this kind of materials has progressively expanded due to its main comparative advantage. $CO_2$ adsorption is measured at higher temperatures (usually 273K). As a consequence, the gas molecules have sufficient kinetic energy to rapidly enter and probe ultramicropores.[134] For this reason, equilibrium can be achieved in much shorter time and the resultant measurements are more accurate. However, $CO_2$ adsorption has also one main limitation. Because of its high saturation pressure at 273K, it only allows exploring a very narrow relative pressure range (< 0.03) with a standard gas sorption equipment (i.e. not suitable for high pressure). Therefore $CO_2$ sorption is able to fully detect only pores whose diameter is less than 1-1.5 nm (i.e. narrow micropore).[135]

This analysis of the main pros and cons of $N_2$ and $CO_2$ sorption in relation to microporous carbon characterisation strongly emphasises the complementarity of these two adsorbates. It is evident that $CO_2$ can be effectively employed to assess the presence of narrow microporosity. On the other hand, $N_2$ is the adsorbate of choice for supermicropores (0.7-1 nm < pore width < 2 nm) and mesopores (2nm < pore width < 50 nm).[133, 135] For this reason, to assess the porosity of microporous carbons, their combined use is highly recommended and has rapidly expanded. From the literature, it emerges that when microporous materials are characterised by both $N_2$ and $CO_2$ sorption, one of the following three main scenarios is most likely to be encountered (V is the volume of adsorbed gas):[138]

1. $V_{N2} < V_{CO2}$ – The material is characterised mostly by narrow micropore not accessible to $N_2$. These results are a direct consequence of a molecular sieving phenomenon.
2. $V_{N2} \approx V_{CO2}$ – The material is microporous and its PSD is relatively narrow.
3. $V_{N2} > V_{CO2}$ – The material is microporous and its PSD is very broad. Mesopores may also be present.

Apart from the surface area, there are some other crucial parameters defining the porosity of a material. In the case of ACs, the micropore volume and the PSD are of great relevance, since they strongly affect their performance in numerous applications.[139] In the literature there are several available models to estimate these parameters from the gas sorption isotherms. In the field of ACs, the most common ones are:

1. The Dubinin-Radushkevich (DR) model – It best applies to microporous carbons with a narrow PSD.[138] For such materials it is possible to derive a fair estimate of the micropore volumes. On the other hand, the results concerning the PSD are generally considered less reliable.[140] For carbons with broader size distributions, modified versions of the DR equation are necessary, such as the Dubinin-Astakhov or the Dubinin-Stoeckly. However their use is less widespread, because it is much more cumbersome.
2. The Density Functional Theory (DFT) model – Two different models are available: Non-Linear (NLDFT) and Quenched State (QSDFT). The former assumes adsorption taking place on flat, structureless, graphitic pore walls. The latter instead takes into account surface roughness effects.[141] They both yield fairly good estimates of microporous volume and PSD, as confirmed by Monte Carlo Simulation. However, in the case of ACs, generally the values calculated with the QSDFT model tend to be more accurate.[136]

## 5.3 KOH chemical activation of HTC carbons.

In this section the relationship between the chemical structure of HTC carbons and their KOH chemical activation is investigated. For the purpose of this investigation, HTC carbons derived from glucose, cellulose and rye straw were synthesised at different HTC temperatures (sample names *x*-*y*, *x* is the initial of the carbon precursor and *y* the HTC temperature) and then activated at the same processing conditions (KOH ratio = 3, activation temperature 750 °C).[A] EA, SEM and $N_2$-$CO_2$ gas adsorption were used to characterise the synthesised ACs. The complete porosity analysis is presented only for the activation of glucose derived HTC carbons. For cellulose and rye straw only a summary of the overall results is shown, since their KOH chemical activation follows very similar trends to glucose.

[A] The chemical activation and the N2/CO2 sorption measurements were carried out at University of Alicante in a collaboration framework with the group of Prof. Lozano-Castelló. For further details see Appendix.

### *5.3.1 Elemental analysis and scanning electron microscopy of ACs*

The elemental composition of the HTC carbons derived ACs is characterised by very similar values regardless of the different precursors or HTC synthesis conditions (Table 5.1).

**Table 5.1:** EA of HTC carbon derived ACs and pyrolysed HTC carbon

| | Elemental Composition (wt%) | | | |
|---|---|---|---|---|
| **Sample** | **C%** | **H%** | **O%** | **N%** |
| **HTC carbons derived ACs[(a)]** | 84.5-89.0 | 1.5-2.1 | 9.3-13.5 | 0.0-0.1 |
| **HTC-Δ750[(b)]** | 94.0 | 1.7 | 4.2 | 0.1 |

[(a)]The EA of each AC can be found in the appendix section, Table A.Ch5.1, [(b)] From chapter 4

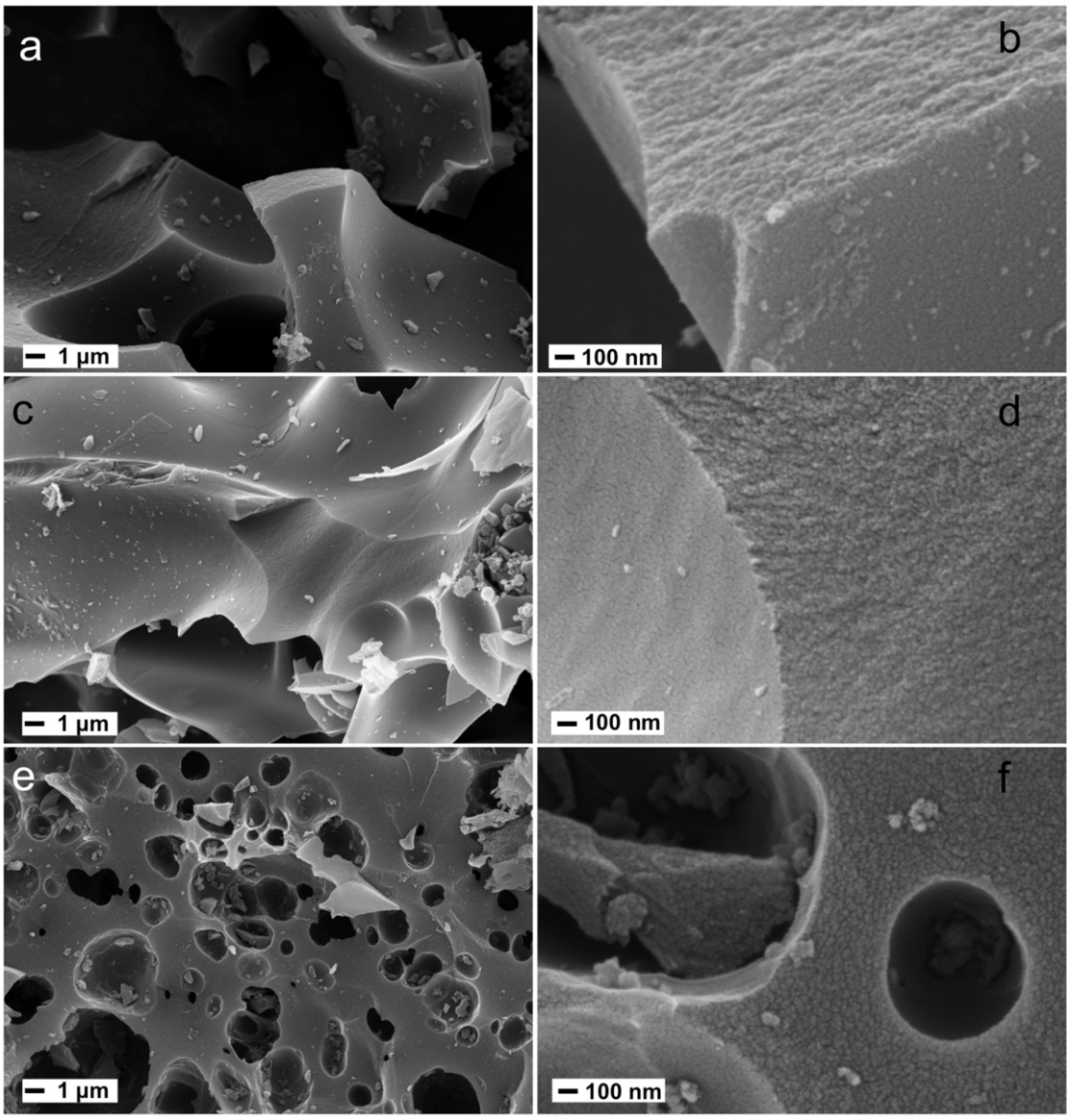


**Figure 5.1:** SEM images of ACs derived from a), b) glucose (G – 240°C), c), d) cellulose (C – 240°C) and e), f) rye straw (RS – 240°C) HTC carbons.

On the other hand, compared to HTC carbons pyrolysed at comparable temperatures (HTC-Δ750), their oxygen content is higher. This difference can be attributed to the higher degree of surface oxidation, which is typically observed after KOH chemical activation. Several oxygen-containing functional groups (e.g. lactone, phenol, quinone) are known to be present on the surface of ACs.[142]

SEM was used to investigate the morphology of ACs derived from glucose, cellulose and rye straw HTC carbons (Fig. 5.1). It is evident that for all three precursors the KOH chemical activation leads to a complete morphological change. The spherical micrometer-sized particles, characterising both glucose and cellulose derived HTC carbons (see section 3.3.1), or the rye straw fibres-like structures, which are still present after HTC treatment, are not observed anymore. The AC materials are now composed of micrometer-sized monolithic fragments with sharp edges. Furthermore higher magnification SEM micrographs (Fig 5.1 b-d-f) show a high level of surface roughness, hinting at the material extensive microporosity.

### *5.3.2 Porosity analysis of ACs produced from glucose derived HTC carbon*

As previously explained, in order to fully characterise the porosity of microporous materials, it is recommendable to employ both $CO_2$ and $N_2$ gas adsorption and to validate the obtained results by analysing them with different isotherms models. For this reason, an analysis based on the combination of the BET, DR and DFT models applied to $N_2$ and $CO_2$ isotherms is developed in this section.

All the $N_2$ isotherms of the ACs produced from glucose derived HTC carbons are characterised by a type I profile (Fig. 5.2a). A more attentive analysis reveals that G-240$^{o}$C has the largest $N_2$ uptake, arising from a higher porosity development than in the cases of G-180$^{o}$C and G-280$^{o}$C. Furthermore, interestingly G-280$^{o}$C $N_2$ isotherm shows a much sharper knee at low relative pressure than G-180$^{o}$C and G-240$^{o}$C. This finding suggests that the PSD of this former sample is much narrower than for the two latter ones. Therefore, it can be deduced that G-180$^{o}$C and G-240$^{o}$C have a higher tendency to develop larger pores during chemical activation than G-280$^{o}$C.

Apart from the total micropore volume (Table 5.2), applying the DR equation to the $N_2$ isotherms (Fig 5.2 b-c-d) can also provide useful information about the ACs PSD. At low $(A/b)^2$ values, the deviation of the experimental results curve (grey full dot line) from the linear fit (red line) is an estimate of the PSD of the sample. Larger deviations correspond to samples with a greater pore fraction out of the micropores

range (i.e. in the mesopores range). According to this criterion, G-240$^0$C (Fig. 5.2c) is characterised by the widest PSD and largest fraction of mesopores. G-180$^o$C (Fig 5.2b) shows a similar trend, although the fraction of mesopores is certainly smaller since the deviation from the linear fit is less pronounced. Contrarily to these first two samples, G-280$^o$C (Fig 5.2c) shows only a negligible deviation from the linear fit suggesting a minor presence of mesopores in this latter sample. The findings, obtained from the DR analysis, are in good agreement with the QSDFT-PSD (Fig. 5.2e). The amount of mesopores present in the G-280$^o$C sample, as already mentioned, is negligible. G-180$^o$C and G-240$^o$C are instead characterised by a large fraction of mesopores, with the latter sample exhibiting the highest amount.

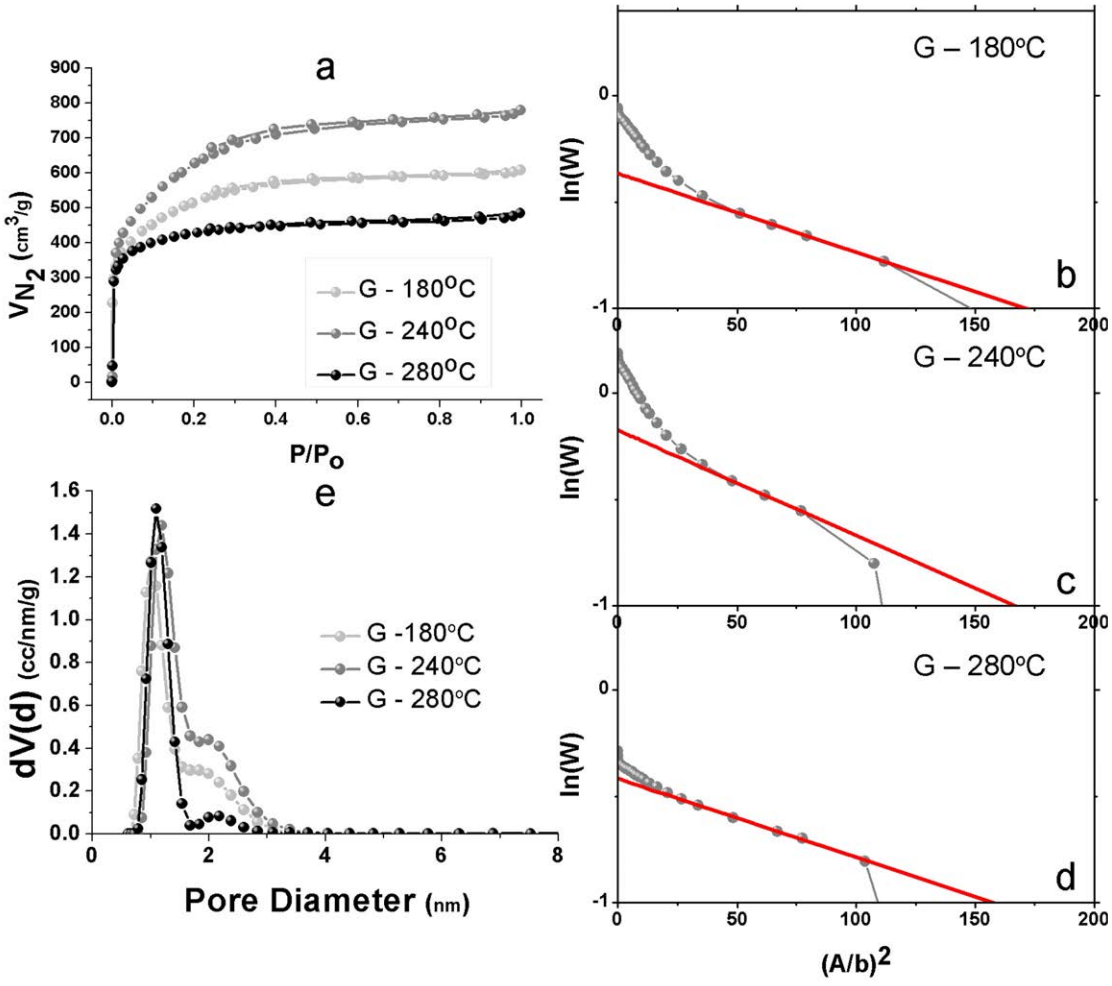


**Figure 5.2**: a) $N_2$ adsorption isotherms, b), c), d) application of DR equation to $N_2$ adsorption isotherms and e) $N_2$ adsorption QSDFT PSD of ACs (G-180$^o$C, G-240$^o$C, G-280$^o$C)

In order to assess the pore volume and the PSD of the narrow microporosity region characterising G-180$^o$C, G-240$^o$C and G-280$^o$C, $CO_2$ adsorption was used, since $N_2$

sorption is not as effective in probing this pore range (See section 5.2.2). It is evident from the measured $CO_2$ isotherms (Fig 5.3 a), that G-280°C has the largest gas uptake followed by G-240°C and then G-180°C. This trend differs from the one observed in $N_2$ sorption and it suggests that G-280°C generates prevalently micropores (majorly narrow micropores) with a narrower PSD. On the other hand, G-180°C and especially G-240°C have the tendency to generate ACs with a broader PSD. This speculation is also confirmed by the NLDFT PSDs, derived from the $CO_2$ isotherms (Fig 5.3 b). Even in the lower micropore range (pore width < 1.0 nm), the PSD of G-280°C is shifted towards smaller pore widths than in the case of G-180°C and G-240°C.

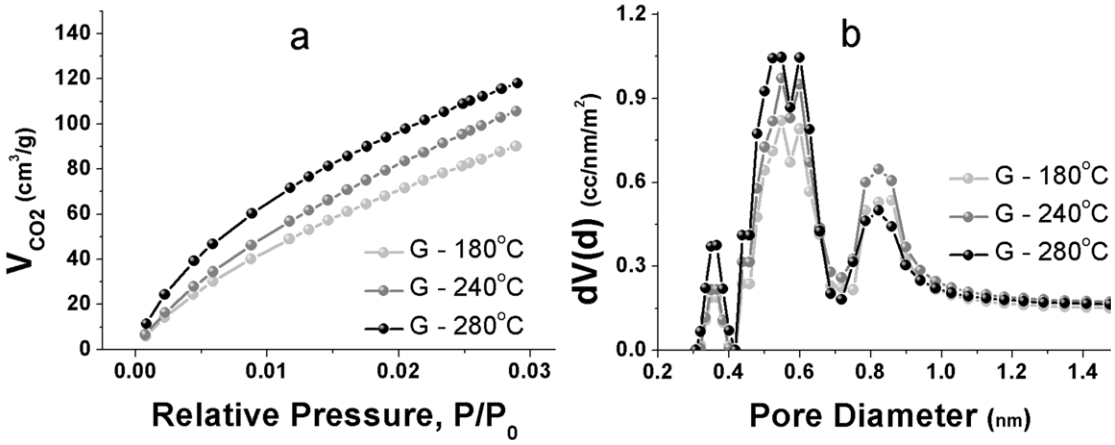


**Figure 5.3:** a) $CO_2$ (273 K) isotherms and b) NLDFT PSD of ACs (G-180°C, G-240°C, G-280°C)

### *5.3.3 Comparing KOH chemical activation of glucose, cellulose and rye straw derived HTC carbons.*

Using the previously discussed models, the key parameters defining the porosity of the ACs (i.e. surface area and pore volume) can be calculated (Fig 5.4, see appendix section for numerical values, Tables A.Ch5.2-4). $V_{CO2\text{-}NLDFT}$ and $V_{CO2\text{-}DR}$ ($V_{CO2\text{-}DR}$ is used for the analysis) can be considered as an approximate estimate of narrow micropore volume. $V_{N2\text{-}DR}$ and $V_{N2\text{-}EX}$ ($V_{N2\text{-}EX}$ is calculated from the experimental isotherm) are respectively approximate estimates of the micropore volume and the total pore volume, accessible to $N_2$ at the measured conditions.

Combining the different pore volume values and the PSDs, obtained by applying the NLDFT and QSDFT models respectively to $CO_2$ and $N_2$ isotherms (Fig. 5.2e and 5.3b), it is possible to obtain a results overview effectively summarising the findings that were highlighted in the previous section.

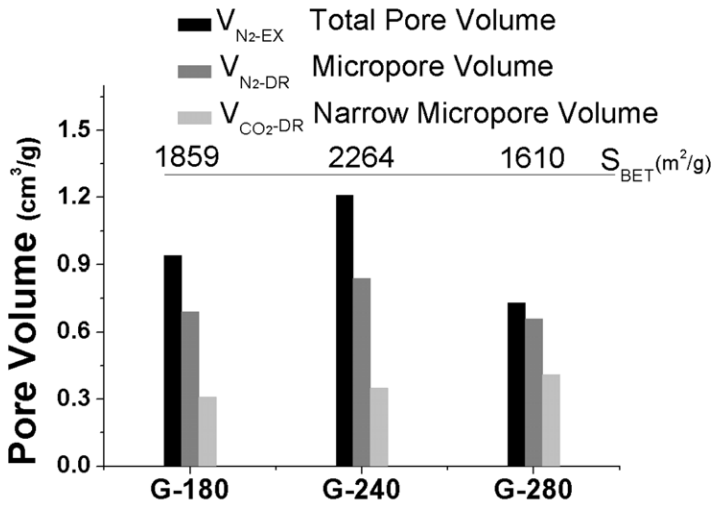


**Figure 5.4:** Calculated surface area (S) and pore volume (V) using different models (subscript) on either $N_2$ or $CO_2$ isotherms for G-180°C, G-240°C, G-280°C

G-240°C is the sample characterised by the highest porosity development, since it shows the largest total pore volume and surface area. At the same time, it has the widest PSD, as indicated by the large difference between its total pore volume (i.e. $V_{N2-EX}$) and narrow micropore volume (i.e. $V_{CO2-DR}$) values. The PSD of G-180°C follows very similar trends to the one of G-240°C. However the extent of porosity development for the former sample is smaller, as indicated by its lower total pore volume and surface area. G-280°C is the case when KOH chemical activation is the least effective. This sample shows the lowest pore volume and surface area. Furthermore, its PSD is much narrower than in the other two samples and is characterised by a very low mesopore fraction, as indicated by the negligible difference between its total pore volume ($V_{N2-EX}$) and micropore volume (i.e. $V_{N2-DR}$) values (≈ 0.05 $cm^3/g$).

Using the same analysis framework, the effects of KOH chemical activation on cellulose and rye straw derived HTC carbons can be effectively analysed and compared to the glucose case (Fig. 5.5-6-7). The porosity analysis for the chemical activation of cellulose derived HTC carbons (C-200, C240 and C-280) show very similar trends to the ones observed for glucose. The highest porosity development is observed for the sample synthesised at 240°C (C-240), as indicated by its highest surface area and total pore volume values. C-200 and C-240 show very similar PSDs, characterised by a significant mesopore fraction (Fig. 5.6). On the other hand, the sample synthesised at 280°C (C-280) shows the lowest surface area and total pore volume, indicating a lower extent of activation. Furthermore, its mesopore volume

fraction is practically negligible, as it was also observed for G-280. Its PSD is mostly characterised by narrow micropores.

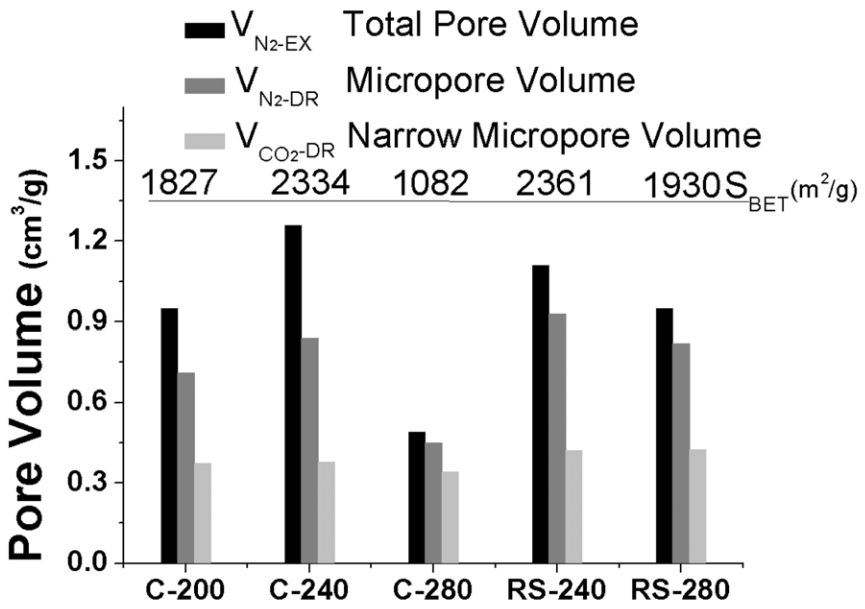


**Figure 5.5:** Calculated surface area (S) and pore volume (V) using different models (subscript) on either $N_2$ or $CO_2$ isotherms for C-200, C-240, C-280, RS-240 and RS 280

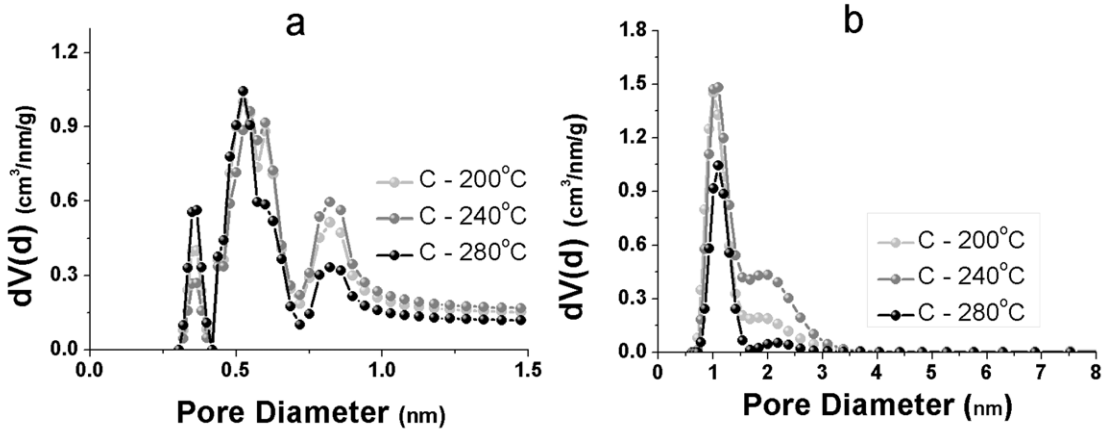


**Figure 5.6:** a) $CO_2$ NLDFT pore size distribution and b) $N_2$ adsorption QSDFT pore size distribution of C-200°C, C-240°C and C-280°C ACs.

In the case of rye straw derived HTC carbons (RS-240, RS 280), KOH chemical activation also generates high surface area and total pore volume ACs (Fig. 5.5). Once again, the sample synthesised at 240°C is characterised by the highest porosity development. However, this time it can be noticed that the development of mesoporosity is less than for glucose and cellulose (Fig. 5.7). Furthermore, as indicated by its relatively high surface area and total pore volume, the sample synthesised at 280°C does not exhibit such a reduced extent of activation as for the

other two carbon precursors. These dissimilarities can be explained by taking into account the more heterogeneous composition and structure of rye straw (i.e. lignin presence and fibrous structure), which may still mildly affect the activation process, regardless of the HTC pre-treatment.

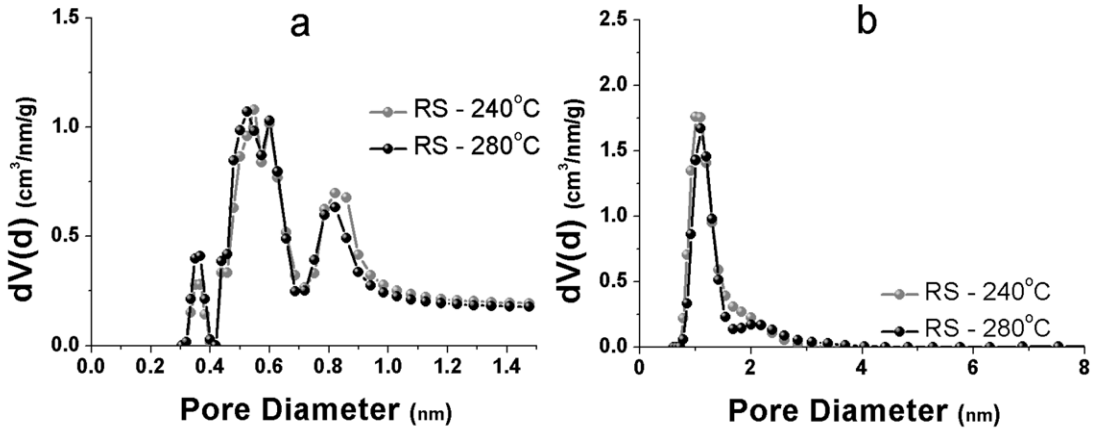


**Figure 5.7:** a) $CO_2$ NLDFT pore size distribution and b) $N_2$ adsorption QSDFT pore size distribution of RS - 240°C and RS – 280°C ACs.

Overall, this analysis highlights that the HTC temperature extensively affects the porosity of the derived ACs. HTC carbons, synthesised at higher temperatures (e.g. 280°C), generate ACs with a lower porosity development and narrower PSDs, whilst the ones, produced at 180-240°C, upon KOH activation, develop a greater porosity characterised by a greater mesopores fraction. These trends can be explained by taking into account the dependence of the chemical structure of HTC carbons upon the synthesis temperature (see Chapters 3-4). More severe HTC processing conditions (i.e. higher temperatures) generate HTC carbons with a higher degree of aromatisation, resulting into enhanced chemical stability and structural order. As observed for the hydroxide activation of several coals, both features are detrimental to the reactivity of the carbon substrate, leading to a reduced porosity development.[128]

## 5.4 The effects of the KOH : HTC carbon ratio on the porosity of ACs.

In this section ACs, produced via KOH activation of rye straw derived HTC carbons (synthesised at 240°C) at different KOH : Carbon Precursor ratio ( KOH ratio = 2:1, 3:1 and 4:1, activation temperature 750 °C), are investigated. This parameter (i.e. KOH ratio) is one of the main variables determining the key features of the ACs porous structure (i.e. surface area, total pore volume and micropore volume). As a

consequence, it can be employed as a term of comparison to determine the effectiveness of HTC temperature as an additional process variable.

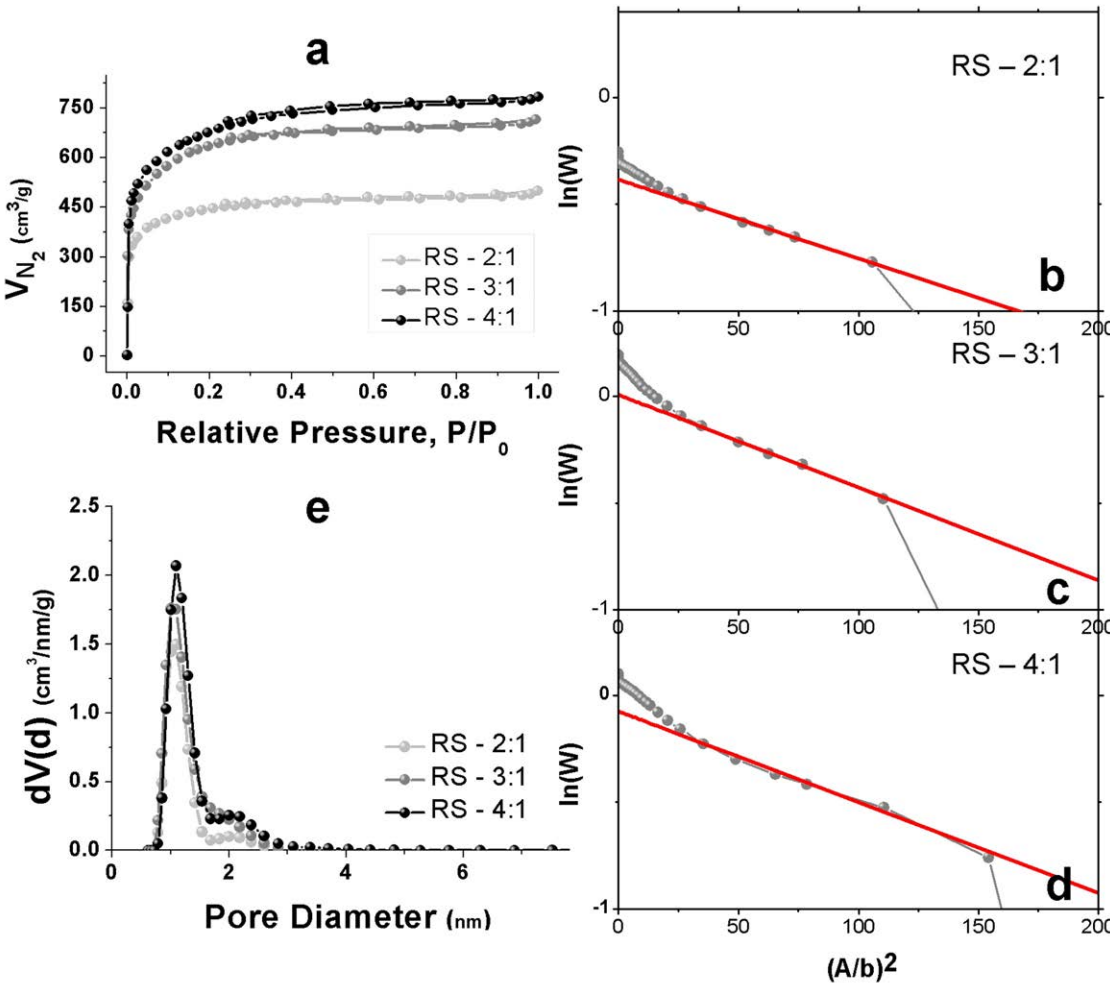


**Figure 5.8:** a) $N_2$ adsorption isotherms, b), c), d) application of DR equation to $N_2$ adsorption isotherms and e) $N_2$ adsorption QSDFT PSD of ACs (RS-2:1, RS-3:1, RS-4:1).

The characterisation of the synthesised ACs (i.e. RS-2:1, RS-3:1, RS-4:1) follows the same structure employed in the previous section. Firstly $N_2$ adsorption was used to characterise the upper micropore and mesopore range (Fig. 5.8). A Type I profile describes all the measured N2 isotherms (Fig. 5.8a). Increasing KOH ratio leads to higher gas uptakes and to a broader PSD, as indicated by the progressive enlargement of the isotherms knee at low relative pressures. This last finding is also confirmed by applying the DR and QSDFT models to the $N_2$ isotherms. In the former case, larger deviations of the experimental results from the linear fit are observed for RS-3:1 and RS-4:1(Fig 5.8b-c-d), indicating a greater fraction of pore volume out of the micropore region. In the latter case, the PSDs highlight how the fraction of mesopore becomes more prominent for high KOH ratio values. From this analysis, it is also

evident that increasing the KOH ratio value from 2:1 to 3:1 affects the ACs porosity to a larger extent than a further increase from 3:1 to 4:1, whose effect on the PSD is relatively negligible.

$CO_2$ gas adsorption was used to probe the narrow microporosity of the synthesised ACs (Fig. 5.9). RS-4:1 shows the largest gas uptake, while RS-2:1 and RS-3:1 approximately achieve the same value (Fig. 5.9a). However, the isotherms overlap in the lower relative pressure region (< 0.010) is a clear evidence of a different PSD also in the narrow micropore range. RS-2:1 has a higher uptake at lower relative pressure, suggesting a higher fraction of very small narrow micropores (< 0.5 nm). RS-3:1 and RS-4:1 isotherms, instead, have broader profiles indicating a shift of the PSD towards larger pore widths. These observations are also confirmed by the obtained NLDFT PSDs (Fig. 5.9b). RS-3:1 and RS-4:1 have very similar PSD with a higher pore fraction in the range 0.5-0.9 nm. On the other hand, RS-2:1 PSD has a major shoulder at pore width values < 0.5 nm.

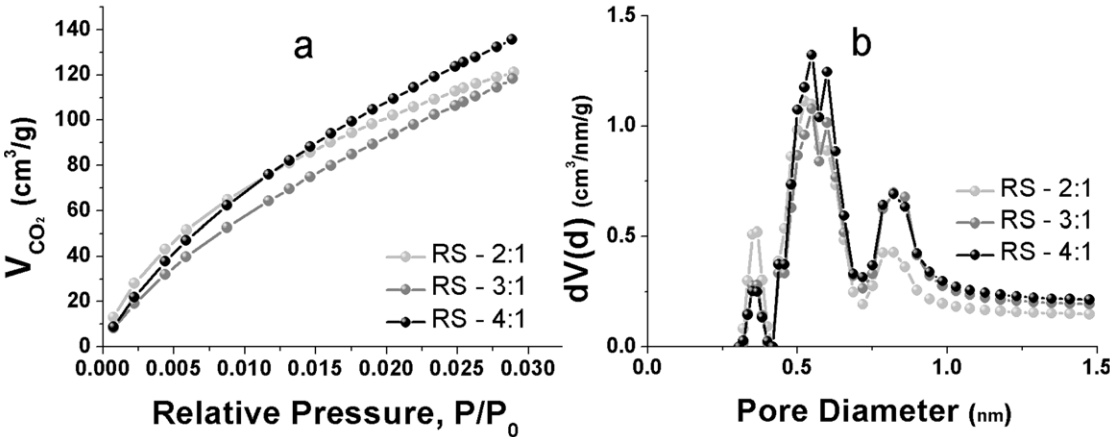


**Figure 5.9:** a) $CO_2$ (273 K) isotherms and b) NLDFT PSD of ACs (RS-2:1, RS-3:1, RS-4:1)

As shown in the previous section, the calculated surface area and pore volume values can be used to effectively summarise the main results, obtained from the porosity characterisation of RS-2:1, RS-3:1 and RS-4:1 (Table 5.10). The existence of a general trend characterising the porosity development of the three ACs is glaring. Low KOH ratio values (2:1) produce a lower extent of activation and favour the formation of microporous ACs with a narrow PSD, as suggested by the reduced difference between its total pore volume (i.e. $V_{N2\text{-}EX}$) and narrow micropore volume (i.e. $V_{CO2\text{-}DR}$) values. Using higher amounts of KOH leads to higher porosity development, as indicated by larger surface area and total pore volume values. However, their increase is partially the result of pore widening, since the PSD for RS-

3:1 and RS-4:1 is clearly more shifted towards the supermicropore and mesopore ranges. These observations are in agreement with the trends generally observed during KOH activation of fossil fuels-derived carbonaceous substrates (e.g. pitch),[129, 143] confirming the similar reactivity of HTC carbons during chemical activation and their resultant high suitability as ACs precursors.

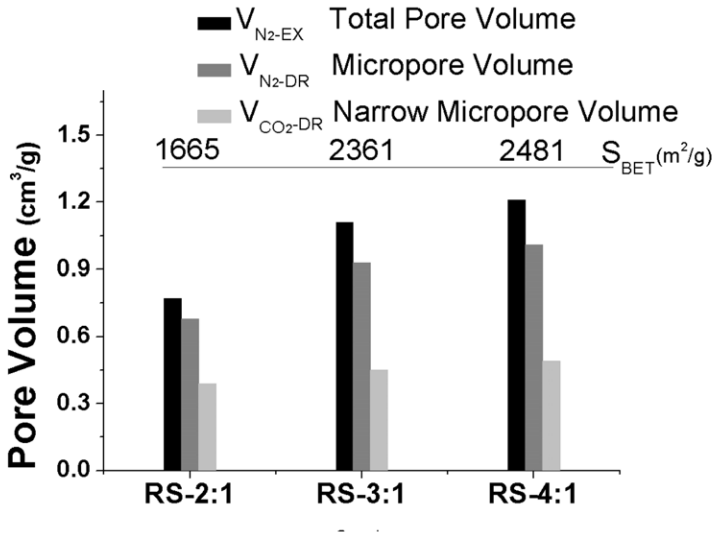


**Figure 5.10:** Calculated surface area (S) and pore volume (V) using different models (subscript) on either $N_2$ or $CO_2$ isotherms for RS-2:1, RS-3:1, RS-4:1

The most interesting outcome of this analysis is provided by the comparison between the results obtained from this section and the previous one (Fig. 5.4-5-10). The effects of HTC temperature on the key parameters, defining the ACs porosity (i.e. surface area, pore volume and PSD), are comparable in magnitude to the ones observed for samples obtained at different KOH ratios. As a consequence, varying the temperature the HTC carbons are synthesised at, allows a degree of control on the ACs' porosity comparable to one of the main variables of the KOH activation process. It is thus obvious that HTC temperature is a key parameter, whose importance should not be underestimated when it comes to tuning the porous structure of HTC carbons derived ACs for specific applications.

## 5.5 Preliminary results of $CO_2$ capture and $CH_4$ storage testing.

In order to evaluate the effectiveness of the HTC derived ACs as $CO_2$ adsorbents, a comparison between their $CO_2$ uptakes at 273 K and the values reported for other ACs or high $CO_2$ adsorbing materials (e.g. microporous polymers, MOFs) is presented (Table 5.2). Although the measuring conditions (i.e. 273K) do not

correspond to real operating ones , since the adsorbents must commonly operate at higher temperatures, this comparison is still a reliable indicator of the potential performance of HTC derived ACs, as $CO_2$ adsorbents. From the collected data, it is evident that the $CO_2$ uptakes of HTC derived ACs outperform the ones of commercially available ACs (e.g. BPL), which are currently widely used in industry for gas separation,[144] and of most of the other adsorbents, which have been chosen as term of comparison because of their excellent reported performances. The mesophase pitch derived ACs are the only materials showing higher $CO_2$ uptakes. However, these values are among the highest ever reported for porous carbon materials and have been obtained after a detailed study, aimed at optimising the ACs adsorption properties. A systematic investigation of the several KOH activation process variables (e.g. heat treatment temperature, $N_2$ flow rate) may also lead to a considerable improvement of the HTC derived ACs performance. Maximisation of the narrow micropore volume would certainly be beneficial, since it has been shown that pores within this size range are the most effective for $CO_2$ adsorption.[145]

**Table 5.2:** $CO_2$ uptakes of different adsorbents at 273K and 1 atm.

| Adsorbent type | $CO_2$ Uptake (mmol/g) | Ref. |
|---|---|---|
| HTC-Carbons derived ACs | 4.02 – 6.06 | This work |
| Commercially Available AC (BPL) | 2.09 – 3.48 | [146, 147] |
| Mesophase Pitch derived ACs | 5.05 – 8.64 | [143] |
| Microporous Organic Polymers (MOPs) | 1.80 – 4.27 | [147, 148] |
| Ultramicroporous Organic Cages | 1.27 – 3.07 | [149] |
| Zeolite 13X | 4.11 | [150] |
| Metal Organic Frameworks (MOFs, ZIF series) | 2.59 – 3.93 | [146, 151] |
| Covalent Organic Frameworks (COFs) | 1.21 – 3.84 | [152] |

Two representative samples of the HTC carbons derived ACs (i.e. G-240 and RS-240) were also tested for high-pressure methane storage (Fig. 5.11). Herein a comparison of their performance with the uptakes of other adsorbents is presented (Table 5.3). Both G-240 and RS-240 show $CH_4$ uptakes comparable with the top performing materials in methane storage applications (e.g. MOFs). These excellent preliminary results could be further improved by tailoring the PSD of the ACs to the optimum pore width value for methane adsorption (ca. 0.8-1.1 nm).[153, 154] Such specific material pore size features could be achieved by tuning the KOH activation process parameters and the chemical structure of the parent HTC carbon, as previously shown (i.e. changing HTC temperature)

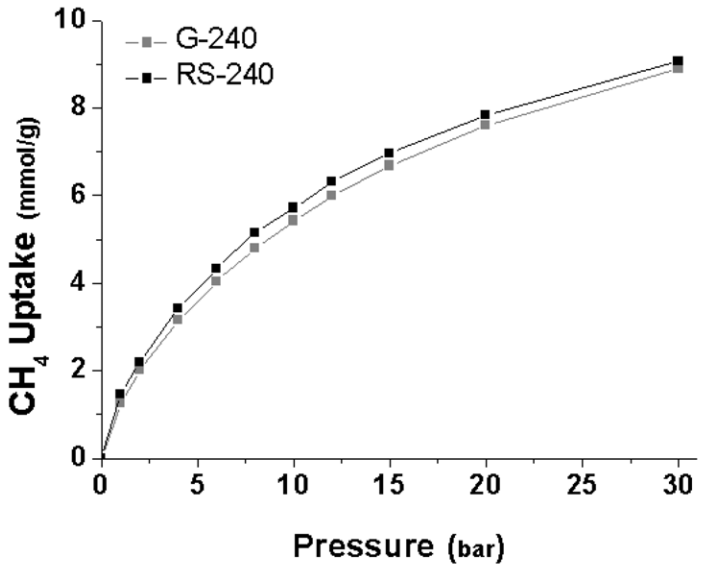


**Figure 5.11:** HTC carbon derived ACs methane adsorption isotherms at 298K.

**Table 5.3:** $CH_4$ uptake of different adsorbents at 298K and 30 bar (if not differently stated in brackets).

| Adsorbent type | $CH_4$ Uptake (mmol/g) | Ref. |
|---|---|---|
| G-240 and RS-240 | 9.0 and 9.1 | This work |
| Commercially available ACs | 3.0 -10.6 (35 bar) | [155, 156] |
| Coal precursors derived ACs | 4.0 – 9.8 | [155] |
| Petroleum pitch based carbon fibres derived ACs | 2.0 – 8.7 | [155] |
| Microporous Organic Polymers (MOPs) | 4.3 – 5.5 (36 bar) | [157] |
| Metal Organic Frameworks (MOFs) | 6.5 – 10.3 (36 bar) | [158] |

## 5.6 Summary.

In this chapter, it has been shown that HTC carbons are excellent precursors for the synthesis of ACs via KOH chemical activation. Regardless of the parent biomass (i.e. glucose, cellulose or rye straw), highly microporous ACs could be generated. The HTC temperature was found to be an extremely influential parameter affecting the porosity development and PSDs of the ACs to the same extent as the KOH ratio (i.e. one of the main KOH activation process variables). The use of higher HTC temperatures (i.e. 280 $^oC$) led to lower porosity development, but to a narrower PSD mostly composed of micropores. On the other hand, KOH chemical activation of HTC carbons, synthesised at lower temperatures (i.e. 180 - 240$^oC$), produced ACs with higher total pore volume and broader PSDs, characterised by a significant mesopores fraction.

Preliminary testing of the synthesised ACs as adsorbents for either $CO_2$ capture or high pressure $CH_4$ storage, yielded very promising results. The measured uptakes of both adsorbates were comparable to top-performing and commercially available

adsorbents usually employed for these end-applications. Further improvements of the synthesised ACs performance could certainly be achieved by optimising the activation and HTC synthesis parameters, in such a way as to tailor their PSDs to the adsorbate. Furthermore, additional testing of the synthesised ACs would also be required, in such a way as to assess their performance under a larger range of operating conditions and to quantify other crucial parameters for their effective application (e.g. packing density).

# CHAPTER 6 – Microalgae: a sustainable and effective precursor for N-doped HTC carbon synthesis.

## 6.1 Introduction

The incorporation of N atoms within the molecular framework of carbon materials has raised several interests in the material science research community, due to its several beneficial effects on the carbon material properties. Depending on the nature of the introduced N-groups, it is possible to distinguish between chemical and structural nitrogen. The latter refers to nitrogen atoms directly embedded within the graphitic carbon layers, while the former comprehends all the N-containing surface functionalities covalently bonded to the carbon framework.[159]

The presence of structural nitrogen atoms, within the graphitic/aromatic structure of carbon materials, contributes with additional electrons to the material conduction band. This results in improved thermal/oxidation stability and higher electrical conductivity,[160, 161] which are both crucial properties for successful application in oxygen reduction reaction catalysis, electrodes in electrochemical double layer capacitors and anode materials in lithium ion batteries.[162-164] Due to the electron-rich nature of nitrogen atoms, N-containing surface functionalities (e.g. amine) have instead demonstrated to be beneficial for the material adsorption properties, especially in the field of $CO_2$ sequestration.[165]

N-doped carbons are commonly synthesised via the pyrolysis of N-containing precursors (e.g. aminated sugars, melamine, N-containing heterocycles) or post-synthesis functionalisation of carbon materials (e.g. treatment with melamine and/or urea and ammonia treatment).[166-168] Recently HTC has proven to be an effective alternative synthetic pathway for the production of homogeneously N-doped carbon material, whose chemical structure can be tuned according to the processing conditions. N-containing monosaccharides/polysaccharides or a mixture of amino acids and sugars have so far been successfully used as N-doped carbon precursors.[37, 169-171] Based on these considerations, HTC of protein-rich biomasses has a high potential to become a green and sustainable synthetic route for the production of $CO_2$-negative N-doped functional carbon materials.

Microalgae are an aquatic biomass generally comprising of proteins, carbohydrates, fats and nucleic acids in varying proportions depending on the species.[172] In particular, the microalgae *Spirulina Platensis*, used in this work,

contain a relatively high protein fraction and therefore a considerable nitrogen content (Table 6.1). Furthermore microalgae are characterised by a very high photosynthetic efficiency and are considered fast growing biomasses. They grow in adverse conditions and extreme environments (i.e. very alkaline water); therefore their cultivation does not compete for spaces aimed at food production.[173, 174] Because of all these chemical and logistic advantages, they represent an ideal precursor for the production of N-doped carbons.

**Table 6.1:** Blue-green *Spirulina Platensis* microalgae composition (wt%) .

| Protein | Carbohydrate | Lipid | Minerals |
|---|---|---|---|
| 66.0 | 19.0 | 7.0 | 8.0 |

In this chapter a study focusing on the hydrothermal treatment of the microalgae *Spirulina Platensis* (simply referred to as "microalgae" in the following text) is presented. The effects of glucose addition to the HTC reaction mixture are also investigated. The microalgae derived HTC products are then chemically activated to produce highly porous N-doped carbons.

## 6.2 Characterisation of microalgae derived HTC carbons

In this section a detailed characterisation of the carbonaceous products, obtained from hydrothermal treatment of microalgae, is presented. In particular the chemical structure of the synthesised HTC products is analysed based on the results yielded by bulk (EA and ssNMR) and surface (IR and XPS) characterisation techniques. Three different samples groups are compared: the raw microalgae, the raw microalgae derived HTC product (HTC-A-*x*, where *x* is the HTC temperature) and the HTC carbon derived from a mixture of microalgae and glucose (HTC-A-*y*G-*x*, where *y* is the glucose to microalgae mass ratio and *x* the HTC temperature).

### *6.2.1 Morphology*

SEM was used to investigate the morphology of raw microalgae and synthesised HTC products (Fig. 6.1). The starting material is composed of globular particles with an average size of several micrometers (10-100 μm). The particle surface is characterised by concave bottomlands and a relatively smooth texture, as indicated by higher magnifications SEM micrographs (Fig. 6.1 a-b). This morphology is typical of spray dried *Spirulina* microalgae. Hydrothermal treatment of the microalgae substrate at

temperatures higher than 180ºC leads to the particle disruption and the formation of irregular agglomerates, showing a high degree of surface roughness (Fig 6.1c-d). Interestingly, it was noticed that the microalgae derived HTC products, obtained at higher temperatures (200-220ºC), show a softer texture similar to the one observed for pitch, indicating the formation of aromatic hydrocarbons of low melting point probably generated from the lipid fraction.

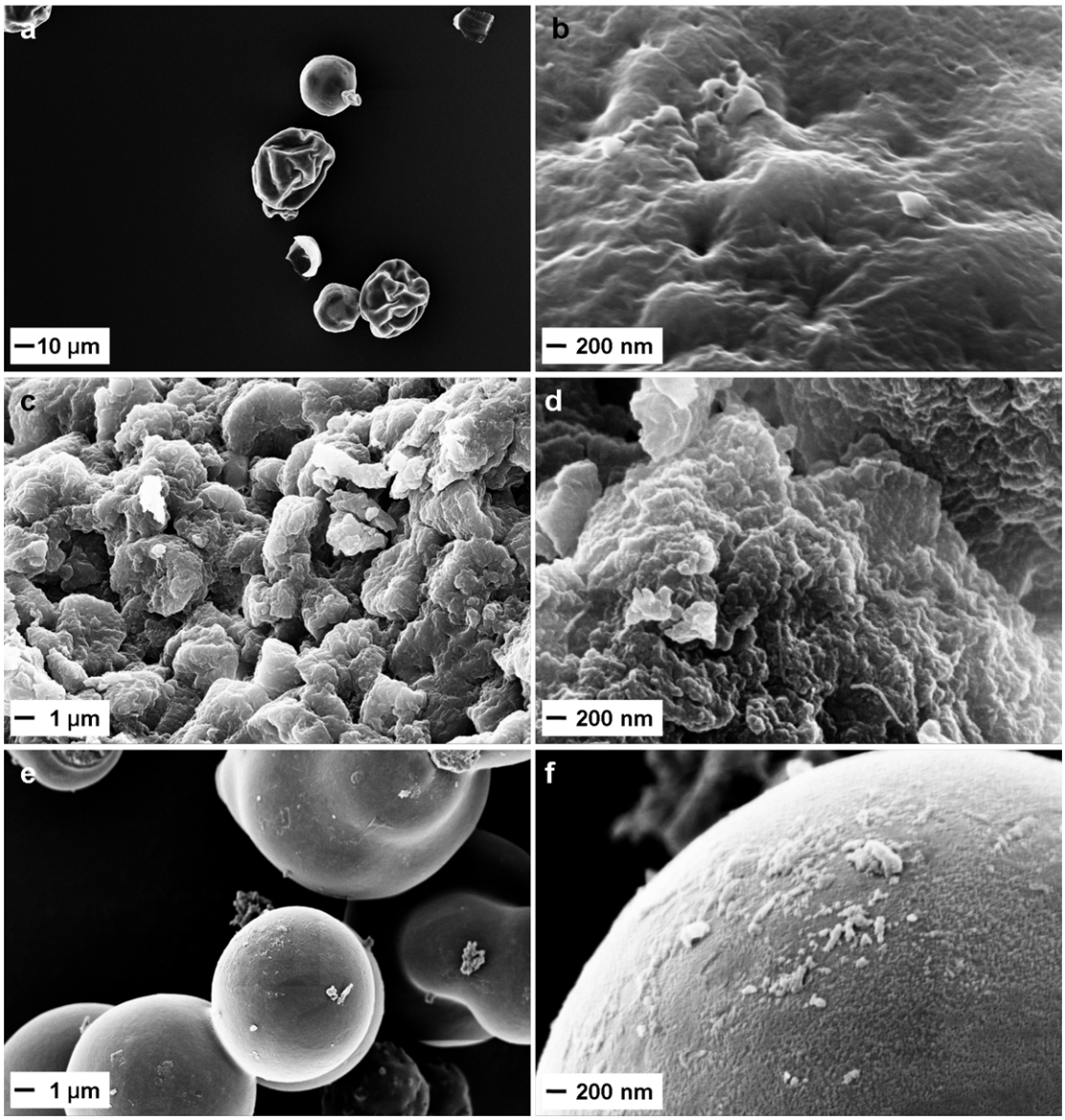


**Figure 6.1:** SEM images of a), b) raw microalgae, c), d) microalgae derived HTC product (200ºC), and e), f) HTC carbon derived from a mixture of glucose and microalgae (220ºC).

On the other hand, when the microalgae substrate is hydrothermally treated in the presence of glucose, the resulting HTC carbon is composed mostly of spherical particles as in the case of pure glucose HTC (Fig 6.1e-f). However, in this case the particles are characterised by a larger average diameter and a rough surface.

### *6.2.2 Bulk chemical composition and structure characterisation*

EA (Table 6.2) reveals that raw microalgae have a significantly high N content (i.e. 11.36%), with the largest portion presumably contained in the polypeptide backbone chains constituting the protein fraction. However minor quantities can also be present in the amino-acids R groups and in the carbohydrate fraction.

HTC treatment of microalgae (HTC-A samples) leads to a major decrease in the heteroatoms (i.e. N and O) contents and is characterised by poor yields. Microalgae derived HTC products, synthesised at progressively higher temperatures, show increasing carbon content and HTC yield indicating a higher extent of carbon fixation. The relatively high H content of these samples underlines their prevalent hydrocarbon nature compared to glucose derived HTC carbons (C% = 66 -70%, H% = 4.5 -5.5 %). This feature presumably arises from the presence of alkyl chains, derived from the lipid fraction, in the microalgae derived HTC products leading to the progressively pitch-like texture of the samples synthesised at higher temperatures, due to a minor extent of hydrocracking reactions.

**Table 6.2:** Elemental composition and HTC yield of raw microalgae and their HTC products.

| | | Elemental Composition (wt%) | | | |
|---|---|---|---|---|---|
| **Sample** | **Yield[(a)]** | **N%** | **C%** | **H%** | **O%** |
| **Raw Microalgae** | - | 11.36 | 47.95 | 7.04 | 33.65 |
| **HTC-A-180** | 18.0 | 6.75 | 65.67 | 8.43 | 17.98 |
| **HTC-A-200** | 20.0 | 6.68 | 67.90 | 8.85 | 15.76 |
| **HTC-A-220** | 23.0 | 6.40 | 70.28 | 9.50 | 13.22 |
| **HTC-A-0.33G-180** | 26.0 | 7.92 | 66.84 | 7.54 | 17.0 |
| **HTC-A-0.67G-180** | 32.0 | 7.31 | 65.94 | 6.92 | 19.30 |
| **HTC-A-1G-180** | 47.5 | 7.10 | 67.39 | 6.34 | 18.47 |
| **HTC-A-0.67G-200** | 31.0 | 7.52 | 70.24 | 6.95 | 14.75 |
| **HTC-A-0.67G-220** | 29.0 | 7.53 | 72.91 | 7.62 | 11.52 |
| **HTC-A-0.67G-240** | 28.0 | 7.32 | 72.74 | 7.84 | 11.67 |

[(a)] Indicating the amount of solid product recovered after HTC as a % of the initial biomass mass.

When glucose is added to the reaction mixture (i.e. samples labelled HC-A-xG-T), beneficial effects are observed with regard to HTC yield and N content. Both quantities are appreciably higher (yield ~ 30 – 50 % and N content ~ 7- 8 wt%), compared to samples prepared from pure microalgae. These results are even more glaring if analysed in terms of nitrogen and carbon efficiency (Figure 6.2) (For N and C efficiency definition see appendix section, Chapter 6, experimental procedure). For the HTC carbons, obtained from a mixture of glucose and microalgae, the amount of

recovered nitrogen is much higher (as high as 6 times) than when no glucose was added (HTC-A samples). This suggests that when microalgae are the only carbon precursor, the N is lost in the form of liquid or volatile decomposition products. Conversely, the addition of glucose allows the fixation of a larger fraction of nitrogen in the synthesised HTC carbons, presumably via co-condensation reactions involving the microalgae degradation/hydrolysis products and the monosaccharides and their derivatives. This speculation is strongly supported by the evidence that the sample showing the highest N-efficiency is the one with the highest glucose to microalgae mass ratio (HTC-A-1G-180).

To a lesser degree, the same trend is also observed for the C-efficiency. The reaction between glucose and the microalgae derived degradation/hydrolysis products plays a major role also in this case, leading to a higher carbon recovery from the microalgae fraction. However it must be taken into account that glucose has a higher C-efficiency, when treated under hydrothermal conditions (≈70%, see chapter 3). Therefore the increased C-efficiency for the samples, where glucose was added, can also be partially due to the formation of HTC carbon solely from glucose.

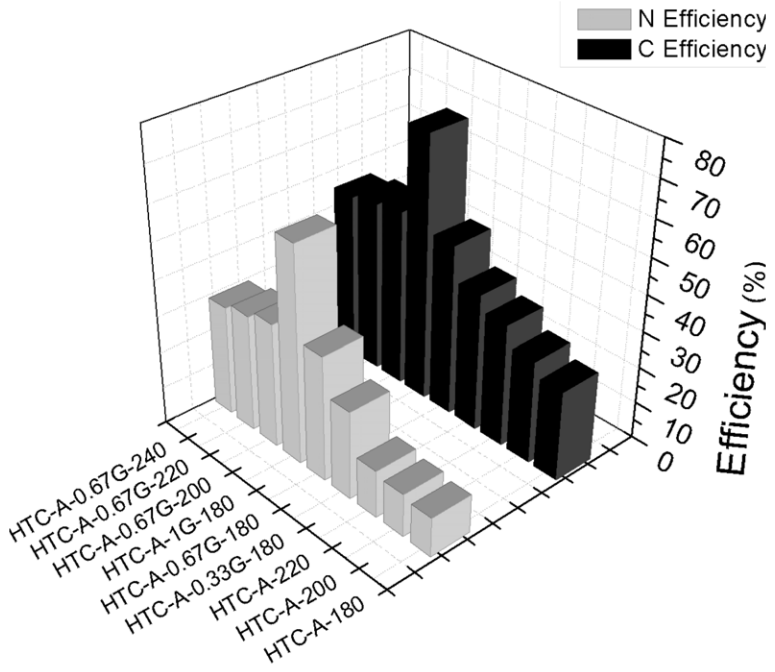


**Figure 6.2:** Nitrogen and carbon efficiency of microalgae derived HTC carbons.

In order to obtain more insights on the chemical structure of microalgae derived HTC carbons, $^{13}C$ ssNMR was used to analyse representative samples from each group (Figure 6.3). The raw microalgae spectrum is characterised by an intense and sharp peak at approximately δ=170-175ppm, ascribable majorly to the amide bond of

the protein fraction, although a minor contribution arising from the lipids carboxylic acids groups may also be present. This resonance is coupled to the one at δ ≈ 50-60 ppm, related to the amino acid NH-substituted α-carbons.[175] Only minor peaks characterise the aromatic region (δ≈105-155ppm), the most intense one (δ=125-129 ppm, Aromatic-C) can be assigned to olefinic, arene or N-containing heterocycles aromatic structures, present either in the lipid fraction or in the amino acids R groups (e.g. Phenylalanine, for an amino acid breakdown composition, see appendix section Table A.Ch6.1).[176] The peaks in the δ=55-105 ppm region are related to the oxygenated carbons contained in the carbohydrate fraction present in the microalgae. An intense and broad peak characterises the aliphatic region (δ≈0-45 ppm) indicating the heterogeneous nature of the paraffinic carbons, contained either in the lipid fraction or in the amino acids R groups.[177]

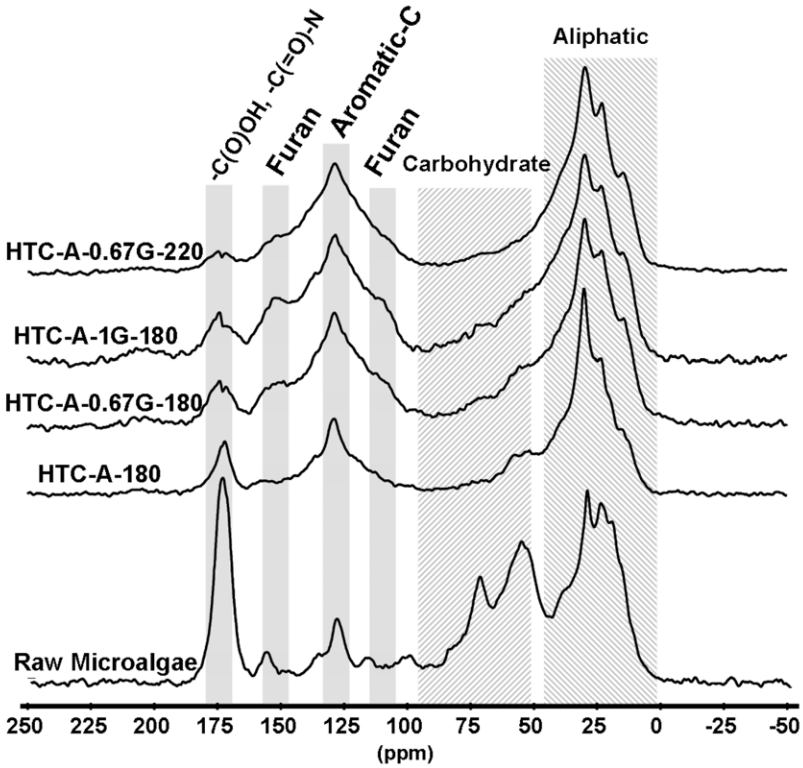


**Figure 6.3**: $^{13}C$ CP MAS NMR spectra of raw microalgae and microalgae derived HTC carbons with and without glucose addition and at different HTC temperatures.

Hydrothermal treatment has severe effects on the chemical structure and composition of microalgae, as indicated by the corresponding $^{13}C$ NMR spectrum (HTC-A-180). The intensities of both resonances at δ=170-175 ppm and δ=50-60 ppm dramatically decrease indicating the loss of amide and –NH-substituted α-

carbons. The peaks in the carbohydrate region practically disappear suggesting the depletion of the sugar fraction. However, except for a minor intensity increase and broadening of the Aromatic-C peak (δ=125-129ppm), no major concomitant peak formation is observed. Interestingly, the main resonances, characterising the $^{13}C$ spectrum, are within the aliphatic region suggesting that the microalgae derived HTC product is mostly composed of alkyl chains and therefore characterised by a strong hydrocarbon character. Considering the low yield of HTC-A-180 (i.e. 18%), the presence of such structures can be mostly attributed to the fatty acids alkyl chains that have been incorporated within the microalgae derived HTC product.

For the samples, where glucose was added to the reaction mixture, the same changes can be observed in the $^{13}C$ ssNMR spectra with one major difference: an intense and very broad peak characterises the aromatic region. The shoulders at δ=110-118ppm and 148-151 ppm can be attributed respectively to the furan β- and α-carbons generated from glucose HTC. However the increase in intensity of the aromatic-C peak may be due to the formation of N-containing heterocyclic aromatic structures, resonating within this range. These species may be the result of Maillard-type cascade reactions involving monosaccharides and amino acids, produced from protein hydrolysis.[178] Higher amounts of glucose (HTC-A-1.5G-180) lead to a further intensity increase of the aromatic region resonances, indicating a higher extent of reaction. On the other hand, increasing the HTC temperature (HTC-A-0.67G-220) causes the loss of the furan shoulders, since at more severe processing conditions these species are converted into more thermally stable aromatic arene-like structures (see chapters 3 and 4).

Solid state CP MAS NMR experiments were also carried out on the $^{15}N$ nuclei, to obtain a more detailed and direct characterisation of the nitrogen species (Fig. 6.4). Unfortunately, these experiments suffer from reduced sensitivity because of two main reasons. First of all, the low natural isotopic abundance of $^{15}N$ allows detecting only the most abundant species within a sample. Furthermore, only N species with protons in their closest proximities can be observed due to unfavourable magnetisation transfer between the protons and the $^{15}N$ nuclei (see chapter 2).

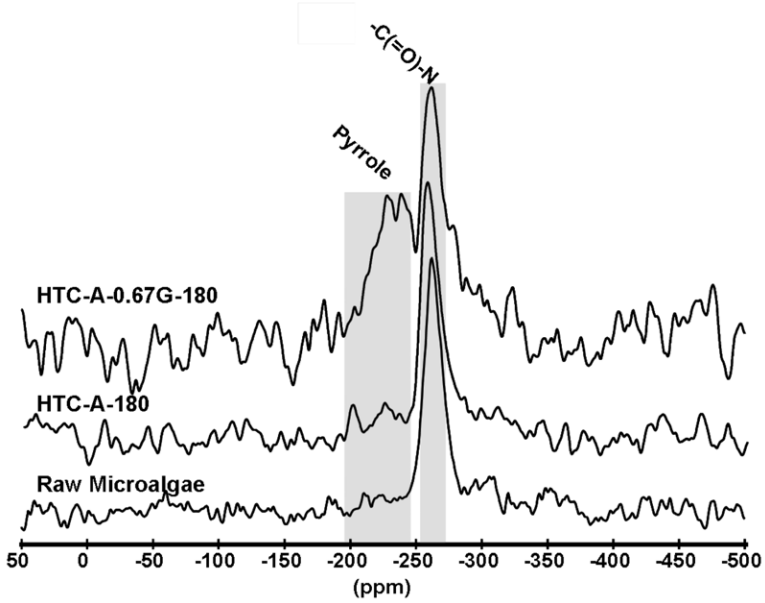


**Figure 6.4:** $^{15}$N CP MAS NMR spectra of raw microalgae and microalgae derived HTC carbons with and without glucose addition.

The $^{15}$N NMR spectrum of raw microalgae is characterised by one single sharp and intense resonance at δ= -260ppm, ascribable to amide groups. This observation confirms that in the raw material the largest nitrogen fraction is contained in the polypeptide chains. No major changes are observed in the case of hydrothermally treated microalgae (HTC-A-180), except for a decrease of the resonance intensity indicated by a higher peak to noise ratio. As a consequence, it can be deduced that the relatively low fraction of nitrogen left after HTC (≈10%, Fig 6.2) is still conserved into amide groups, which have not been fully hydrolysed presumably because of the raw microalgae limited solubility in water. On the other hand, for HTC carbons obtained from a mixture of microalgae and glucose, it is evident that the amide peak intensity is even more reduced and there is a second very broad peak at δ= -200-250ppm, corresponding to pyrrolic-N.[179] These species are formed from the reaction between reducing sugars and compounds possessing a free amino group (i.e. amino acids) via Maillard-type cascade reactions under hydrothermal conditions.[169, 178, 180] The possibility of more condensed N-containing aromatic structures (e.g. Pyridine, quaternary nitrogen species), being formed during microalgae/glucose HTC, cannot be discarded based on these evidences, since, as previously anticipated, non protonated nitrogen species cannot be detected during $^{15}$N CP experiments. For this reason, this ssNMR analysis has been complemented with additional FTIR and XPS measurements.

### *6.2.3 Surface chemical structure characterisation*

In order to fully characterise the microalgae derived HTC carbons and spot any differences between the chemical structure in the bulk and at the surface, the same five samples were investigated by FTIR (Fig. 6.5).

Two intense bands in the region 1500-1750 $cm^{-1}$ characterise the raw microalgae spectrum. The first one is centred at ca. 1640 $cm^{-1}$ (Amide I) and is ascribable to C=O stretching vibration in peptide linkages. However the broad peak profile suggests that the presence of side contributions at ca. 1740 and 1620 $cm^{-1}$, respectively corresponding to C=O stretching vibration of ester carbonyl from lipids and C=C stretching vibration of olefinic and aromatic compounds, may also be present. The second intense band at ca. 1530 $cm^{-1}$ (Amide II) arises mainly from in-plane N-H bending vibration. The broad absorption band at ca. 1030 $cm^{-1}$ (Carbohydrate I) can be instead attributed to the carbohydrate fraction in particular to the presence of C-O, C-O-C and C-C species. The higher wavenumbers absorption bands at 2845-2960 and 3110-3670 $cm^{-1}$ are assigned respectively to the stretching vibrations of C-H in alkanes, present in the lipids fraction, and carbohydrate O-H or primary amines N-H.

The IR spectrum of hydrothermally treated microalgae (HTC-A-180) confirms the findings obtained from ssNMR analysis. The Amide I and II bands loose most of their intensity, indicating the depletion of the polypeptide chains. In particular, the Amide I band is now sharper and shifted at ca. 1620 $cm^{-1}$, suggesting that C=C species belonging to aromatic/olefinic structures are now more abundant. The alkanes absorption band shows a dramatic relative intensity increase, confirming that the microalgae derived HTC product has a strong hydrocarbon character. The carbohydrate band disappearance, coupled to the reduced intensity of the 3110-3670 $cm^{-1}$ peak, suggests that the sugar fraction originally present in the raw microalgae has fully reacted. These evidences are also valid for the samples where glucose was added (HTC-A-0.67G-180, HTC-A-1G-180 and HTC-A-0.67G-220). However one main difference characterises the alkane absorption band: its relative intensity significantly decreases in these latter samples, suggesting that the glucose addition drastically reduces the hydrocarbon character of the microalgae derived HTC product, presumably due to a dilution effect. Furthermore it is evident that the relative intensity decrease of the Amide I and II bands is even more pronounced for the HTC-A-*y*G-*x* samples. The 1500-1750 $cm^{-1}$ region is now characterised by one broad peak, indicating the heterogeneity of the species contributing to its intensity. It is possible

that the nitrogen, previously contained in the amide bonds, has now been incorporated into N-containing heterocyclic aromatic structures (e.g. Pyrrole, pyridine), characterised by absorbance bands within this wavenumber range.[181] However IR experiments are not sufficient to draw such conclusions. For this reason a complementary XPS analysis is presented later on. The spectrum of HTC-A-0.67G-220 shows more defined features in the 690-820 $cm^{-1}$ region, arising from C-H out of plane bending vibrations of aromatic structures.[182] This observation confirms that increasing HTC temperature leads to the progressive formation of more condensed and aromatic carbon species.

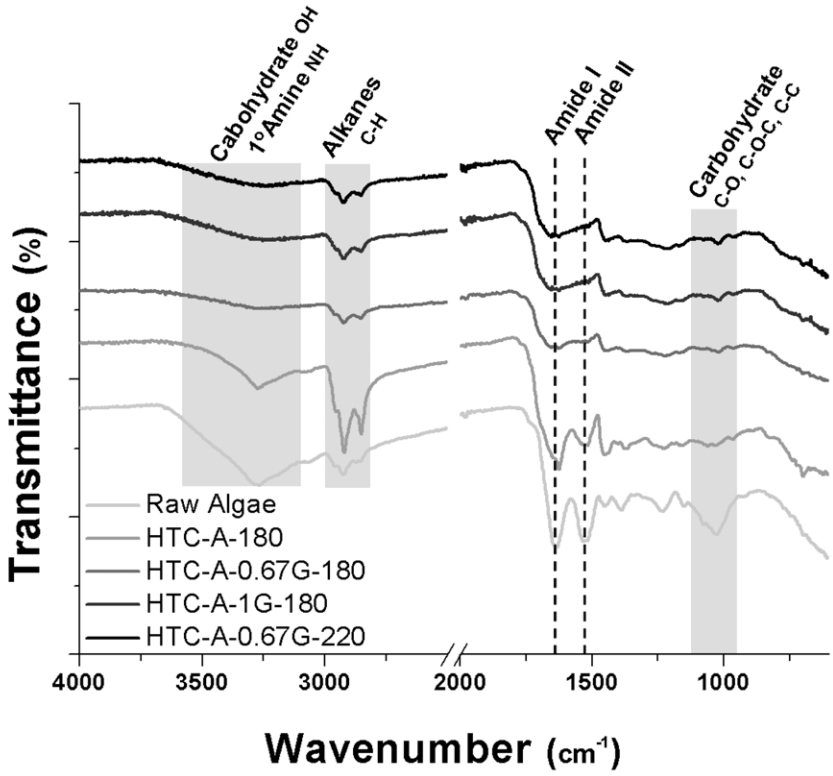


**Figure 6.5:** FTIR spectra of raw microalgae and microalgae derived HTC carbons with and without glucose addition and at different HTC temperatures.

The XPS analysis highlights that the C 1(s) envelope of raw microalgae (Fig. 6.6a) is characterised by three main peaks at 285.0 eV (C-C and C-$H_x$), 286.5 eV (C-O-H (hydroxyl), C-O-C (ether) and C-N (amine)) and 288.0 eV (C=O (carbonyl) and N-C=O (amide)) with a minor contribution at 289.0 eV (O=C-O (acid or ester)). The relatively high intensity of the 286.5 and 288.0 eV peaks underlines the presence of a considerable amount of heteroatom containing species (i.e. O and N) in the raw microalgae, which are presumably part of the protein and sugar fractions.

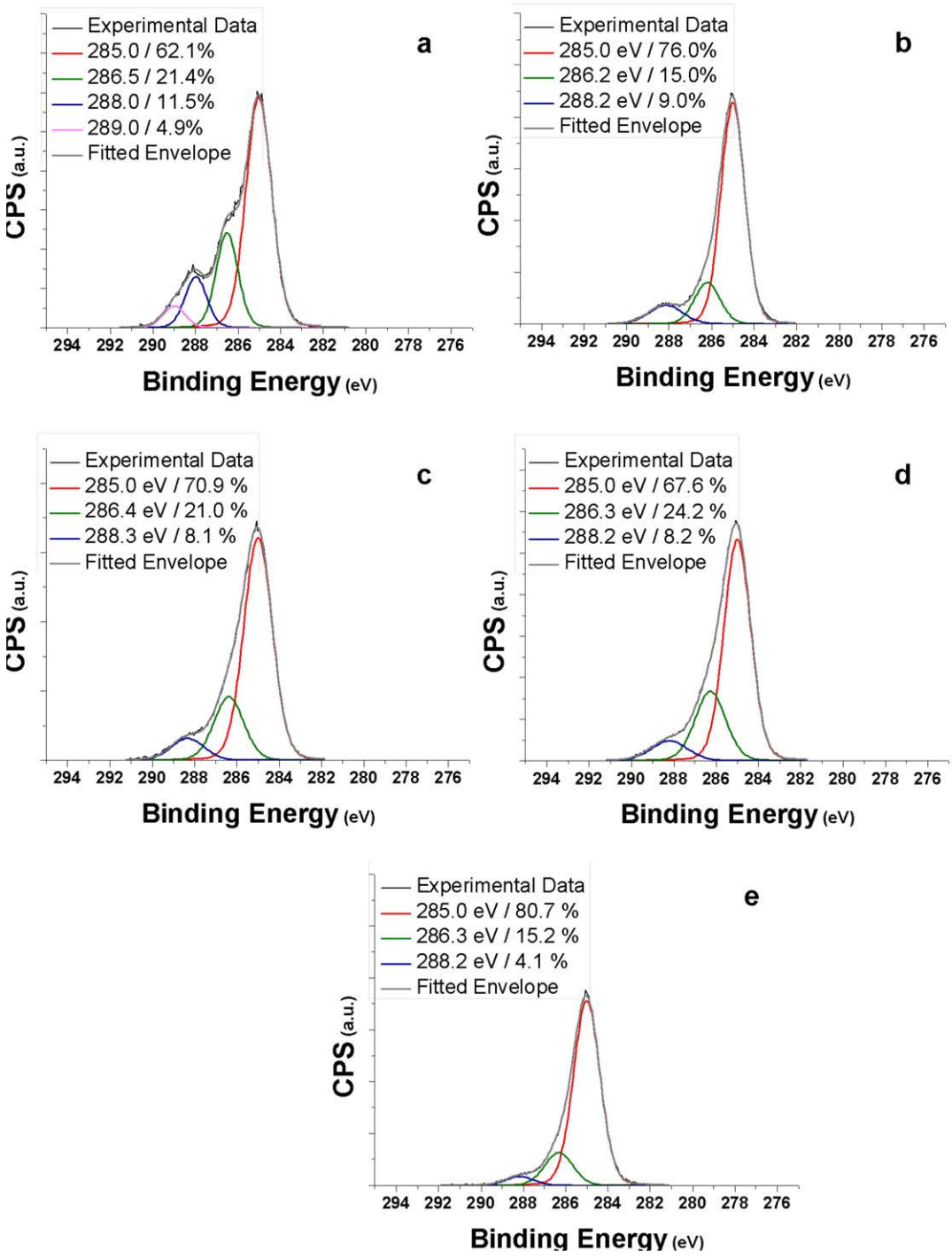


**Figure 6.6:** C1(s) photoelectron envelope of a) Raw microalgae, b) HTC-A-180, c) HTC-A-0.67G-180, d) HTC-A-1G-180 and e) HTC-A-0.67G-220.

In the case of the HTC product, obtained from raw microalgae (HTC-A-180, Fig. 6.6b), the contribution of the 286.2 and 288.2 eV peaks to the overall C 1(s) envelope is highly reduced indicating that during HTC a large fraction of the N and O containing species are depleted. This finding is in agreement with the FTIR and ssNMR analysis revealing the progressive disappearance of both the protein

(indicated by the amide bond) and sugar fractions during hydrothermal treatment and the strong hydrocarbon character of the microalgae derived HTC product (HTC-A-180). Interestingly, for the HTC carbons obtained from a mixture of glucose and microalgae (Fig. 6.6c-d), only the 288.3 eV peak exhibits a reduced intensity. On the other hand the 286.3-286.4 eV peak is still very prominent. These observations can be respectively correlated to the progressive hydrolysis of proteins during HTC and the formation of aromatic heterocycles (e.g. furan, pyrrole, pyridine), as also suggested by NMR. These results further support the eventuality of Maillard type cascade reactions taking place and yielding N-containing aromatic heterocycles, As previously observed with FTIR and ssNMR, increasing the HTC temperature leads to a further loss of the heteroatom containing functionalities and to an increase of the carbon content as indicated by the reduced intensities of the 286.3 and 288.2 eV peaks for the HTC-A-0.67G-220 sample (Fig. 6.6e).

In order to obtain more insights on the N-species nature and in particular to ascertain the presence of non-protonated N-containing aromatic heterocycles, an analysis of the N 1(s) photoelectron envelope was carried out (Fig. 6.7). However, this characterisation technique also suffers from a sensitivity limitation, arising from the fact that several N-species overlap over a very narrow binding energy range (i.e. pyrrole ≈ 400.2 eV, amide ≈ 399.9 eV, amine ≈ 399.3 eV, pyridine ≈ 398.9 eV).[183] As a consequence, it allows discerning which ones are the most abundant species, but in the case of very broad N 1(s) envelopes spotting the overlap of minor contributions may become a hard task.

As expected based on FTIR and ssNMR results, the N 1(s) envelope of raw microalgae (Fig. 6.7a) is mostly characterised by one single peak at ca. 400.0 eV ascribable to amide bonds, present in the proteins polypeptide chains. In the case of hydrothermally treated microalgae, the most intense peak remains the one at 400.0 eV indicating that the relatively low fraction of nitrogen left, after hydrothermal treatment is still present in the amide form. However, as anticipated, it is not possible to discard the possibility of a pyrrole contribution (400.2 eV), generated from the reaction between the hydrolysed amino acids and the carbohydrate minor fraction, originally present in the raw microalgae. Furthermore two other less significant contributions can be observed at ca. 401.9 and 398.7 eV, which can be respectively

assigned to quaternary-N and pyridinic-N species, presumably formed as minor products during the carbonisation process.

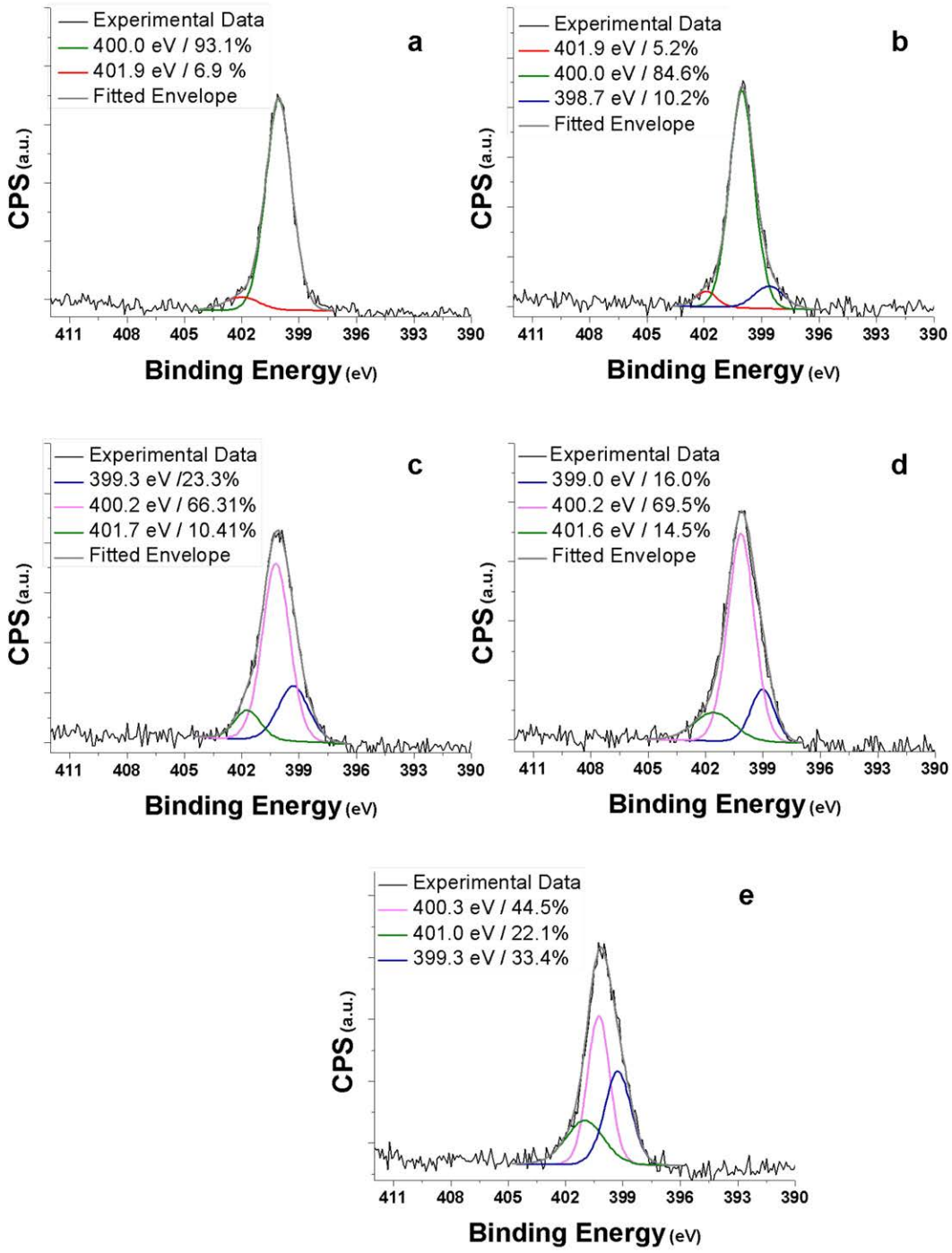


**Figure 6.7:** N1(s) photoelectron envelope of a) Raw microalgae, b) HTC-A-180, c) HTC-A-0.67G-180, d) HTC-A-1G-180 and e) HTC-A-0.67G-220.

Upon glucose addition, the N 1(s) envelopes of microalgae derived HTC carbons (HTC-A-0.67G-180 and HTC-A-1G-180, Fig. 6.7c-d), broadens and slightly shifts to

higher binding energy values. The envelope best fit reveals that there are at least three main contributions. The most intense one at 400.2 eV can be assigned to pyrrolic-N. The other two, as previously seen, are ascribable to quaternary-N (401.0 – 401.7 eV) and pyrdinic-N species (399.0 – 399.3 eV). The relative intensity of these latter peaks is higher than in HTC-A-180 suggesting a higher extent of formation of such species when glucose is added. These results further prove the incorporation of N into aromatic heterocycles when glucose is present, as previously suggested based on FTIR and ssNMR results. It should be mentioned that for the peak at 399.0-399.3 eV, there is also the possibility of amine groups contribution (399.3 eV). However these N-moieties were not detected with $^{15}N$ ssNMR, therefore they may be present only in minimal quantities. Interestingly higher HTC temperatures (HTC-A-0.67G-220, Fig 6.7e) lead to an increase of the side peaks contributions (401.0 and 399.3 eV) suggesting a higher extent of formation of more condensed N-containing aromatic structures at more severe processing conditions, as also observed during the pyrolysis of N-containing carbonaceous precursors.[184]

Combining the results obtained from EA, ssNMR, FTIR and XPS, it is possible to depict one clear scenario for the HTC of microalgae. When treated under hydrothermal conditions, the polypeptide chains constituting the protein fraction are denaturated/hydrolysed into their amino acid building blocks. If the raw microalgae are the only carbon precursor, then the amino acids remain in solution and therefore most of the nitrogen content is lost in the liquid phase. The microalgae derived HTC product is characterised by a prevalent hydrocarbon character, arising from the abundant alkyl chains fraction majorly derived from the fatty acids component. Adding glucose allows fixating a higher amount of nitrogen in the synthesised HTC carbon via Maillard type cascade reactions, involving the amino groups of the amino acids and the carbonyl moieties, present in the carbohydrates and their derivatives. Furthermore the glucose degradation products (e.g. levulinic acid and formic acid) may enhance the amide bonds hydrolysis by lowering the solution pH and acting as an in-situ catalyst. These reactions patterns have already been reported for the reaction of carbohydrate and amino acids under hydrothermal conditions, and have been observed to produce a carbonaceous material containing N-heterocyclic aromatic structures, such as pyrrole, pyridine and quaternary-N species.[169, 178] Such N-containing moieties are also present in the HTC carbons derived from the mixture of microalgae and glucose, confirming the similarity of the reaction mechanisms.

Additionally, depending on the HTC temperature, the N-species distribution can be tuned. More severe processing conditions (i.e. higher temperature) favour more stable aromatic structures (e.g. pyridine and quaternary-N species), as a result of a higher extent of carbonisation.

## 6.3 KOH chemical activation of microalgae derived N-doped HTC carbon

The major drawback of the microalgae derived N-doped HTC carbons, hindering their effective exploitation for several end-applications (e.g. $CO_2$ capture, supercapacitors) is their low surface area and porosity (For a $N_2$ sorption isotherm of a representative sample, see appendix section Fig. A.Ch6.1). In order to improve these properties, KOH chemical activation of one representative sample (HTC-A-0.67G-180) was attempted. Several different ACs (HTC-AG-*x*-*y*) were synthesised using different KOH to HTC carbon ratio (*x*) and activation temperatures (*y*). The synthesised materials were characterised by EA and XPS, in such a way as to investigate the effects of chemical activation on the N content. $N_2$ and $CO_2$ gas adsorption were employed to analyse the porous structure of the ACs, as shown in Chapter 5.

### *6.3.1 Nitrogen content and surface chemical structure*

EA reveals that the ACs still contain relatively high N amounts, although chemical activation of the microalgae derived HTC carbons leads to a major decrease of this quantity (Table 6.3). The existence of a well-defined trend between all the analysed samples is evident. More severe processing conditions (i.e. higher KOH ratio or temperature) produce ACs with a lower N content, due to the preferential oxidation of N-containing functionalities during the activation process.[185] The increased oxidised character of the microalgae derived ACs is also confirmed by the relatively high O amounts, typical of carbons synthesised via KOH chemical activation, as also observed in the previous chapter.

**Table 6.3:** Elemental composition of ACs derived from microalgae HTC carbons.

| | Elemental Composition (wt%) | | | |
|---|---|---|---|---|
| **Sample** | **N%** | **C%** | **H%** | **O%** |
| **HTC-AG-2-650** | 3.63 | 82.54 | 1.30 | 11.17 |
| **HTC-AG-1-700** | 3.89 | 84.61 | 0.98 | 10.13 |
| **HTC-AG-2-700** | 2.87 | 84.92 | 0.90 | 10.93 |
| **HTC-AG-4-700** | 2.52 | 85.61 | 0.76 | 10.72 |
| **HTC-AG-2-750** | 2.92 | 88.79 | 0.81 | 7.08 |

Two representative ACs (HTC-AG-2-650 and HTC-AG-2-700) were also characterised by XPS, in order to identify the main functionalities present at the surface. The high-resolution C1(s) spectra of both samples show four main contributions (Fig. 6.8). The first and most intense one at 285.0 eV is ascribable to C-C and C-H moieties present within the carbon framework. The relatively high intensities of the two following peaks at 266.4-266.5 and 288.3-288.7 eV underline the high abundance of heteroatoms within the carbon surface structures. The largest fraction certainly corresponds to O-containing functional groups (e.g. lactone, hydroxyl, quinone), as indicated by EA. However contributions from N-containing moieties are also a possibility, due to the presence of a relevant amount of N in both samples. The last peak at 290.2-290.7 eV is assigned to $\pi \rightarrow \pi^*$ shake up satellites indicative of extended aromatic features.

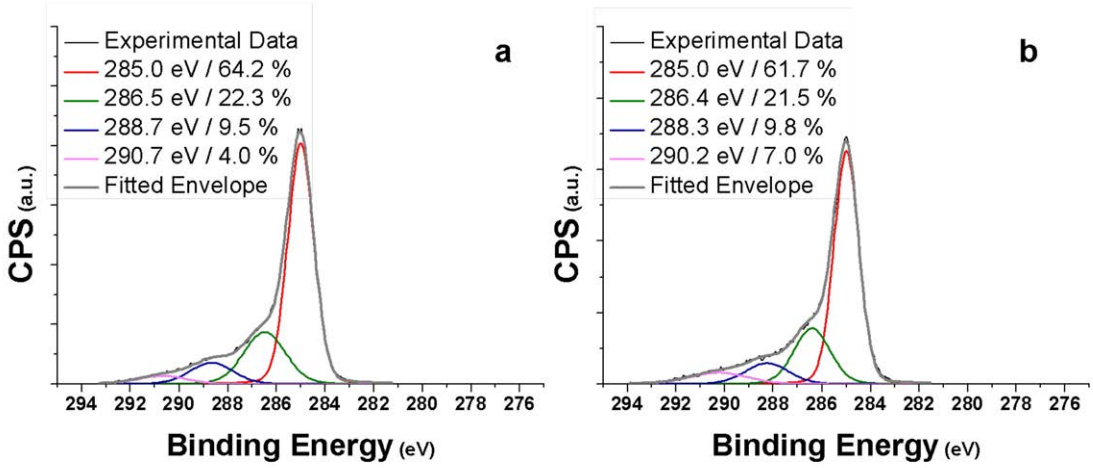


**Figure 6.8:** C1(s) photoelectron envelope of a) HTC-AG-2-650 and b) HTC-AG-2-700

The high-resolution N1(s) spectra of both samples were also analysed and deconvoluted in order to obtain more insights on the N-containing species (Fig. 6.9). Three main contributions are visible at 398.8-398.9 eV (pyridinic-N), 400.1-400.2 eV (pyrrolic or pyridonic-N) and 401.5 eV (quaternary-N), as for the parent microalgae-glucose derived HTC carbon (i.e. HTC-A-0.67G-180).[186] However for the two ACs the central peak (i.e. 400.1-400.2 eV) shows a reduced relative intensity indicating the preferential loss of pyrrolic-N during chemical activation, due to its lower thermal stability. A further evidence, supporting this observation, is that the AC, synthesised at higher temperature (HTC-AG-2-700), has a larger fraction of pyridinic and quaternary-N than HTC-AG-2-650, confirming the increasing relative abundance of these species at more severe processing conditions. Furthermore, due to the oxidative

environment present during KOH chemical activation, the central peak of the N1(s) envelope (i.e. 400.2 eV) may also include major contributions from more oxidised N-containing species (e.g. pyridone) characterised by binding energies very close to the pyrrole one.[187]

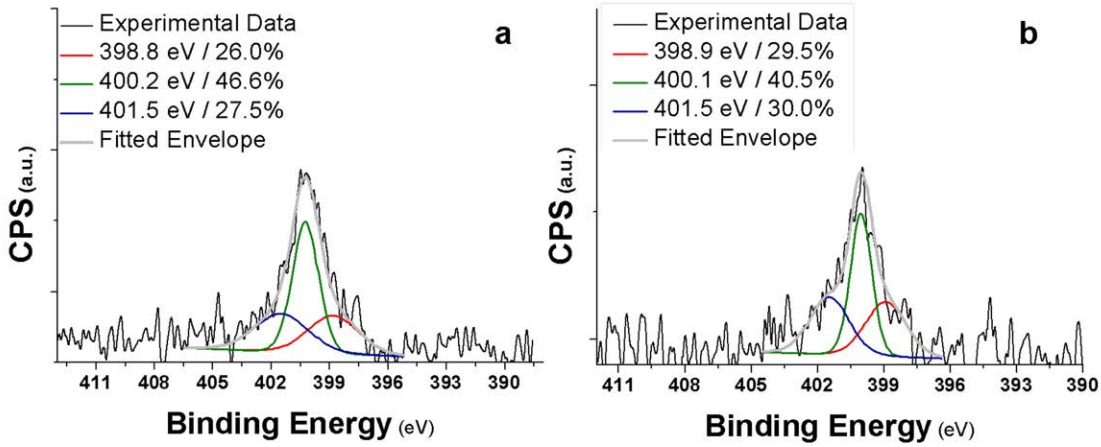


**Figure 6.9:** C1(s) photoelectron envelope of a) HTC-AG-2-650 and b) HTC-AG-2-700

### *6.3.2 Porosity characterisation*

As shown in the previous chapter, from $N_2$ and $CO_2$ adsorption isotherms it is possible to calculate the main parameters defining the porosity of the ACs, which can then be used to effectively compare different samples (Fig. 6.10).

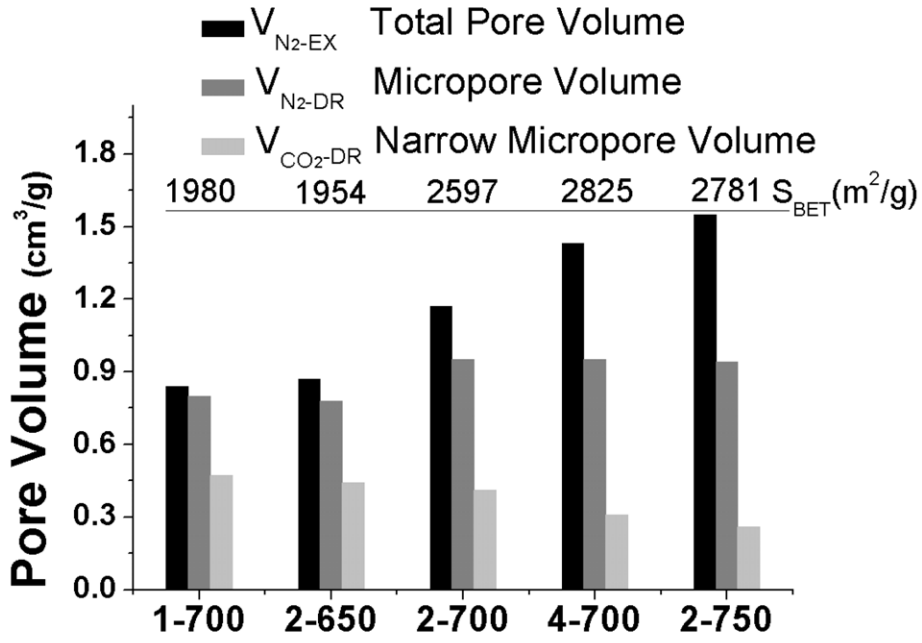


**Table 6.10:** Calculated surface area (S) and pore volume (V) using different models (subscript) on either $N_2$ or $CO_2$ isotherms for C-200, C-240, C-280, RS-240 and RS 280

At all the employed processing conditions KOH chemical activation generates a very high porosity development, as indicated by the extremely high surface area and pore volume values of all the synthesised samples. Furthermore it can be observed that choosing determinate KOH ratios or temperatures allows tuning the porosity distribution. Milder processing conditions (i.e. low temperature and KOH ratio) generate mostly microporous ACs, with the largest fraction of pores being in the narrow micropore range. Higher activation temperatures or KOH ratios lead to the development of greater porosity, as indicated by the larger surface area and total pore volume values. At the same time the porosity of these ACs is characterised by a larger fraction of mesopores, which have been probably generated by a pore-widening process as suggested by the reduced portion of narrow micropores.

The PSDs of the ACs have been also estimated applying NLDFT and QSDFT models, respectively to $CO_2$ and $N_2$ isotherms (Fig. 6.11). The obtained results reflect the previous findings. The PSDs of the ACs, synthesised at more severe processing conditions (i.e. high activation temperatures and KOH ratio), are much broader and extend into the mesopore range. On the other hand a large fraction of narrow micropore and the absence of mesopores characterise the porosity of ACs, synthesised using low KOH ratio and activation temperatures.

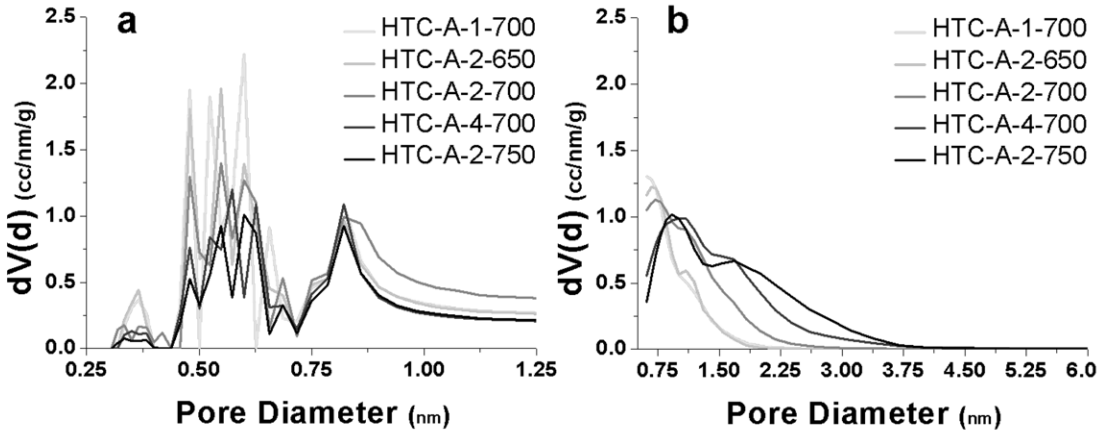


**Figure 6.11: a)** $CO_2$ NLDFT pore size distribution and b) $N_2$ adsorption QSDFT pore size distribution of ACs.

## 6.4 Summary

In the first section of this chapter, it has been shown that HTC of microalgae (*Spirulina Platensis*) is a facile, effective and sustainable method for the synthesis of

N-doped HTC carbons. The N-content of the raw microalgae was efficiently retained in the synthesised carbon products.

Direct hydrothermal treatment of raw microalgae was first tested. This synthetic route was characterised by poor yields and low N-efficiency, since most of the microalgae N-content remained in the liquid phase, as a consequence of polypeptides hydrolysis into their amino acids building blocks. The microalgae derived HTC product was characterised by a prevalent hydrocarbon character, arising from the abundant alkyl fractions derived from the fatty acids component. The addition of glucose to the initial HTC reaction mixture was found out to be extremely beneficial, because it allowed the fixation of a higher N amount in the microalgae derived HTC carbons leading to higher N-efficiency and reaction yields. These beneficial effects were attributed to the glucose double role of in-situ hydrolysis catalyst and co-condensation reaction reagent. In the former case, the formation of glucose HTC degradation products (e.g. levulinic acid and formic acid) was thought to be a crucial event, lowering the reaction mixture pH and enhancing in this way the hydrolysis of the polypeptide amide bonds. For the latter role, the presence of carbonyl functional groups, belonging to the monosaccharides and their derivatives (e.g. HMF), was fundamental, since these moieties reacted with the amino groups of the amino acids presumably via Maillard type cascade reactions, yielding stable N-containing heterocycles (e.g. pyrrole, pyridine and quaternary-N species)

In the second part of this chapter, highly microporous N-doped carbons were synthesised via KOH chemical activation of the microalgae derived HTC carbons. Although the activation process led to a major reduction of the N content, the amount of this heteroatom retained in the synthesised ACs was still considerable (2.5 – 3.9 wt%). Furthermore changing the KOH ratio or the activation temperature values allowed tuning the porosity of the ACs from totally microporous, with the highest fraction of pores in the narrow microporosity range, to partially mesoporous, with a considerable amount of pores in the small mesopores domain. These features make these materials ideal candidates for supercapacitors electrodes, since they provide extremely high surface areas for the formation of electric double-layer coupled to abundant heteroatom doping (i.e. N and O) that is necessary to obtain a pseudo-capacitance contribution.

# CHAPTER 7 – Conclusions & Outlook

In this thesis the hydrothermal carbonisation (HTC) of carbohydrate-rich (i.e. lignocellulosic biomass) and protein-rich (i.e. microalgae) raw biomass has been investigated as a synthetic route for the production of functional carbon materials. Post-synthesis processing (i.e. pyrolysis and chemical activation) has also been studied in order to improve the synthesised material properties (e.g. porosity, surface chemistry).

A detailed investigation on the HTC conversion mechanism of lignocellulosic biomass (i.e. rye straw) and its single components has been developed (i.e. cellulose, lignin) based on a comparison with glucose HTC (Chapter 3). In this latter case it was shown that HTC temperature is a powerful tool that allows tuning the chemical structure of the glucose derived HTC carbon, from a highly cross-linked furan based scaffold to a carbon core composed of polyaromatic arene-like domains. In the cellulose case, a different HTC mechanism was proposed based on the evidence that the furan rich structure could not be observed in any of the cellulose derived HTC carbons. This observation suggested that the cellulosic substrate, when treated under hydrothermal conditions, undergoes a carbonisation process comparable to pyrolysis and yielding directly a carbonaceous product with an enhanced polyaromatic character. Repeating the same experiment series with an amylose rich carbon precursor, highlighted that the furan rich carbon structure can be isolated for amylose derived HTC carbons. As a consequence, the different HTC mechanism of cellulose conversion was attributed to its water insolubility, hindering the hydrolysis of the glycosidic bond and resultant formation of glucose. These findings revealed that the HTC of cellulose under mild processing conditions (i.e. 200 $^{o}$C and 10-20 bar) does not proceed through an hydrolysis step leading to an homogeneous solution, but the heterogeneous nature of the system (i.e. suspension in water) characterises every stage of the reaction. As a consequence, templating strategies or the addition of structural directing agents are not feasible synthetic routes for the production of cellulose derived nanostructured HTC carbons, as in the case when water soluble monosaccharides are used as carbon precursor. Using two reactors in series could provide a possible solution to overcome such a problem. The first chamber processing conditions could be optimised to effectively hydrolyse the cellulosic substrate, whilst the second reactor could be used for the synthesis of HTC carbons from the

hydrolysis product (i.e. glucose). The investigation of such an experimental set-up goes beyond the aim of this thesis, however it could provide inspiration for future work.

The HTC of rye straw reflected the reactivity patterns observed for cellulose indicating the main role of the cellulosic fraction during the HTC processing of lignocellulosic biomass. However, for rye straw, higher temperatures (i.e. 220-240$^{o}$C) were necessary to fully convert the cellulose fraction to a final carbonaceous product presumably due to the presence of lignin hindering its disruption. Nonetheless the needed temperature was still considerably lower than the value employed in pyrolytic processes to convert biomass into biochar (i.e. 350 $^{o}$C), highlighting a potential advantage of HTC over pyrolysis from an energetic point of view.

The pyrolysis of glucose derived HTC carbons was investigated as post-synthesis functionalisation step (Chapter 4). It was shown that according to the adopted processing temperature the chemical structure of the HTC carbon can be tuned tailoring its properties to the end-application (e.g. Adsorption, chromatography, electrochemistry). Pyrolysis at progressively higher temperatures (i.e. 350 – 550 – 750 – 900$^{o}$C) led to the conversion of the furan rich structure, characterising the glucose derived HTC carbon (HTC Temperature = 180$^{o}$C), into highly curved aromatic pre-graphenic domains. The complete disappearance of the furan moieties was observed in the 350 – 550 $^{o}$C temperature range, leading to the release of CO and $CO_2$ volatile species as a consequence of furan ring opening and subsequent oxygen elimination. This thermal degradation process was observed to produce an increasingly more hydrophobic surface and considerable microporosity (i.e. 0.2 $cm^3/g$), within the HTC carbon structure. Both features are indeed key material properties to take into consideration, when considering the use of HTC carbon for any applications.

A comparison between HTC carbons and chars obtained from direct pyrolysis of carbohydrates (i.e. glucose and starch), was also developed based on an NMR semiquantitative analysis. Its findings have highlighted that hydrothermal treatment of glucose (or hydrolysable glucose polymer at the employed HTC processing conditions) offers an additional intermediate stage (i.e. the furan rich intermediate) between the parent sugar and the polyaromatic char structure, obtained from pyrolysis, allowing a higher degree of control over the chemical structure of the synthesised HTC carbons. Furthermore increasing the HTC temperature (i.e. 200-280

$^{o}$C) led to an increase of aromatisation comparable to the one obtained from pyrolysis (i.e. > 350 $^{o}$C). As a consequence, with the aid of a high temperature and pressure equipment, it would be possible to synthesise and tune the chemical structure of HTC carbons, as shown with pyrolysis, in a single pot synthetic process. This would certainly be advantageous from a process engineering point of view.

In order to produce HTC carbons derived from lignocellulosic biomass with enhanced textural and porous properties, KOH chemical activation was also investigated as an HTC post-synthesis functionalisation step (Chapter 5). Regardless of the parent biomass (i.e. glucose, cellulose or rye straw), HTC carbons demonstrated to be excellent precursors for the synthesis of highly microporous ACs. The porosity development upon KOH chemical activation was found to be dependent on the chemical structure of the HTC carbon precursors, tuned by employing different HTC temperatures. HTC carbons synthesised at higher temperatures (i.e. HTC temperature = 280 $^{o}$C) generated ACs characterised by a lower porosity development, but with a narrower PSD mostly composed of micropores. On the other hand, KOH chemical activation of HTC carbons, synthesised at lower temperatures (i.e. HTC temperature = 180 - 240$^{o}$C), produced ACs with higher total pore volume and broader PSDs, characterised by a significant mesopores fraction. Overall, the extent of porosity development control, allowed by HTC temperature, was found to be comparable to the one obtained by using different KOH to carbon precursor mass ratios (i.e. one of the main KOH activation process variables). As a consequence in the context of HTC carbons derived ACs, the HTC temperature was discovered to be a key variable for the tuning of the ACs porosity.

The HTC carbons derived ACs were also tested for both $CO_2$ capture or high pressure $CH_4$ storage. The obtained preliminary results were very promising showing that the measured uptakes of both adsorbates (i.e. $CO_2$ and $CH_4$) were comparable to top-performing and commercially available adsorbents, usually employed for these end-applications. Further performance improvements could be certainly achieved by tailoring the PSD of the ACs to the adsorbate, via tuning of the HTC carbon synthesis and KOH chemical activation parameters (e.g. HTC temperature, KOH ratio, activation temperature). Although these optimisation studies were beyond the scope of this work, they could provide inspiration for further developments in this research field.

In the last results chapter of this thesis (Chapter 6) the use of HTC as a facile, effective and sustainable synthetic route for microalgae derived N-doped carbons was shown. The hydrothermal treatment of the microalgae substrate was observed to cause the depletion of the protein and carbohydrate fractions and the near complete loss (i.e. ≈ 90%) of the microalgae N-content, as liquid hydrolysis/degradation products. The carbonaceous product, obtained from microalgae HTC, showed a predominantly aliphatic character indicating the presence of alkyl chains presumably derived from the lipid fraction. The increasingly pitch-like texture, observed at higher HTC temperatures, confirmed that the microalgae HTC product contained a large fraction of heavy hydrocarbons. Addition of glucose to the initial HTC reaction mixture was found out to be extremely beneficial, because it allowed the fixation of a higher N amount, in the algae derived HTC carbons (≈ 60 %), and the attainment of higher product yields (≈ 50%). Both positive effects were attributed to the glucose double role of in-situ hydrolysis catalyst and co-condensation reaction reagent. In the former case, the formation of glucose HTC degradation products (e.g. levulinic acid and formic acid) was thought to be a crucial event, lowering the reaction mixture pH and enhancing in this way the hydrolysis of the polypeptide amide bonds. For the latter role, the presence of carbonyl functional groups, belonging to the monosaccharides and their derivatives (e.g. 5-HMF), was fundamental, since these moieties reacted with the amino groups of the amino acids, presumably via Maillard type cascade reactions yielding stable N-containing heterocycles (e.g. pyrrole, pyridine and quaternary-N species). Chemical activation of the microalgae derived HTC produced highly microporous N-doped carbons. Although the activation process led to a major reduction of the N content, the amount of this heteroatom, retained in the synthesised ACs, was still notable (2.5 – 3.9 wt%). Furthermore the porosity development (i.e. micropore volume, PSD and surface area) could be tuned from totally microporous, with the highest fraction of pores in the narrow microporosity range (< 1nm), to partially mesoporous, with a considerable amount of pores in the small mesopores domain (2-3.5 nm). These features render these materials ideal candidates for electrochemical double layer supercapacitors electrodes, since they present extremely high surface area coupled to abundant heteroatom doping (i.e. N and O) that is necessary to obtain a pseudo-capacitance contribution.

Overall, the work presented in this thesis represents remarkable progresses towards the exploitation of raw biomass for the synthesis of sustainable and functional carbon materials. It highlights the high potential of the hydrothermal method as a means of conversion of waste or cheap biomass into value added products in complete agreement with the "Biorefinery Concept". Furthermore it represents an important contribution to the overall HTC research field, since it proposes a new reaction mechanism for cellulose HTC conversion and it presents a detailed investigation of HTC carbon pyrolysis, which can be used as a further post-synthesis functionalisation step. It also demonstrates the high suitability of HTC carbons as precursors for the synthesis of highly microporous ACs having several foreseeable applications (e.g. $CO_2$ capture, high pressure $CH_4$ storage and supercapacitors) and representing a carbon neutral/negative alternative to the fossil fuels derived carbon materials.

## References


[1] F. Cherubini, *Energy Conversion and Management* **2010**, *51*, 1412.
[2] R. Rinaldi, F. Schuth, *Energy & Environmental Science* **2009**, *2*, 610.
[3] R. W. Bentley, *Energy Policy* **2002**, *30*, 189.
[4] C. Okkerse, H. van Bekkum, *Green Chemistry* **1999**, *1*, 107.
[5] IEA, *Task 42 on biorefineries: co-production of fuels, chemicals, power and materials from biomass.*, http://www.biorefinery.nl/ieabioenergy-task42/, **2008**, accessed 01/12/2011
[6] A. J. Ragauskas, C. K. Williams, B. H. Davison, G. Britovsek, J. Cairney, C. A. Eckert, W. J. Frederick, J. P. Hallett, D. J. Leak, C. L. Liotta, J. R. Mielenz, R. Murphy, R. Templer, T. Tschaplinski, *Science* **2006**, *311*, 484.
[7] P. T. Anastas, M. M. Kirchhoff, *Accounts of Chemical Research* **2002**, *35*, 686.
[8] P. Anastas, N. Eghbali, *Chemical Society Reviews* **2010**, *39*, 301.
[9] J. H. Clark, F. E. I. Deswarte, T. J. Farmer, *Biofuels Bioproducts & Biorefining-Biofpr* **2009**, *3*, 72.
[10] Y. P. Zhai, Y. Q. Dou, D. Y. Zhao, P. F. Fulvio, R. T. Mayes, S. Dai, *Advanced Materials* **2011**, *23*, 4828.
[11] J. P. Paraknowitsch, A. Thomas, M. Antonietti, *Chemistry of Materials* **2009**, *21*, 1170.
[12] F. Rodriguez-Reinoso, *Carbon* **1998**, *36*, 159.
[13] K. A. Spokas, D. C. Reicosky, *Ann. Environ. Sci.* **2009**, *3*, 179.
[14] A. G. Pandolfo, A. F. Hollenkamp, *Journal of Power Sources* **2006**, *157*, 11.
[15] A. Eftekhari, P. Jafarkhani, F. Moztarzadeh, *Carbon* **2006**, *44*, 1343.
[16] A. Thess, R. Lee, P. Nikolaev, H. J. Dai, P. Petit, J. Robert, C. H. Xu, Y. H. Lee, S. G. Kim, A. G. Rinzler, D. T. Colbert, G. E. Scuseria, D. Tomanek, J. E. Fischer, R. E. Smalley, *Science* **1996**, *273*, 483.
[17] A. Szczurek, G. Amaral-Labat, V. Fierro, A. Pizzi, E. Masson, A. Celzard, *Carbon* **2011**, *49*, 2773.
[18] A. Szczurek, G. Amaral-Labat, V. Fierro, A. Pizzi, A. Celzard, *Carbon* **2011**, *49*, 2785.
[19] E. Raymundo-Pinero, F. Leroux, F. Beguin, *Advanced Materials* **2006**, *18*, 1877.
[20] J. Jeromenok, W. Böhlmann, M. Antonietti, J. Weber, *Macromolecular Rapid Communications* **2011**, *32*, 1846.
[21] R. J. White, V. Budarin, R. Luque, J. H. Clark, D. J. Macquarrie, *Chemical Society Reviews* **2009**, *38*, 3401.
[22] R. J. White, V. L. Budarin, J. H. Clark, *Chemsuschem* **2008**, *1*, 408.
[23] M. M. Titirici, A. Thomas, M. Antonietti, *New Journal of Chemistry* **2007**, *31*, 787.
[24] M. M. Titirici, A. Thomas, S. H. Yu, J. O. Muller, M. Antonietti, *Chemistry of Materials* **2007**, *19*, 4205.
[25] F. Bergius, *Naturwissenschaften* **1928**, *16*, 1.
[26] O. Bobleter, G. Bonn, *Carbohydrate Research* **1983**, *124*, 185.
[27] G. Bonn, O. Bobleter, *Journal of Radioanalytical Chemistry* **1983**, *79*, 171.
[28] Vattenfall, *Research and Development Magazine*, http://www.vattenfall.com/en/file/Biomass_RDMagazine_4_dec_2010.pdf_16610923.pdf, **2010**, accessed 03/12/2011

[29] N. D. Berge, K. S. Ro, J. D. Mao, J. R. V. Flora, M. A. Chappell, S. Y. Bae, *Environmental Science & Technology* **2011**, *45*, 5696.
[30] M. C. Rillig, M. Wagner, M. Salem, P. M. Antunes, C. George, H. G. Ramke, M. M. Titirici, M. Antonietti, *Applied Soil Ecology* **2010**, *45*, 238.
[31] W. Qing, L. Hong, C. Liquan, H. Xuejie, *Carbon* **2001**, *39*, 2211.
[32] M. M. Titirici, M. Antonietti, *Chemical Society Reviews* **2010**, *39*, 103.
[33] B. Hu, K. Wang, L. H. Wu, S. H. Yu, M. Antonietti, M. M. Titirici, *Advanced Materials* **2010**, *22*, 813.
[34] M. M. Titirici, M. Antonietti, N. Baccile, *Green Chemistry* **2008**, *10*, 1204.
[35] N. Baccile, G. Laurent, F. Babonneau, F. Fayon, M. M. Titirici, M. Antonietti, *Journal of Physical Chemistry C* **2009**, *113*, 9644.
[36] S. Kubo, R. J. White, N. Yoshizawa, M. Antonietti, M.-M. Titirici, *Chemistry of Materials* **2011**, *23*, 4882.
[37] R. J. White, N. Yoshizawa, M. Antonietti, M. M. Titirici, *Green Chemistry* **2011**, *13*, 2428.
[38] M. Antonietti, M. M. Titirici, *Comptes Rendus Chimie* **2010**, *13*, 167.
[39] L. Delarosa, M. Pruski, D. Lang, B. Gerstein, P. Solomon, *Energy & Fuels* **1992**, *6*, 460.
[40] P. F. Barron, M. A. Wilson, *Nature* **1981**, *289*, 275.
[41] P. Tekely, D. Nicole, J. Brondeau, J. J. Delpuech, *Journal of Physical Chemistry* **1986**, *90*, 5608.
[42] I. Pastorova, R. E. Botto, P. W. Arisz, J. J. Boon, *Carbohydrate Research* **1994**, *262*, 27.
[43] J. B. Wooten, J. I. Seeman, M. R. Hajaligol, *Energy & Fuels* **2004**, *18*, 1.
[44] K. Saito, K. Kanehashi, I. Komaki, in *Annual Reports on NMR Spectroscopy, Vol. Volume 44*, Academic Press, **2001**, pp. 23.
[45] J. Herzfeld, D. Rand, Y. Matsuki, E. Daviso, M. Mak-Jurkauskas, I. Mamajanov, *Journal of Physical Chemistry B* **2011**, *115*, 5741.
[46] X. L. Wu, S. T. Burns, K. W. Zilm, *Journal of Magnetic Resonance Series A* **1994**, *111*, 29.
[47] M. Levitt, *Spin Dynamics: Basics of Nuclear Magnetic Resonance*, 2nd ed., Wiley, **2008**.
[48] M. Balci, *Basic 1H- and 13C-NMR Spectroscopy*, Elsevier, **2005**.
[49] E. D. Becker, *High Resolution NMR: Theory and Chemical Applications*, 3rd ed., Academic Press, **2000**.
[50] N. Baccile, in *Ideas in Chemistry and Molecular Sciences*, Wiley-VCH Verlag GmbH & Co. KGaA, **2010**, pp. 139.
[51] D. D. Laws, H. M. L. Bitter, A. Jerschow, *Angewandte Chemie-International Edition* **2002**, *41*, 3096.
[52] J. P. Hornak, *http://www.cis.rit.edu/htbooks/mri/chap-3/chap-3.htm*, accessed 30/09/2011.
[53] P. F. Barron, M. A. Wilson, J. F. Stephens, B. A. Cornell, K. R. Tate, *Nature* **1980**, *286*, 585.
[54] D. G. Cory, *Chemical Physics Letters* **1988**, *152*, 431.
[55] R. Tycko, G. Dabbagh, *Journal of the American Chemical Society* **1991**, *113*, 9444.
[56] R. Benn, H. Grondey, C. Brevard, A. Pagelot, *Journal of the Chemical Society-Chemical Communications* **1988**, 102.

[57] M. J. Bayro, M. Huber, R. Ramachandran, T. C. Davenport, B. H. Meier, M. Ernst, R. G. Griffin, *Journal of Chemical Physics* **2009**, *130*, 8.
[58] A. Gandini, M. N. Belgacem, *Progress in Polymer Science* **1997**, *22*, 1203.
[59] M. Choura, N. M. Belgacem, A. Gandini, *Macromolecules* **1996**, *29*, 3839.
[60] S. K. R. Patil, C. R. F. Lund, *Energy & Fuels* **2011**, *25*, 4745.
[61] J. Horvat, B. Klaic, B. Metelko, V. Sunjic, *Tetrahedron Letters* **1985**, *26*, 2111.
[62] L. Wang, M. Sharifzadeh, R. Templer, R. J. Murphy, *Energy & Environmental Science* **2011**, DOI: 10.1039/C2EE02935A.
[63] R. Palkovits, K. Tajvidi, J. Procelewska, R. Rinaldi, A. Ruppert, *Green Chemistry* **2010**, *12*, 972.
[64] R. Rinaldi, R. Palkovits, F. Schuth, *Angewandte Chemie-International Edition* **2008**, *47*, 8047.
[65] University_of_Kentucky, *Cereal Straw Production*, http://www.uky.edu/Ag/CDBREC/introsheets/straw.pdf, **2009**, accessed 10/11/2011
[66] FAO, http://www.fao.org/es/ess/top/commodity.html?lang=en&item=71&year=2005, accessed 10/10/2011.
[67] R. D. Gilbert, J. F. Kadla, in *Biopolymers from Renewable Resources* (Ed.: D. L. Kaplan), Springer, Berlin, **1998**, pp. 47.
[68] G. S. Nilsson, K. E. Bergquist, U. Nilsson, L. Gorton, *Starch-Starke* **1996**, *48*, 352.
[69] S. Deguchi, K. Tsujii, K. Horikoshi, *Chemical Communications* **2006**, 3293.
[70] R. Rinaldi, N. Meine, J. vom Stein, R. Palkovits, F. Schuth, *Chemsuschem* **2010**, *3*, 266.
[71] B. Lindman, G. Karlstrom, L. Stigsson, *Journal of Molecular Liquids* **2010**, *156*, 76.
[72] ChemEd-DL, http://chempaths.chemeddl.org/services/chempaths/?q=book/General%20Chemistry%20Textbook/Molecules%20in%20Living%20Systems/1556/building-blocks-biochemistry&title=CoreChem:Polysaccharides, accessed 10/11/2011.
[73] J. Ralph, C. Lapierre, J. M. Marita, H. Kim, F. C. Lu, R. D. Hatfield, S. Ralph, C. Chapple, R. Franke, M. R. Hemm, J. Van Doorsselaere, R. R. Sederoff, D. M. O'Malley, J. T. Scott, J. J. MacKay, N. Yahiaoui, A. M. Boudet, M. Pean, G. Pilate, L. Jouanin, W. Boerjan, *Phytochemistry* **2001**, *57*, 993.
[74] G. Brunner, *The Journal of Supercritical Fluids* **2009**, *47*, 373.
[75] A. Kruse, E. Dinjus, *Journal of Supercritical Fluids* **2007**, *39*, 362.
[76] A. Kruse, E. Dinjus, *Journal of Supercritical Fluids* **2007**, *41*, 361.
[77] X. Sun, Y. Li, *Angewandte Chemie International Edition* **2004**, *43*, 597.
[78] R. Rinaldi, F. Schuth, *Chemsuschem* **2009**, *2*, 1096.
[79] A. Kruse, A. Gawlik, *Industrial & Engineering Chemistry Research* **2003**, *42*, 267.
[80] M. Moller, P. Nilges, F. Harnisch, U. Schroder, *Chemsuschem* **2011**, *4*, 566.
[81] T. Rogalinski, T. Ingram, G. Brunner, *Journal of Supercritical Fluids* **2008**, *47*, 54.
[82] P. Mansikkamaki, M. Lahtinen, K. Rissanen, *Carbohydrate Polymers* **2007**, *68*, 35.

[83] W. S. L. Mok, M. J. Antal, *Industrial & Engineering Chemistry Research* **1992**, *31*, 1157.
[84] P. Kumar, D. M. Barrett, M. J. Delwiche, P. Stroeve, *Industrial & Engineering Chemistry Research* **2009**, *48*, 3713.
[85] S. Link, S. Arvelakis, H. Spliethoff, P. De Waard, A. Samoson, *Energy & Fuels* **2008**, *22*, 3523.
[86] D. Knezevic, W. van Swaaij, S. Kersten, *Industrial & Engineering Chemistry Research* **2010**, *49*, 104.
[87] E. B. Sanders, A. I. Goldsmith, J. I. Seeman, *Journal of Analytical and Applied Pyrolysis* **2003**, *66*, 29.
[88] M. Bardet, S. Hediger, G. Gerbaud, S. Gambarelli, J. F. Jacquot, M. F. Foray, A. Gadelle, *Fuel* **2007**, *86*, 1966.
[89] K. David, Y. Q. Pu, M. Foston, J. Muzzy, A. Ragauskas, *Energy & Fuels* **2009**, *23*, 498.
[90] C. Liu, J. B. Huang, X. L. Huang, H. J. Li, Z. Zhang, *Computational and Theoretical Chemistry* **2011**, *964*, 207.
[91] N. S. Mosier, C. M. Ladisch, M. R. Ladisch, *Biotechnology and Bioengineering* **2002**, *79*, 610.
[92] J. F. Haw, T. P. Schultz, *Holzforschung* **1985**, *39*, 289.
[93] R. J. White, C. Antonio, V. L. Budarin, E. Bergstrom, J. Thomas-Oates, J. H. Clark, *Advanced Functional Materials* **2010**, *20*, 1834.
[94] A. Oberlin, in *Chemistry and Physics of Carbon* (Ed.: P. A. Thrower), Marcel Dekker Inc., **1989**, pp. 1.
[95] J. N. Rouzaud, A. Oberlin, *Carbon* **1989**, *27*, 517.
[96] R. E. Franklin, *Proceedings of the Royal Society of London Series a-Mathematical and Physical Sciences* **1951**, *209*, 196.
[97] R. E. Franklin, *Acta Crystallographica* **1951**, *4*, 253.
[98] A. Oya, H. Marsh, *Journal of Materials Science* **1982**, *17*, 309.
[99] C. X. Tong, *Advanced Materials for Thermal Management of Electronic Packaging*, 1st ed., Springer, New York, **2011**.
[100] P. J. F. Harris, S. C. Tsang, *Philosophical Magazine a-Physics of Condensed Matter Structure Defects and Mechanical Properties* **1997**, *76*, 667.
[101] M. Inagaki, L. R. Radovic, *Carbon* **2002**, *40*, 2279.
[102] J. C. C. Freitas, F. G. Emmerich, G. R. C. Cernicchiaro, L. C. Sampaio, T. J. Bonagamba, *Solid State Nuclear Magnetic Resonance* **2001**, *20*, 61.
[103] C. L. Burket, R. Rajagopalan, A. P. Marencic, K. Dronvajjala, H. C. Foley, *Carbon* **2006**, *44*, 2957.
[104] X. Q. Zhang, J. Golding, I. Burgar, *Polymer* **2002**, *43*, 5791.
[105] E. Fitzer, W. Schafer, *Carbon* **1970**, *8*, 353.
[106] X. Q. Zhang, D. H. Solomon, *Chemistry of Materials* **1999**, *11*, 384.
[107] H. Eckert, Y. A. Levendis, R. C. Flagan, *Journal of Physical Chemistry* **1988**, *92*, 5011.
[108] A. Shindo, K. Izumino, *Carbon* **1994**, *32*, 1233.
[109] S. Biniak, G. Szymanski, J. Siedlewski, A. Swiatkowski, *Carbon* **1997**, *35*, 1799.
[110] Aldrich_Chemical_Company_Inc., *Catalogue Handbook of Fine Chemicals* Aldrich_Chemical_Company_Inc, **1990**.

[111] NIST, http://webbook.nist.gov/cgi/cbook.cgi?ID=C123762&Mask=200#Mass-Spec, accessed 25/10/2011.
[112] S. B. Sastri, J. P. Armistead, T. M. Keller, *Carbon* **1993**, *31*, 617.
[113] K. A. Trick, T. E. Saliba, *Carbon* **1995**, *33*, 1509.
[114] A. Thomas, F. Goettmann, M. Antonietti, *Chemistry of Materials* **2008**, *20*, 738.
[115] H. Marsh, W. F. K. Wynnejones, *Carbon* **1964**, *1*, 269.
[116] J. C. C. Freitas, T. J. Bonagamba, F. G. Emmerich, *Energy & Fuels* **1999**, *13*, 53.
[117] S. Kubo, I. Tan, R. J. White, M. Antonietti, M. M. Titirici, *Chemistry of Materials* **2010**, *22*, 6590.
[118] S. Kubo, R. Demir-Cakan, L. Zhao, R. J. White, M. M. Titirici, *Chemsuschem* **2010**, *3*, 188.
[119] R. J. White, K. Tauer, M. Antonietti, M. M. Titirici, *Journal of the American Chemical Society* **2010**, *132*, 17360.
[120] L. Khezami, A. Chetouani, B. Taouk, R. Capart, *Powder Technology* **2005**, *157*, 48.
[121] A. H. Basta, V. Fierro, H. El-Saied, A. Celzard, *Bioresource Technology* **2009**, *100*, 3941.
[122] A. Linares-Solano, D. Lozano-Castello, M. A. Lillo-Rodenas, D. Cazorla-Amoros, in *Chemistry and Physics of Carbon, Vol. 30* (Ed.: L. R. Radovic), CRC **2007**, pp. 1.
[123] M. Sevilla, R. Mokaya, *Journal of Materials Chemistry* **2011**, *21*, 4727.
[124] Y. Gogotsi, C. Portet, S. Osswald, J. M. Simmons, T. Yidirim, G. Laudisio, J. E. Fischer, *International Journal of Hydrogen Energy* **2009**, *34*, 6314.
[125] H. Marsh, F. Rodriguez-Reinoso, Elsevier, Oxford, **2006**.
[126] D. Lozano-Castello, J. M. Calo, D. Cazorla-Amoros, A. Linares-Solano, *Carbon* **2007**, *45*, 2529.
[127] M. A. Lillo-Rodenas, D. Cazorla-Amoros, A. Linares-Solano, *Carbon* **2003**, *41*, 267.
[128] M. A. Lillo-Rodenas, J. Juan-Juan, D. Cazorla-Amoros, A. Linares-Solano, *Carbon* **2004**, *42*, 1371.
[129] D. Lozano-Castello, M. A. Lillo-Rodenas, D. Cazorla-Amoros, A. Linares-Solano, *Carbon* **2001**, *39*, 741.
[130] M. A. Lillo-Rodenas, D. Lozano-Castello, D. Cazorla-Amoros, A. Linares-Solano, *Carbon* **2001**, *39*, 751.
[131] F. Rouquerol, J. Rouquerol, K. Sing, *ADSORPTION By Powders & Porous Solids*, Academic Press, **1999**.
[132] D. Lozano-Castello, D. Cazorla-Amoros, A. Linares-Solano, *Carbon* **2004**, *42*, 1233.
[133] D. H. Everett, *Definitions, Terminology and Symbols in Colloid and Surface Chemistry - Part I, Vol. 31*, IUPAC, **1972**.
[134] J. Garrido, A. Linaressolano, J. M. Martinmartinez, M. Molinasabio, F. Rodriguezreinoso, R. Torregrosa, *Langmuir* **1987**, *3*, 76.
[135] J. Weber, J. Schmidt, A. Thomas, W. Bohlmann, *Langmuir* **2010**, *26*, 15650.
[136] J. Silvestre-Albero, A. Silvestre-Albero, F. Rodriguez-Reinoso, M. Thommes, *Carbon* **2011**.

[137] K. S. Walton, R. Q. Snurr, *Journal of the American Chemical Society* **2007**, *129*, 8552.
[138] F. Carrasco-Marin, M. V. Lopez-Ramon, C. Moreno-Castilla, *Langmuir* **1993**, *9*, 2758.
[139] A. Linares-Solano, D. Lozano-Castello, M. A. Lillo-Rodenas, D. Cazorla-Amoros, in *Recent Advances in Adsorption Processes for Environmental Protection and Security*, Springer, Dordrecht, **2008**, pp. 97.
[140] M. Kruk, M. Jaroniec, J. Choma, *Carbon* **1998**, *36*, 1447.
[141] A. V. Neimark, Y. Z. Lin, P. I. Ravikovitch, M. Thommes, *Carbon* **2009**, *47*, 1617.
[142] J. L. Figueiredo, M. F. R. Pereira, M. M. A. Freitas, J. J. M. Orfao, *Carbon* **1999**, *37*, 1379.
[143] A. Wahby, J. M. Ramos-Fernandez, M. Martinez-Escandell, A. Sepulveda-Escribano, J. Silvestre-Albero, F. Rodriguez-Reinoso, *Chemsuschem* **2010**, *3*, 974.
[144] S. Sircar, T. C. Golden, M. B. Rao, *Carbon* **1996**, *34*, 1.
[145] J. Silvestre-Albero, A. Wahby, A. Sepulveda-Escribano, M. Martinez-Escandell, K. Kaneko, F. Rodriguez-Reinoso, *Chemical Communications* **2011**, *47*, 6840.
[146] R. Banerjee, H. Furukawa, D. Britt, C. Knobler, M. O'Keeffe, O. M. Yaghi, *Journal of the American Chemical Society* **2009**, *131*, 3875.
[147] R. Dawson, E. Stockel, J. R. Holst, D. J. Adams, A. I. Cooper, *Energy & Environmental Science* **2011**, *4*, 4239.
[148] M. G. Rabbani, H. M. El-Kaderi, *Chemistry of Materials* **2011**, *23*, 1650.
[149] T. Tozawa, J. T. A. Jones, S. I. Swamy, S. Jiang, D. J. Adams, S. Shakespeare, R. Clowes, D. Bradshaw, T. Hasell, S. Y. Chong, C. Tang, S. Thompson, J. Parker, A. Trewin, J. Bacsa, A. M. Z. Slawin, A. Steiner, A. I. Cooper, *Nature Materials* **2009**, *8*, 973.
[150] J. S. Lee, J. H. Kim, J. T. Kim, J. K. Suh, J. M. Lee, C. H. Lee, *Journal of Chemical and Engineering Data* **2002**, *47*, 1237.
[151] R. Banerjee, A. Phan, B. Wang, C. Knobler, H. Furukawa, M. O'Keeffe, O. M. Yaghi, *Science* **2008**, *319*, 939.
[152] H. Furukawa, O. M. Yaghi, *Journal of the American Chemical Society* **2009**, *131*, 8875.
[153] J. W. Lee, M. S. Balathanigaimani, H. C. Kang, W. G. Shim, C. Kim, H. Moon, *Journal of Chemical and Engineering Data* **2007**, *52*, 66.
[154] J. Sun, T. D. Jarvi, L. F. Conopask, S. Satyapal, M. J. Rood, M. Rostam-Abadi, *Energy & Fuels* **2001**, *15*, 1241.
[155] D. F. Quinn, J. A. MacDonald, K. Sosin, *207th ACS National Meeting San Diego* **1994**.
[156] D. Lozano-Castello, J. Alcaniz-Monge, M. A. de la Casa-Lillo, D. Cazorla-Amoros, A. Linares-Solano, *Fuel* **2002**, *81*, 1777.
[157] C. D. Wood, B. Tan, A. Trewin, F. Su, M. J. Rosseinsky, D. Bradshaw, Y. Sun, L. Zhou, A. I. Cooper, *Advanced Materials* **2008**, *20*, 1916.
[158] W. Zhou, *Chemical Record* **2010**, *10*, 200.
[159] J. P. Paraknowitsch, A. Thomas, M. Antonietti, *Journal of Materials Chemistry* **2010**, *20*, 6746.
[160] M. Terrones, P. M. Ajayan, F. Banhart, X. Blase, D. L. Carroll, J. C. Charlier, R. Czerw, B. Foley, N. Grobert, R. Kamalakaran, P. Kohler-Redlich, M. Ruhle,

T. Seeger, H. Terrones, *Applied Physics a-Materials Science & Processing* **2002**, *74*, 355.
[161] Q. H. Yang, W. H. Xu, A. Tomita, T. Kyotani, *Chemistry of Materials* **2005**, *17*, 2940.
[162] W. Yang, T. P. Fellinger, M. Antonietti, *Journal of the American Chemical Society* **2011**, *133*, 206.
[163] G. Lota, E. Frackowiak, *Fuel Cells* **2010**, *10*, 848.
[164] L. Zhao, Y.-S. Hu, H. Li, Z. Wang, L. Chen, *Advanced Materials* **2011**, *23*, 1385.
[165] G. P. Hao, W. C. Li, D. Qian, A. H. Lu, *Advanced Materials* **2010**, *22*, 853.
[166] M. Sevilla, P. Valle-Vigón, A. B. Fuertes, *Advanced Functional Materials* **2011**, *21*, 2781.
[167] C. Pevida, T. C. Drage, C. E. Snape, *Carbon* **2008**, *46*, 1464.
[168] M. G. Plaza, S. Garcia, F. Rubiera, J. J. Pis, C. Pevida, *Separation and Purification Technology* **2011**, *80*, 96.
[169] L. Zhao, N. Baccile, S. Gross, Z. Yuanjian, W. Wei, S. Yuhan, M. Antonietti, M. M. Titirici, *Carbon* **2010**, *48*, 3778.
[170] R. J. White, M. Antonietti, M. M. Titirici, *Journal of Materials Chemistry* **2009**, *19*, 8645.
[171] L. Zhao, R. Crombez, F. P. Caballero, M. Antonietti, J. Texter, M. M. Titirici, *Polymer* **2010**, *51*, 4540.
[172] A. Demirbas, M. F. Demirbas, *Energy Conversion and Management* **2011**, *52*, 163.
[173] M. Aresta, A. Dibenedetto, G. Barberio, *Fuel Processing Technology* **2005**, *86*, 1679.
[174] Y. Chisti, *Trends in Biotechnology* **2008**, *26*, 126.
[175] H. Knicker, H. D. Ludemann, *Organic Geochemistry* **1995**, *23*, 329.
[176] H. Knicker, A. W. Scaroni, P. G. Hatcher, *Organic Geochemistry* **1996**, *24*, 661.
[177] X. Zang, R. T. Nguyen, H. R. Harvey, H. Knicker, P. G. Hatcher, *Geochimica Et Cosmochimica Acta* **2001**, *65*, 3299.
[178] N. Baccile, G. Laurent, C. Coelho, F. Babonneau, L. Zhao, M. M. Titirici, *Journal of Physical Chemistry C* **2011**, *115*, 8976.
[179] M. S. Solum, K. L. Altmann, M. Strohmeier, D. A. Berges, Y. L. Zhang, J. C. Facelli, R. J. Pugmire, D. M. Grant, *Journal of the American Chemical Society* **1997**, *119*, 9804.
[180] A. Adams, K. A. Tehrani, M. Kersiene, R. Venskutonis, N. De Kimpe, *Journal of Agricultural and Food Chemistry* **2003**, *51*, 4338.
[181] Y. F. Jia, B. Xiao, K. M. Thomas, *Langmuir* **2002**, *18*, 470.
[182] A. C. Lua, T. Yang, *Journal of Colloid and Interface Science* **2004**, *276*, 364.
[183] S. R. Kelemen, M. Afeworki, M. L. Gorbaty, P. J. Kwiatek, M. S. Solum, J. Z. Hu, R. J. Pugmire, *Energy & Fuels* **2002**, *16*, 1507.
[184] K. Stanczyk, R. Dziembaj, Z. Piwowarska, S. Witkowski, *Carbon* **1995**, *33*, 1383.
[185] M. Sevilla, R. Mokaya, A. B. Fuertes, *Energy & Environmental Science* **2011**, *4*, 2930.
[186] E. Raymundo-Pinero, D. Cazorla-Amoros, A. Linares-Solano, J. Find, U. Wild, R. Schlogl, *Carbon* **2002**, *40*, 597.

[187] J. R. Pels, F. Kapteijn, J. A. Moulijn, Q. Zhu, K. M. Thomas, *Carbon* **1995**, *33*, 1641.

# List of Abbreviations and Symbols

## Abbreviations

| | |
|---|---|
| 5-HMF | 5-hydroxymethylfurfural |
| AC(s) | Activated Carbon(s) |
| BET | Brunauer, Emmet, Teller |
| CP | Cross Polarisation |
| CSA | Chemical Shift Anisotropy |
| DC | Dipolar Coupling |
| (NL-QS)DFT | (Non Local – Quenched State) Density Functional Theory |
| DLS | Dynamic Light Scattering |
| DQ-SQ | Double Quantum Single Quantum |
| DR | Dubinin-Radushkevich |
| EA | Elemental Analysis |
| FID | Free Induction Decay |
| FT | Fourier Transform |
| FT-IR | Fourier Transform Infrared Spectroscopy |
| GC-MS | Gas Chromatography – Mass Spectrometry |
| HETCOR | Heteronuclear Correlation Experiment |
| HeteroC | Heteronuclear Dipolar Coupling |
| HeteroD | Heteronuclear Dicoupling |
| HomoC | Homonuclear Dipolar Coupling |
| HomoD | Homonuclear Dicoupling |
| HTC | Hydrothermal Carbonisation |
| INEPT | Insensitive Nuclei Enhanced by Polarisation Transfer |
| IRCP | Inversion Recovery Cross Polarisation |
| J-C | J-Coupling |
| KOH Ratio | KOH to Carbon Precursor Mass Ratio |
| MAS | Magic Angle Spinning |
| PFA | Polyfurfuryl Alcohol |
| PSD | Pore Size Distribution |
| RF | Radiofrequency |
| SEM | Scanning electron microscopy |
| SP | Single Pulse |

| | |
|---|---|
| ssNMR | Solid State Nuclear Magnetic Resonance |
| (HR)TEM | (High Resolution) Transmission Electron Microscopy |
| TGA | Thermogravimetric Analysis |
| TG-IR | Thermogravimetric Analysis – Infrared Spectroscopy |
| XPS | X-ray Photoelectron spectroscopy |
| XRD | X-ray Diffraction |

## Symbols

| | |
|---|---|
| $J$ | Spin angular momentum |
| $\hbar$ | Planck's Constant divided by $2\pi$ |
| $I$ | Nuclear Spin |
| $\mu$ | Magnetic Moment |
| $\gamma$ | Gyromagnetic Constant |
| $B_0$ | Primary (External) Magnetic Field |
| $B_1$ | Secondary Magnetic Field |
| $\omega_0$ | Larmor Frequency |
| $B_{ef}$ | Effective Magnetic Field |
| $\sigma$ | Shielding Factor |
| $t_{cp}$ | Cross Polarisation Contact Time |
| $\delta$ | NMR Chemical Shift |
| $r$ | Furan to Arene Estimate |
| $S_{BET}$ | BET Surface Area |
| $P/P_0$ | Relative Pressure |
| $V_{CO2\text{-}NLDFT}$ | Pore Volume calculated from $CO_2$ isotherm with NLDFT model |
| $V_{CO2\text{-}DR}$ | Pore Volume calculated from $CO_2$ isotherm with DR model |
| $V_{N2\text{-}DR}$ | Pore Volume calculated from $N_2$ isotherm with DR model |
| $V_{N2\text{-}EX}$ | Pore Volume obtained from $N_2$ isotherm |

# Appendix

## Instrumental details

### Scanning Electron Microscopy (SEM)

SEM was performed using a Gemini Leo-1550 instrument. Before imaging, material was loaded onto carbon tapes and sputtered with Au.

### Dynamic Light Scattering (DLS)

Solutions were investigated by dynamic light scattering (DLS) using ALV-7004 Multiple Tau Digital Correlator equipped with CGS-3 Compact Goniometer system, 22 mW He-Ne laser (wavelength l = 632.8 nm) and a pair of avalanche photodiodes operated in a pseudo-cross-correlation mode. All published measurements were made at a 90◦ angle.

### Elemental Analysis (EA)

Elemental chemical analysis was performed on a (C, N, O, S, H) Vario Elmer-Perkin elemental analyzer by Ms. Silvia Pirok (Max Planck Institute of Colloids and Interfaces, Golm, Germany).

### Fourier Transform – Infrared Spectroscopy (FT-IR)

FT-IR spectra were recorded with a Varian 1000 FT-IR (scimitar series) spectrometer, equipped with an attenuated total reflection (ATR) setup.

### X-ray Diffraction (XRD)

XRD patterns were recorded with a Bruker-D8 apparatus (θ-θ reflection mode), operating with Cu–K$\alpha_1$ radiation ($\lambda$ =1.54 Å ). Samples were grinded and measured on silicon or deepened plastic samples holders. Each sample was scanned in the range $2^o < 2\theta < 55^o$ with a $0.05^o$ step size at a scan rate of 4 s per step.

### Solid State NMR (ssNMR)

$^{13}C$ solid-state MAS NMR experiments were acquired on a BrukerAvance 300MHz (7 T) spectrometer using 4mm zirconia rotors as sample holders, spinning at MAS rate nMAS = 14 kHz. The chemical shift reference was tetramethylsilane (TMS; d =0 ppm). $^1H$ $t_1$ relaxation time was set to 3 s.

$^{15}N$ solid-state MAS NMR spectra were acquired on a Bruker Avance 300 MHz (7 T) spectrometer using respectively 7 mm zirconia rotors as sample holders, spinning at MAS rate nMAS = 5 kHz. $^{15}N$ chemical shift were referenced to labelled glycine at -348 ppm on the nitromethane scale (CH3NO2; $\delta$ = 0 ppm).
SsNMR experiments were all carried out at the facilities of the Laboratoire de Chimie de la Matiere Condensee de Paris, College de France.

**X-ray Photoelectron Spectroscopy (XPS)**

XPS was carried out using a Thermo-Scietific K-Alpha instrument with monochromatic X-ray source AlK$\alpha$ (1486.6 eV) and a monochromatic spot of 400 $\mu$m by Dr. Carmen Serra (University of Vigo, Vigo, Spain). Binding energies for the high-resolution spectra were calibrated by setting C 1s at 285.0 eV.

**Thermogravimetric Analysis – Infrared Spectroscopy (TG-IR)**

TG-IR measurements were performed on a 20 mg sample by using a Netzsch STA 409 C/3/F with a TASC 414/3 system controller set at 180-200 $^{o}$C at heating rate of 10 K $min^{-1}$ under N2 at 100 mL $min^{-1}$. IR spectra of volatiles were recorded on a Bruker EQUINOX-55 FT instrument equipped with a liquid $N_2$ cooled MCT detector with a resolution of 4 $cm^{-1}$ and 64 scans.

**Gas Chromatography – Mass Spectrometry (GC-MS)**

GC-MS experiments were performed on a Agilent 6890N GC connected to an Agilent 5975 mass spectrometer with EI ionization (70 eV). The Chromatogram was analysed using the ChemStation software from Agilent equipped with NIST 2.0 database

**High Resolution Tunneling Electron Microscopy (HRTEM)**

Microanalysis was carried out using a Hitachi HF3300 cold-field emission TEM/STEM at 300 kV. The STEM images were taken using the TEM, ZC, and SE modes. The carbon sample was dispersed onto a holey carbon film supported on a 200-mesh copper grid. The heating experiments were carried out using a heating system (Aduro$^{TM}$ In Situ System, Protochips, Inc. Raleigh, NC, USA) capable of reaching 1200$^{o}$C. The temperature on the chip was controlled by varying the current applied to the heating stage according to the calibration curve provided by the vendor.

**Gas Sorption Analysis**

$N_2$ and $CO_2$ sorption measurements, showed in chapter 4 and 6, were performed respectively at 77K and 273K using a QUADRASORB SI equipped with automated surface area and pore size analyzer. Prior to measurements samples were degassed at 150$^{o}$C for 20 h using a "Masterprep" degassing system. The relative pressure range, employed for BET surface area estimation, was chosen according to the conditions explained in Reference [137], which have been shown to yield reliable results also for highly microporous materials. The $V_{DR}$ pore volume values were calculated as explained in Reference [131].

Porous texture characterisation of the samples investigated in Chapter 5 was carried out in the University of Alicante in a collaboration framework with the group of Prof. Lozano-Castelló. The instrumental details are herein reported as provided by the collaboration partner. The measurements were performed by physical adsorption of gases ($N_2$ at 77 K and $CO_2$ at 273 K) using an automatic adsorption system (Autosorb-6, Quantachrome).

**High Pressure $CH_4$ Storage Measurements**

These measurements were carried out in the University of Alicante in a collaboration framework with the group of Prof. Lozano-Castelló. The instrumental and measurement details are herein reported as provided by the collaboration partner. CH4 adsorption isotherms at 298K and high pressures have been obtained in a Sartorius high-pressure microbalance. The balance is equipped with a pressure indicator and a thermocouple mounted in the sample housing as well as with a rotary pump. The maximum pressure used in this study was 3 MPa. The experimental results have been corrected for buoyancy effects related to the displacement of gas by the sample, sample holder, adsorbed phase and pan. The corrections due to the sample holder and pan were obtained with a blank experiment carried out with the sample holder empty. The buoyancy due to the sample, which results in an apparent loss of weight, was estimated as the product of the skeletal volume of the sample and gas density. The buoyancy effect related to the adsorbed phase was corrected to obtain the absolute adsorption isotherms. The high-pressure adsorption isotherms are reproducible to about 1% within the error of the balance.

## CHAPTER 3

*Experimental Procedure*

10 wt% biomass (i.e. D-glucose, cellulose, amylose, alcell lignin, rye straw) in water solutions (20 ml) were prepared and stirred overnight. The raw rye straw was grinded to a maximum particle size of 0.8 mm prior being mixed. The prepared solutions were then poured into quartz vials, subsequently placed into 50ml Teflon lined stainless steel autoclaves. The autoclaves were then heated into a programmable oven, which had been pre-heated at the desired reaction temperature (HTC temperatures and reaction times have been specified in chapter 3). The autoclaves were cooled down in a water bath to room temperature. The HTC carbon was recovered by filtration, repeatedly washed with distilled water until the attainment of a colourless aqueous phase and finally dried at 80 ºC under vacuum overnight.

$$HTC\ \ Yield\ \ (\%)\ \ = \frac{amount\ \ of\ \ solid\ \ after\ \ HTC\ \ (g)}{initial\ \ amount\ \ of\ \ biomass\ \ (g)}$$

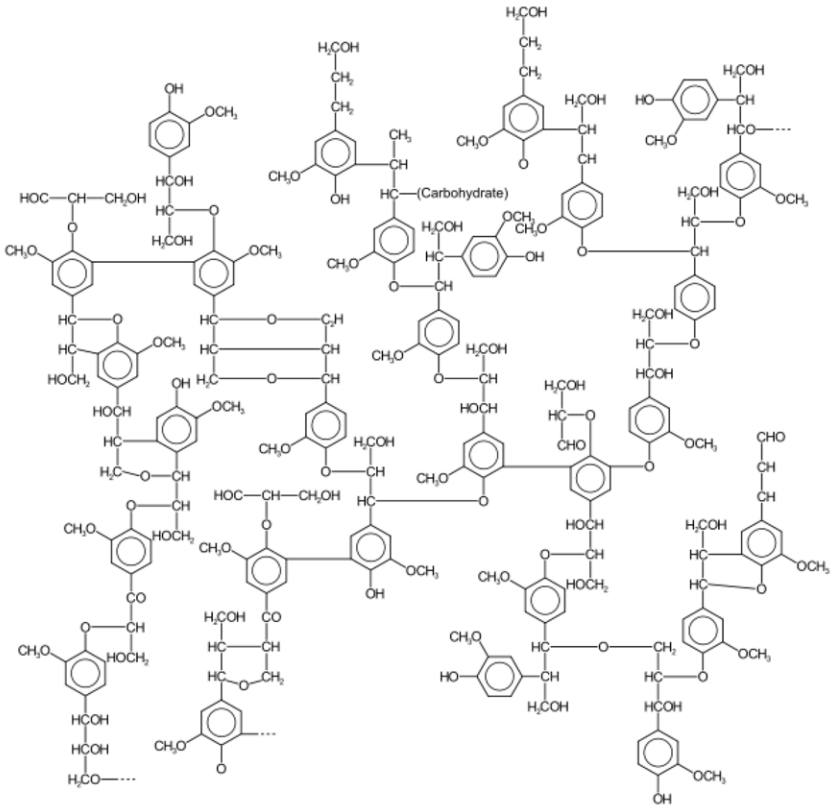


**Figure A.Ch3.1:** One of the available lignin models. Reproduced from A. W. Glazer, H. Nikaido, Microbial Biotechnology: fundamentals of applied microbiology, W. H. Freeman, **1999**

## CHAPTER 4

*Experimental Procedure*

Glucose derived HTC carbon samples were prepared as described in Chapter 3. The employed HTC temperature and reaction times were respectively 180$^{o}$C and 24 hours. The glucose derived HTC samples were then pyrolysed (Δ symbol denotes pyrolysed samples) at different temperatures ( 350, 550, 600, 750, 900 $^{o}$C) for 6 hours (if not differently stated) under $N_2$ flow in a muffle oven. The heating rate was 10 K min$^{-1}$. Raw D-glucose and starch (Glu-Δ350$^{o}$C, Sta- Δ350$^{o}$C) were also directly pyrolysed at 350 $^{o}$C for respectively 3 and 6 hours under $N_2$ flow.

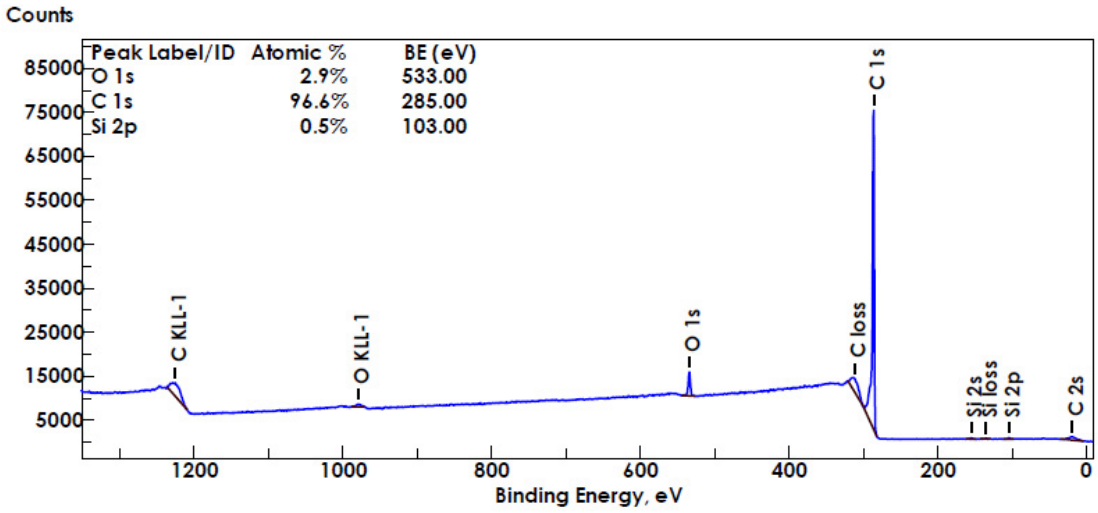


**Figure A.Ch4.1:** XPS survey scan of HTC carbon pyrolysed at 900$^{o}$C.

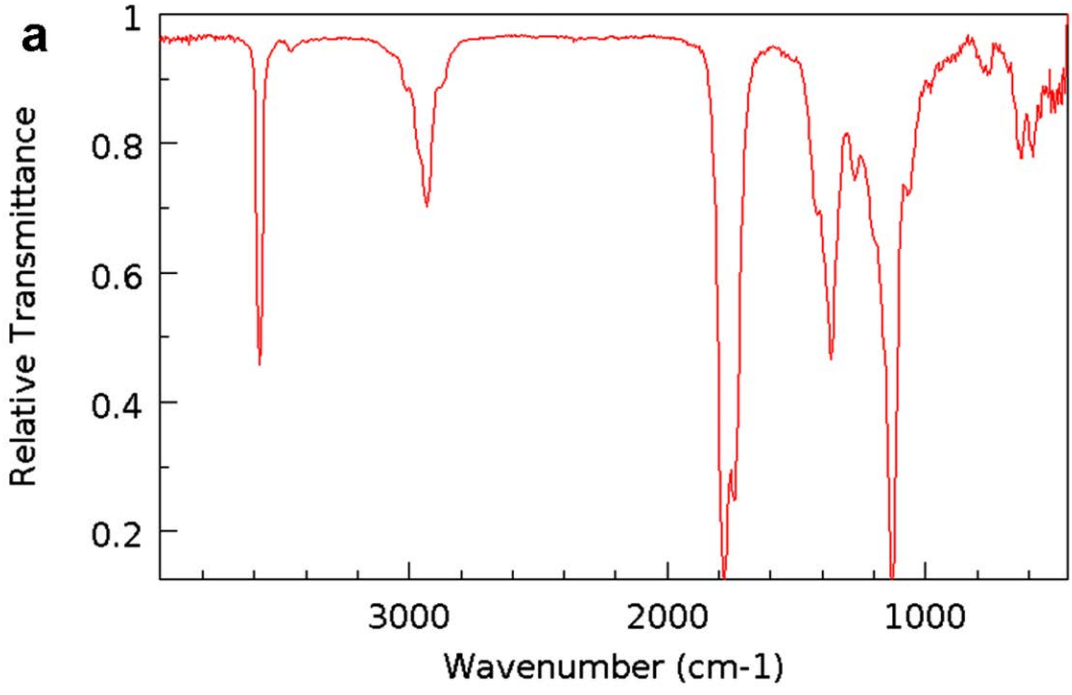

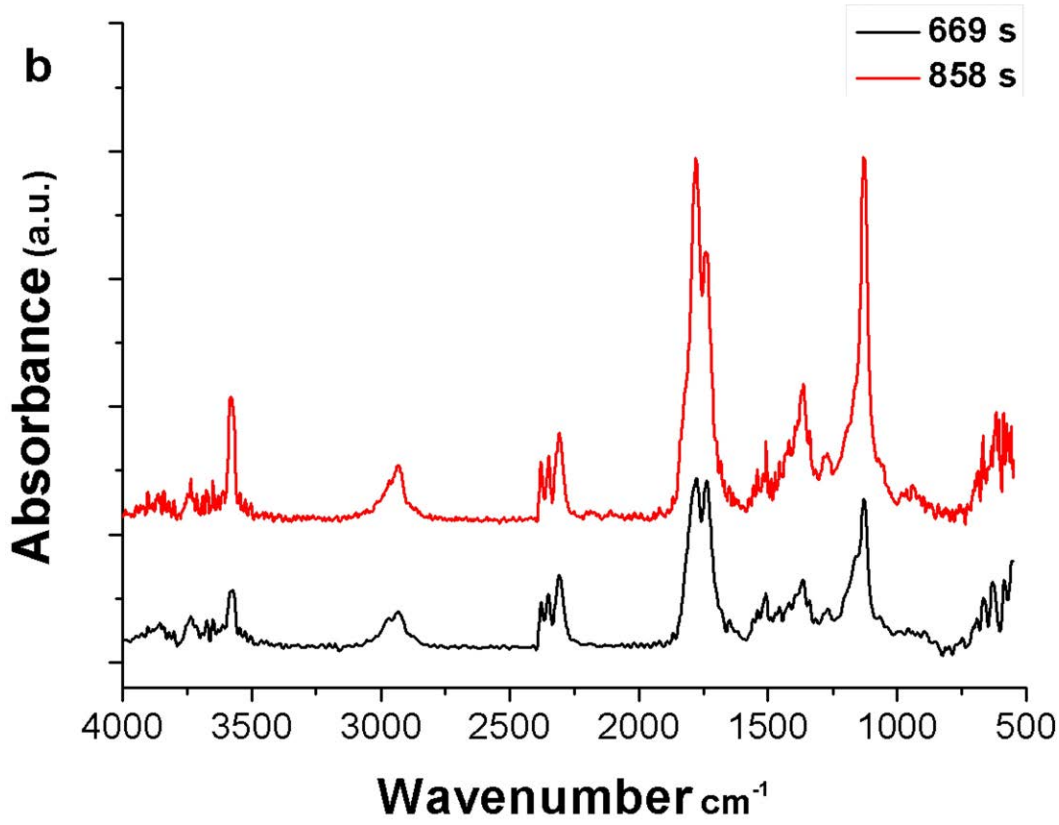


**Figure A.Ch4.2:** a) IR spectrum of gaseous levulinic acid. Reproduced from NIST Chemistry WebBook (**http://webbook.nist.gov/chemistry**), b) IR spectra of volatiles evolved during HTC carbon (non-extracted sample) pyrolysis recorded at two different times (after 669 and 858 seconds).

## CHAPTER 5

*Experimental Procedure*

HTC carbon samples were synthesised according to the experimental procedure described in chapter 3. The KOH chemical activation step was carried out in the University of Alicante in a collaboration framework with the group of Prof. Lozano-Castelló. The experimental procedure is herein reported as provided by the collaboration partner. Chemical activation with KOH was carried out using an impregnation method. Two grams of HTC were mixed, by stirring with a solution that contained 10 ml of water and 4, 6 or 8 g of the activating agent depending on the ratio of activating agent/HTC used (2/1, 3/1 or 4/1, respectively) for two hours at 60 ºC. The resulting slurry was dried at 110 ºC overnight in an oven. Then, the resulting mixture was used for carbonisation. The carbonisation was carried out in a horizontal furnace, and the samples were heated up to 750 ºC at 20ºC/min under a nitrogen flow rate of 500 ml/min. Samples were kept at the carbonization temperature for 2 hours

before cooling down under nitrogen. The pyrolysed samples were washed repeatedly with a 5M solution of HCl and later with distilled water until free of chloride ions.

**Table A.Ch5.1:** Elemental Composition of ACs produced via KOH chemical activation of biomass derived HTC carbons.

| | Elemental Composition (wt%) | | |
|---|---|---|---|
| **Sample** | **C%** | **H%** | **O%** |
| **G-180** | 87.10 | 1.80 | 11.10 |
| **G-240** | 88.99 | 1.69 | 9.32 |
| **G-280** | 85.47 | 2.03 | 12.50 |
| **C-200** | 87.05 | 1.73 | 11.22 |
| **C-240** | 88.33 | 1.94 | 9.73 |
| **C-280** | 84.86 | 1.93 | 13.21 |
| **RS-240** | 87.77 | 1.75 | 10.48 |
| **RS-280** | 84.50 | 1.98 | 13.52 |
| **RS-2** | 84.98 | 2.14 | 12.88 |
| **RS-3** | 87.77 | 1.75 | 10.48 |
| **RS-4** | 88.64 | 1.49 | 9.87 |

**Table A.Ch5.2:** Calculated surface area (S) and pore volume (V) using different models (subscript) on either $N_2$ or $CO_2$ isotherms for G-180°C, G-240°C, G-280°C

| Sample | $S_{N2\text{-}BET}$ ($m^2/g$) | $V_{N2\text{-}Ex}$ ($cm^3/g$) [(a)] | $V_{N2\text{-}DR}$ ($cm^3/g$) | $V_{CO2\text{-}NLDFT}$ ($cm^3/g$) | $V_{CO2\text{-}DR}$ ($cm^3/g$) |
|---|---|---|---|---|---|
| **G-180** | 1859 | 0.94 | 0.69 | 0.34 | 0.31 |
| **G-240** | 2264 | 1.21 | 0.84 | 0.40 | 0.35 |
| **G-280** | 1610 | 0.73 | 0.66 | 0.41 | 0.41 |

[(a)] Calculated from the experimental isotherm

**Table A.Ch5.3:** Calculated surface area (S) and pore volume (V) using different models (subscript) on either $N_2$ or $CO_2$ isotherms for C-200, C-240, C-280, RS-240 and RS 280

| Sample | $S_{N2\text{-}BET}$ ($m^2/g$) | $V_{N2\text{-}Ex}$ ($cm^3/g$) [(a)] | $V_{N2\text{-}DR}$ ($cm^3/g$) | $V_{CO2\text{-}NLDFT}$ ($cm^3/g$) | $V_{CO2\text{-}DR}$ ($cm^3/g$) |
|---|---|---|---|---|---|
| **C-200** | 1827 | 0.95 | 0.71 | 0.39 | 0.37 |
| **C-240** | 2334 | 1.26 | 0.84 | 0.40 | 0.38 |
| **C-280** | 1082 | 0.50 | 0.45 | 0.33 | 0.34 |
| **RS-240** | 2361 | 1.11 | 0.93 | 0.44 | 0.42 |
| **RS-280** | 1930 | 0.95 | 0.82 | 0.44 | 0.42 |

[(a)] Calculated from the experimental isotherm

**Table A.Ch5.4:** Calculated surface area (S) and pore volume (V) using different models (subscript) on either $N_2$ or $CO_2$ isotherms for RS-2:1, RS-3:1, RS-4:1

| Sample | $S_{N2\text{-}BET}$ ($m^2/g$) | $V_{N2\text{-}Ex}$ ($cm^3/g$) [(a)] | $V_{N2\text{-}DR}$ ($cm^3/g$) | $V_{CO2\text{-}NLDFT}$ ($cm^3/g$) | $V_{CO2\text{-}DR}$ ($cm^3/g$) |
|---|---|---|---|---|---|
| **RS-2:1** | 1665 | 0.77 | 0.68 | 0.40 | 0.39 |
| **RS-3:1** | 2361 | 1.11 | 0.93 | 0.44 | 0.45 |
| **RS-4:1** | 2481 | 1.21 | 1.01 | 0.50 | 0.49 |

[(a)] Calculated from the experimental isotherm

## CHAPTER 6

*Experimental Procedure*

N-doped carbonaceous materials were obtained by hydrothermal treatment of raw microalgae (Spirulina Platensis) or of a mixture microalgae/glucose as follows. First, raw microalgae or a mixture microalgae/glucose were dispersed in water (15 wt% microalgae, 0 – 15 wt% glucose) and stirred for 18 h. The dispersion was then sealed in a glass vial inside a Teflon lined autoclave and heat-treated at 180 – 240 ºC for 24 h in programmable oven, which had been pre-heated to the desired reaction temperature. The autoclave was cooled down in a water bath to room temperature. The solid products were separated by filtration, repeatedly washed with distilled water until the attainment of a colourless aqueous phase and finally dried at 80 ºC under vacuum overnight.

The microalgae or microalgae/glucose derived HTC products were then finely grinded in a mortar and physically mixed with the desired KOH amount. The reaction mixture was then heated into a tubular furnace under constant $N_2$ flow. The employed heating rate and dwelling time were respectively 3 K $min^{-1}$ and 1 hour. The activated samples were then thoroughly washed with 10wt% HCl solutions to remove any inorganic salts, and then with distilled water until the attainment of neutral pH washings. The samples were finally dried in a vacuum oven at 80$^{o}$C overnight.

The N and C efficiency were defined as follows:

$$N\ Efficiency = \frac{N\ amount\ present\ in\ the\ HTC\ product}{N\ amount\ present\ in\ the\ carbon\ precursor}$$

$$C\ Efficiency = \frac{C\ amount\ present\ in\ the\ HTC\ product}{C\ amount\ present\ in\ the\ carbon\ precursor}$$

**Table A.Ch6.1:** Major amino acids present in the microalgae. The composition has been provided by IGV Institut für Getreideverarbeitung GmbH

| Amino acid | Concentration (g/kg) |
|---|---|
| Isoleucine | 34-50 |
| Leucine | 54-87 |
| Lysine | 29-65 |
| Methionine | 13-25 |
| Phenylalanine | 27-42 |
| Threonine | 31-63 |
| Thryptophan | 9-24 |
| Valine | 38-55 |

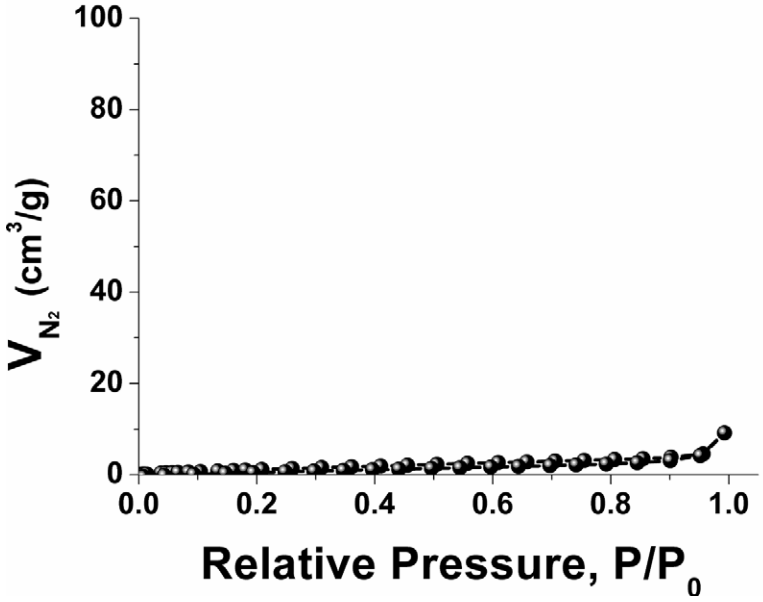


**Figure A.Ch6.1:** $N_2$ sorption isotherm measured for a representative sample of microalgae derived HTC product.